UNSTEADY AIRFOIL STALL AND STALL FLUTTER

Final Technical Report

Lockheed

MISSILES & SPACE COMPANY

A GROUP DIVISION OF LOCKHEED AIRCRAFT CORPORATION

SUNNYVALE, CALIFORNIA

UNSTEADY AIRFOIL STALL

AND STALL FLUTTER

Final Technical Report

Prepared by

Lars E. Ericsson
Senior Staff Engineer, Engineering Technology

J. Peter Reding
Research Specialist, Aero-Thermodynamics

June 1971

Prepared under Contract NAS 1-9987
for
NASA, Langley Research Center

LOCKHEED MISSILES & SPACE COMPANY
Sunnyvale, California

NASA CR-111906

UNSTEADY AIRFOIL STALL AND STALL FLUTTER

By Lars E. Ericsson and J. Peter Reding

June 1971

Issued by Originator as LMSC Report No. A-6J-71-1

Prepared under Contract NAS 1-9987 by
Lockheed Missiles & Space Company
Sunnyvale, California

for

NATIONAL AERONAUTICS AND SPACE ADMINISTRATION

ABSTRACT

A study has shown that the unsteady airfoil stall characteristics can be described analytically using static experimental data as an input. It is found that the dynamic overshoot of static stall does not in itself generate any time lag above the Karman-Sears wake lag. It is the post stall aerodynamic forces that create an additional time lag, which is dominant at high frequencies. The analytic theory is found to predict dynamic loops and measured negative damping as long as the frequency is not very large. In the latter case, a graphical method for modulation of the separation induced phase lag gives improved agreement with experimental data. The effects of compressibility and shock-induced boundary layer separation are included in the analysis, and it is shown that the experimentally determined stall flutter boundaries of a space shuttle wing can be predicted using only static data as an input.

SUMMARY

An analytic theory has been developed that satisfactorily describes the characteristics of unsteady airfoil stall at low and moderately high frequencies. The high frequency characteristics can be predicted by a semi-empirical graphical technique. In both cases, static (experimental) data are used as an input. The dynamic overshoot of static stall is caused by pitch rate induced improvements of the boundary layer characteristics which in themselves do not generate any additional time lag. It is the post stall characteristics that are associated with additional time lag caused by the separation point movement. The regular Karman-Sears vortex-wake lag exists throughout the dynamic cycle, even at moderately high subsonic Mach numbers. The effects of compressibility are included in the analysis, and it is outlined to what extent three-dimensional flow effects may influence the "two-dimensional" results. The stall flutter boundaries of a space shuttle wing are predicted both for wind tunnel Reynolds number and full scale flight. The boundaries measured in a subscale wind tunnel test are in good agreement with the analytic predictions.

CONTENTS

ILLUSTRATIONS

ILLUSTRATIONS (Continued)

ILLUSTRATIONS (Continued)

ILLUSTRATIONS (Continued)

Section 1
INTRODUCTION

Stall flutter is a problem that has received a great deal of attention by helicopter and compressor industry during the past 10 years (Refs. 1-4). Recently the problem has become of great concern also to the aerospace industry, as some of the winged space shuttle vehicles will experience stall flutter in their transition from very high hypersonic entry angles to the sub-stall angles of attack of the subsonic cruise portion of the reentry (Ref. 5). Because of this, a preliminary research study was performed to investigate the unsteady aerodynamics associated with airfoil stall (Ref. 6). A semi-empirical method was developed that could predict the measured dynamic stall characteristics as long as the oscillatory frequencies were low (Refs. 6 and 7).

The success of this preliminary study indicated that the prediction of airfoil dynamics and stall flutter from static experimental characteristics was possible. It was also found that unsteady airfoil stall is very difficult to simulate in wind tunnel tests (Ref. 8). It was, therefore, decided to extend the initial study to include (1) compressibility effects, and (2) three-dimensional flow effects, and to develop analytic means for (3) prediction of dynamic stall characteristics and (4) analysis of stall flutter. This report documents the results of this extended analysis.

Section 2
ANALYSIS OF UNSTEADY AIRFOIL STALL

The three factors determining when and where flow separation occurs are (listed in probable order of importance for airfoil stall):

1. Boundary layer profile shape
2. Boundary layer thickness
3. Adversity of local pressure gradient

As the two-dimensional flow over an airfoil is not subject to any cross flow with associated effects on the boundary layer thickness and profile shape, all three factors are in fact determined by the pressure distribution. The first two parameters carry the effects of the pressure gradient on the boundary layer development up to the separation point. In addition to this pressure gradient time history effect, the boundary layer profile shape and thickness are also dependent upon initial ambient flow parameters such as Mach number, Reynolds number and turbulence level, as well as on surface roughness and eventual boundary layer suction or blowing effects. Boundary layer profile shape and thickness are both affected by the same flow parameters but in different ways. A turbulence trip will, for example, usually improve the form factor but increase the boundary layer thickness. That is, the two first parameters cannot be combined into one single parameter. The third factor, the adversity of the local pressure gradient (at the separation point) affects the flow separation in a very direct (local) manner, that is easier to visualize than the integrated pressure time history effects associated with the two first flow parameters.

In the analysis that follows, the effects of the airfoil motion on these flow parameters, and thereby on the airfoil stall, will be investigated. Incompressible flow is analyzed first, and the effects of compressibility and three-dimensional flow will be discussed later as the analysis proceeds.

2-1 INCOMPRESSIBLE FLOW

On the pitching airfoil the pressure gradient lags the airfoil motion because of circulation lag and accelerated flow effects (Ref. 6). The circulation lag, as defined by the Karman-Sears vortex wake effects (Ref. 9), can be approximated by a constant time lag at low frequencies and by a constant phase lag at high frequencies (Ref. 7).

In addition to this circulation lag, there is a delay of the adversity of the pressure gradient on the leeward side caused by the accelerating flow generated by the airfoil motion during pitch-up. The non-stationary Bernoulli equation gives the following relationship for constant ambient (free stream) conditions (Ref. 6):

$$\frac{dp_e}{d\xi} = \left(\frac{\partial p_e}{\partial \xi}\right)_{\dot{\alpha}=0} + \frac{\partial p_e}{\partial \alpha}\,\frac{c\dot{\alpha}}{U_e} \qquad (1)$$

The local pressure gradient is in the dynamic case less than in the static case by an amount $-\frac{\partial p_e}{\partial \alpha}\,\frac{c\dot{\alpha}}{U_e}$. The corresponding delay in the dynamic case to reach the static local value is (Ref. 10),

$$\Delta\alpha = \alpha(t) - \alpha(t - \Delta t) = -\frac{\frac{\partial p_e}{\partial \alpha}}{\frac{\partial}{\partial \alpha}\left(\frac{\partial p_e}{\partial \xi}\right)_{\dot{\alpha}=0}}\,\frac{U_\infty}{U_e}\,\frac{c\dot{\alpha}}{U_\infty} \qquad (2)$$

The accelerated-flow-induced pressure-gradient-delay is expressed in form of an equivalent time lag in Eq. (2). $\Delta\alpha$ is the dynamic overshoot of the static angle of attack needed to reach the same adversity of the pressure gradient at separation.

In addition to this local pressure gradient effect at separation, $\xi = \xi_s$, the time history effect of the pressure gradient relief upstream of separation, $\xi < \xi_s$, improves the boundary layer, decreasing both the form factor H and the thickness δ up to

separation (Ref. 11). As a result, the boundary layer can stand a higher adverse pressure gradient before separation; that is, there is in the dynamic case an overshoot of the static value for the critical pressure gradient.

$$\left(\frac{dp_e}{d\xi}\right)_{crit} = \left[\left(\frac{\partial p_e}{\partial \xi}\right)_{crit}\right]_{\dot{\alpha}=0} + \frac{\partial}{\partial\left(\frac{c\dot{\alpha}}{U_\infty}\right)}\left(\frac{\partial p_e}{\partial \xi}\right)_{crit}\frac{c\dot{\alpha}}{U_\infty} \tag{3}$$

As a result of this boundary layer improvement, the static stall angle α_s is overshot by an amount $\Delta\alpha_s$ (giving an overshoot $\Delta c_{l_{max}} = c_{l_\alpha}\Delta\alpha_s$ of static $c_{l_{max}}$).

$$\Delta\alpha_s = \frac{\frac{\partial}{\partial\left(\frac{c\dot{\alpha}}{U_\infty}\right)}\left(\frac{\partial p_e}{\partial \xi}\right)_{crit}\frac{c\dot{\alpha}}{U_\infty}}{\frac{\partial}{\partial \alpha}\left[\left(\frac{\partial p_e}{\partial \xi}\right)_{crit}\right]_{\dot{\alpha}=0}} \tag{4}$$

This improvement of the boundary layer and resulting increase of the critical pressure gradient is associated with a time lag effect. It is the upstream pressure gradients at earlier time instants that determine the boundary layer parameters at separation. The effects are somewhat similar to the boundary layer thickening due to forebody cross flow on a cone-cylinder body (Ref. 10). That is, the upstream pressure gradient effects are convected downstream. If we, as in the case of the boundary layer cross flow (Ref. 10), lump the upstream effects to one station, $\xi = \bar{\xi}$, we can express the boundary layer shape factor H and thickness δ at ξ_s in the following form for the pitching airfoil ($\alpha = \alpha_o + \theta$)

$$H(\xi_s, t) = H(\xi_s, \alpha_o) + \frac{\partial H(\xi_s)}{\partial p_{e_\xi}(\bar{\xi})}\frac{\partial p_{e_\xi}(\bar{\xi})}{\partial \alpha}\theta(\bar{\xi}, t - \Delta t_c - \Delta t_w) \tag{5}$$

$$\delta(\xi_s, t) = \delta(\xi_s, \alpha_o) + \frac{\partial \delta(\xi_s)}{\partial p_{e_\xi}(\bar{\xi})}\frac{\partial p_{e_\xi}(\bar{\xi})}{\partial \alpha}\theta(\bar{\xi}, t - \Delta t_c - \Delta t_w) \tag{6}$$

$$\theta(\bar{\xi}) = \theta + \left(\bar{\xi} - \xi_{CG}\right)\frac{c\dot{\theta}}{U_\infty} \tag{7}$$

The time lag Δt_c is the time required to convect the integrated pressure gradient effects around the leading edge surface (coordinate s) with some mean convection velocity $\bar{U}$ and t_w is the Karman-Sears vortex wake lag, $t_w = 1.5\ c/U$ (Ref. 6)

$$\Delta t_c = \frac{s_s - \bar{s}}{\bar{U}} = K_s \frac{\left(\xi_s - \bar{\xi}\right)c}{\bar{U}} \tag{8}$$

For harmonic oscillations

$$\theta(t - \Delta t) = |\theta| e^{i\omega(t - \Delta t)} = \theta e^{-i\omega\Delta t} \tag{9}$$

With Δt_c given by Eq. (8), $\omega\Delta t_c$ is

$$\omega\Delta t_c = K_s\left(\xi_s - \bar{\xi}\right)\frac{\omega c}{U_\infty}\frac{U_e}{\bar{U}}\frac{U_\infty}{U_e(\bar{\xi})} = K_{\bar{\xi}}\left(\xi_s - \bar{\xi}\right)\bar{\omega} \tag{10}$$

$$K_s < \frac{\pi}{2}, 1 > \frac{\bar{U}}{U_e} > 0.8\ ;\ \frac{1}{2} < \frac{U_e(\bar{\xi})}{U_\infty} < 2$$

That is $1 < K_{\bar{\xi}} < 4$. As $\left(\xi_s - \bar{\xi}\right) < .02$, $\omega\Delta t \ll 1$ and $\theta(t - \Delta t)$ can be expressed in the following form

$$\theta(t - \Delta t_c) = \theta(t) - \dot{\theta}(t)\Delta t_c \tag{11}$$

$$= \theta(t) - K_{\bar{\xi}}\left(\xi_s - \bar{\xi}\right)\frac{c\dot{\theta}}{U_\infty}$$

And $\theta(\bar{\xi}, t - \Delta t_c)$ becomes

$$\theta(\bar{\xi}, t - \Delta t_c = \theta(\bar{\xi}, t) - K_{\xi} \left(\xi_s - \bar{\xi}\right) \frac{c\dot{\theta}}{U_\infty} \tag{12}$$

For leading edge separation, $\bar{\xi} \approx 0$, $\xi_s < .02$, and we find that even with $K_{\bar{\xi}} = 4$, the convective time lag for the integrated pressure gradient effect is negligible. For separation farther aft, e.g., trailing edge stall, it is no longer of negligible magnitude.

A principal goal of the present investigation was to develop analytic means for predictions of the accelerated flow effects. In order to accomplish this, one needs to be able to compute the pressure gradients up to the point of flow separation. G. Ville has demonstrated that most NAGA-series airfoils have a near-leading-edge geometry that can be described by similar profiles (Ref. 12). Only one similarity parameter is needed, viz., the nose radius. The airfoil shape forward of the maximum thickness can be approximated by an ellipse (Fig. 1). Near the leading edge the ellipse is well approximated by the following parabola

$$\left(\frac{y}{r_N}\right)^2 = 2 \frac{x}{r_N} \tag{13}$$

The velocity determined by potential flow theory (Ref. 12) is as follows for moderate angles of attack ($\cos \alpha = 1$, $\sin \alpha = \alpha$).

$$v = \frac{U_e}{U_\infty} = \frac{\xi^{1/2} + \left[1 + \left(\frac{\rho_N}{2}\right)^{1/2}\right]\alpha}{\left(\xi + \frac{\rho_N}{2}\right)^{1/2}} \tag{14}$$

$$v_\xi = \frac{\partial v}{\partial \xi} = \frac{\frac{\rho_N}{2} \xi^{-1/2} - \left[1 + \left(\frac{\rho_N}{2}\right)^{1/2}\right]\alpha}{2\left(\xi + \frac{\rho_N}{2}\right)^{3/2}} \tag{15}$$

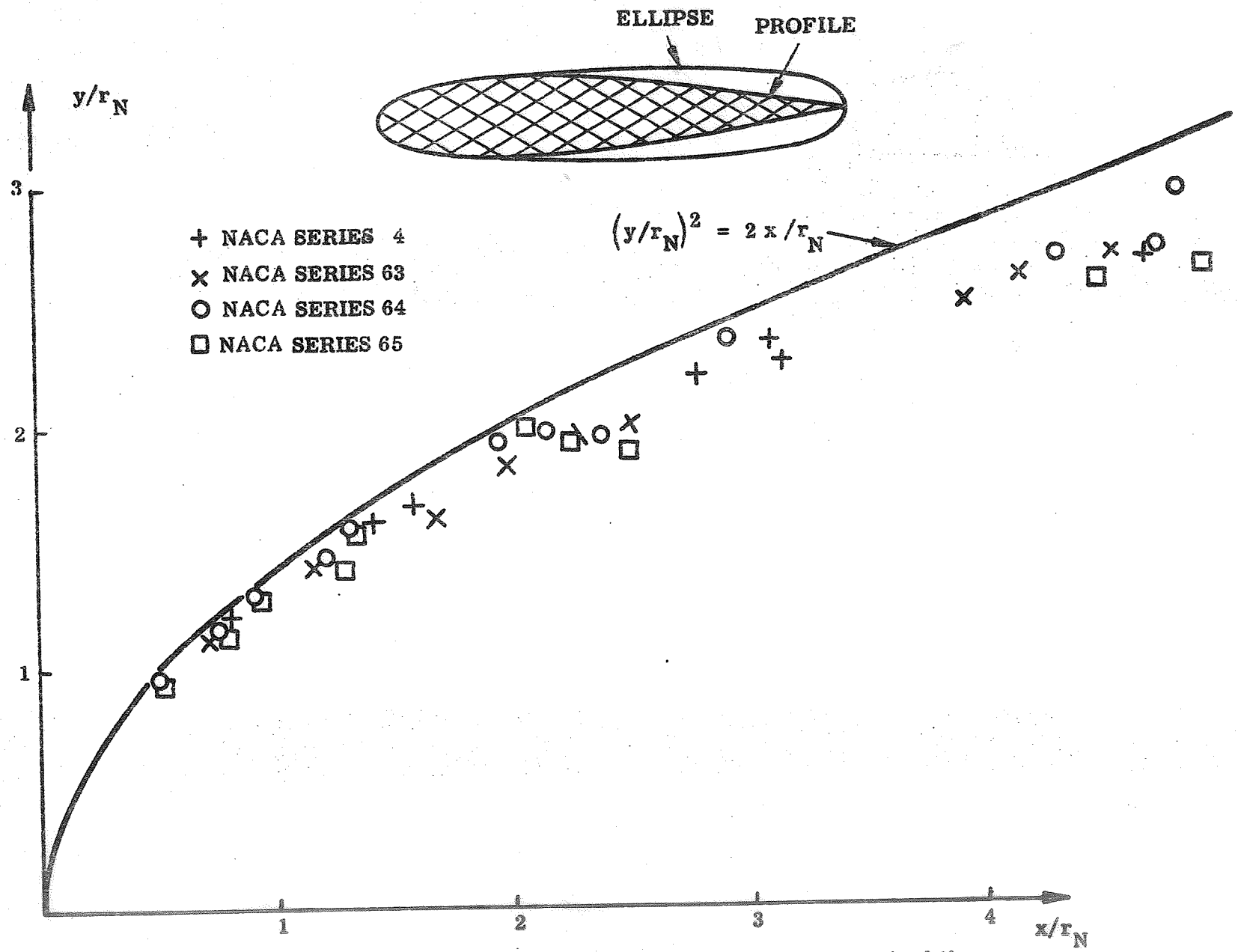

Figure 1 Leading Edge Similar Profiles for NACA-Series Airfoils

$$v_\alpha = \frac{\partial v}{\partial \alpha} = \frac{1 + \left(\frac{\rho_N}{2}\right)^{1/2}}{\left(\xi + \frac{\rho_N}{2}\right)^{1/2}} \tag{16}$$

$$v_{\alpha_{max}} = v_\alpha(\xi = 0) = 1 + \left(\frac{2}{\rho_N}\right)^{1/2} \tag{17}$$

This peak velocity due to unit angle of attack, $v_{\alpha_{max}}$, agrees exceedingly well with exact computations for NACA-series airfoils (Refs. 12 and 13, and Fig. 2). The downstream distribution (near the leading edge) of this α-induced velocity agrees also well with the exact computations (Fig. 3).

The pressure coefficient C_p is in incompressible flow

$$C_p = 1 - v^2 \tag{18}$$

Combining Eqs. (2), (14) and (18), noticing that p_e-derivatives can be substituted by C_{p_e}-derivatives, and that $U_e/U_\infty = v$, one obtains the following expression for the accelerated flow induced pressure gradient delay

$$\xi_a = -\frac{\frac{\partial p_e}{\partial \alpha}}{\frac{\partial}{\partial \alpha}\left(\frac{\partial p_e}{\partial \xi}\right)_{\dot{\alpha}=0}} \frac{U_\infty}{U_e}$$

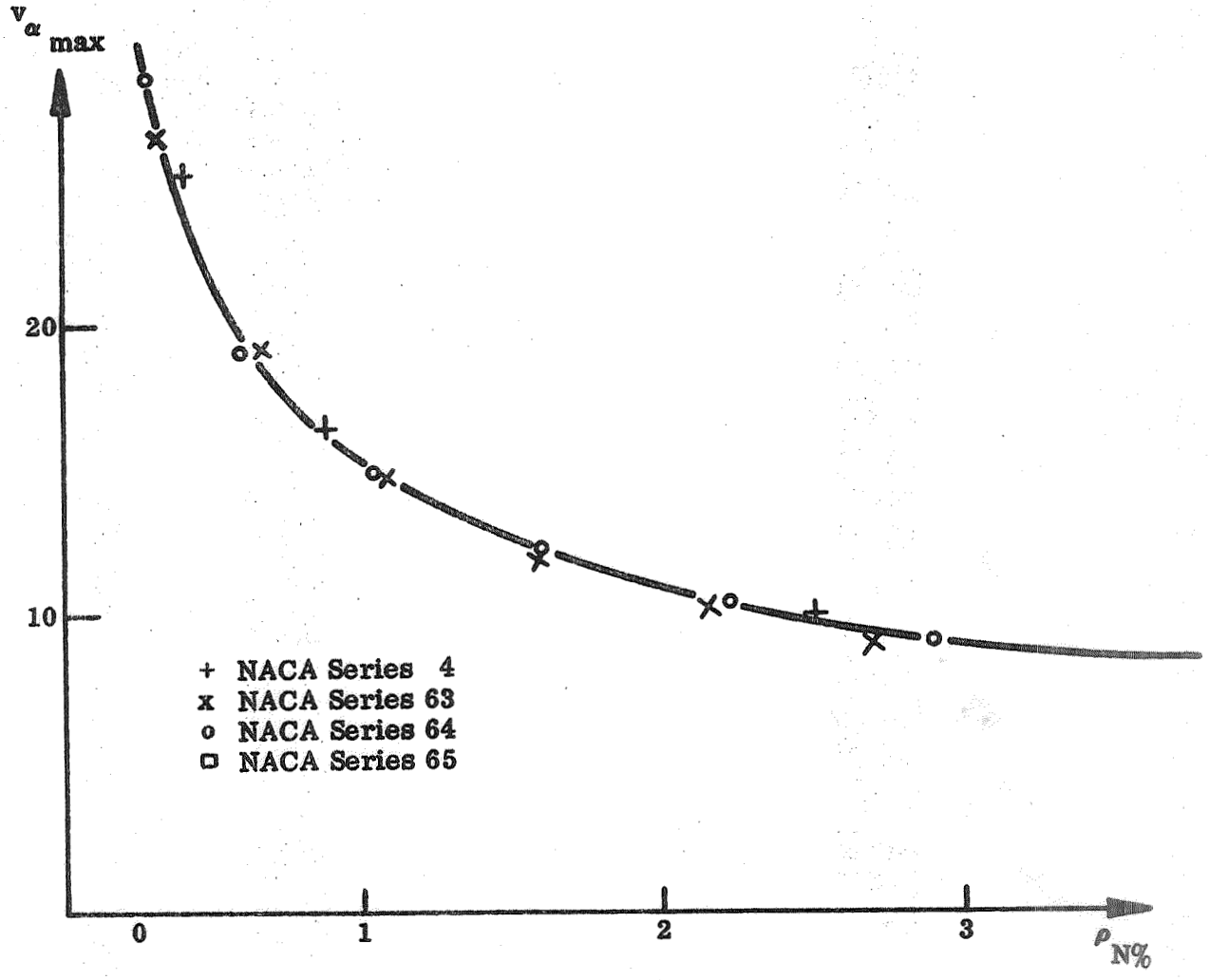

Figure 2 Effect of Nose Radius on Peak Velocity α-Derivative at $\alpha=0$

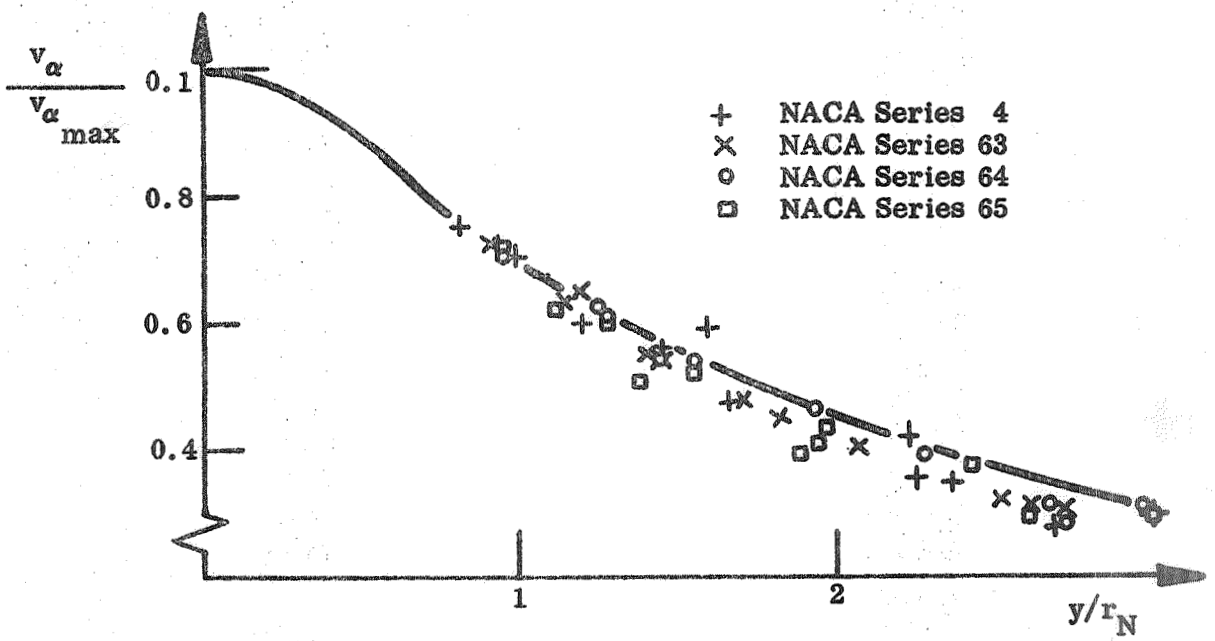

Figure 3 Incompressible Velocity Distributions at Leading Edge of NACA-Series Airfoils

$$\xi_a = \frac{2\left(\xi_s + \frac{\rho_N}{2}\right)^{3/2}}{2\alpha\left[1 + \left(\frac{\rho_N}{2}\right)^{1/2}\right] + (\xi_s)^{1/2}\left(1 - \frac{\rho_N}{2\xi_s}\right)} \tag{19}$$

This analytic formulation predicts what the accelerated flow induced pressure gradient delay and associated time lag effect would be for different airfoils (different ρ_N). We find that the magnitude of this delay is small. For a typical airfoil with $\xi_s \approx \rho_N$, Eq. (19) gives

$$\xi_a = \left(3/2\ \rho_N\right)^{3/2} \Bigg/ \left\{\left[1 + \left(\frac{\rho_N}{2}\right)^{1/2}\right]\alpha + \left(\rho_N\right)^{1/2}/4\right\}$$

Even at $\alpha = 0$, ξ_a is less than 0.1 for $\rho_N = 0.01$. At $\alpha = \alpha_s = 0.2$ it is eight (8) times less, and completely negligible (compared to the Karman-Sears wake lag, $\xi_w = 1.5$).

Thus, the time lag as such is negligible. However, the fact that the boundary layer upstream of separation has experienced the less adverse pressure gradients associated with earlier attitudes during the airfoil pitch-up motion adds to the pressure gradient relief of Eq. (1) in producing a boundary layer in the dynamic case that corresponds to that for a static airfoil with much more favorable leading edge curvature distribution than the actual airfoil.

The pressure gradient (at $\bar{\xi}$) upstream of separation is lagging the static value at the same angle of attack by the following amount ($\Delta t = c\Delta\xi/\bar{U}$)*

*The effect of pitch rate induced cross flow is treated separately later, Eqs. (22) - (24).

$$\frac{\partial}{\partial \alpha}\left(\frac{\partial p_e}{\partial \xi}\right)\Delta\alpha(\xi) = \frac{\partial}{\partial \alpha}\left(\frac{\partial p_e}{\partial \xi}\right)\left(\xi_a \frac{c\dot{\alpha}}{U_\infty} + \Delta\xi \frac{c\dot{\alpha}}{\bar{U}}\right)$$

That is, through Eqs. (14)-(18)

$$\Delta\alpha(\xi) = \left\{ \xi_a + \frac{\Delta\xi\left(\xi + \frac{\rho_N}{2}\right)}{\xi^{1/2} + 1 + \left(\frac{\rho_N}{2}\right)^{1/2}} \right\} \frac{c\dot{\alpha}}{U_\infty} \tag{20}$$

With $\frac{\partial p_e}{\partial \xi}$ known, including the effect of pitch rate and time lag, an analysis using the method due to von Karman and Pohlhausen (Ref. 11) could give an analytic expression for the dynamic overshoot $\Delta\alpha_s$, Eq. (4). This is, however, beyond the scope of the present report, which is only intended to provide the tools needed for "analytic extrapolation" from available experimental data. The effect of airfoil shape on the dynamic overshoot $\Delta\alpha_s$ can be expressed as follows:

$$\Delta\alpha_{s_1} = K_{a_1} \left\{ \frac{2\left(\bar{\xi} + \frac{\rho_N}{2}\right)^{3/2}}{2\alpha\left[1 + \left(\rho_N/2\right)^{1/2}\right] + (\bar{\xi})^{1/2}\left(1 - \frac{\rho_N}{2\bar{\xi}}\right)} + \frac{\bar{\xi}\left(\bar{\xi} + \frac{\rho_N}{2}\right)\frac{U_e}{\bar{U}}}{\alpha\left[1 + \left(\frac{\rho_N}{2}\right)^{1/2}\right] + \bar{\xi}^{1/2}} \right\} \frac{c\dot{\alpha}}{U_\infty} \tag{21}$$

$\bar{\xi}$ is the centroid of the integrated upstream pressure gradient effect, $0 < \bar{\xi} < \xi_s$, as used earlier for the convective time lag estimate, Eqs. (5)-(12).

While this pressure gradient effect probably is the most obvious contributor to the dynamic overshoot of static stall, there are other possibilities. It is well known that boundary layer transition plays an important role, especially in the case of leading edge stall (Refs. 14-18). It has recently been shown that boundary layer transition can be influenced by "quasi-steady harmonics" (Ref. 19), and one could, therefore, speculate that the airfoil oscillation could affect the stall via the transition process. The "moving wall" effect can also delay separation (Refs. 20-22). It has been shown that subtle modifications of the leading edge, viz., nose droop with and without changes of the nose radius, can produce as much as 50 percent increased $c_{l_{max}}$ (Refs. 23 and 24, and Fig. 4).

The dynamic nose droop effect is simply the forward portion of the pitch rate induced camber effect (Ref. 6 and Fig. 5).

$$\nu_{LE} = -\xi_{CG}\frac{c\dot{\theta}}{U_\infty} \tag{22}$$

The pitch rate induces an apparent curvature change due to the variation of pitch rate induced velocities normal to the surface around the leading edge (Fig. 6). (The effect is similar to the apparent base curvature effect discussed in Ref. 25.)

$$\frac{\Delta r_N}{r_N} = \frac{c\dot{\theta}}{U_\infty}\left[\frac{\left(1+\eta'^2\right)^{3/2}}{\eta''} + \frac{\eta - \left(\xi - \xi_{CG}\right)\eta'}{\left(1+\eta'^2\right)^{1/2}}\right] \tag{23}$$

Using the near-leading-edge approximation, Eq. (13), gives

$$\frac{\Delta r_N}{r_N} = \frac{c\dot{\theta}}{U_\infty}\left[\frac{\xi + \xi_{CG}}{\left(1+\frac{\xi}{\rho_{N/2}}\right)^{1/2}} - \rho_N\left(1+\frac{\xi}{\rho_{N/2}}\right)^{3/2}\right] \tag{24}$$

AIRFOIL	$c_{l_{max}}$ at $R_c = 4 \times 10^6$
NACA 64A010	1.07
1	1.36
2	1.44
3	1.65

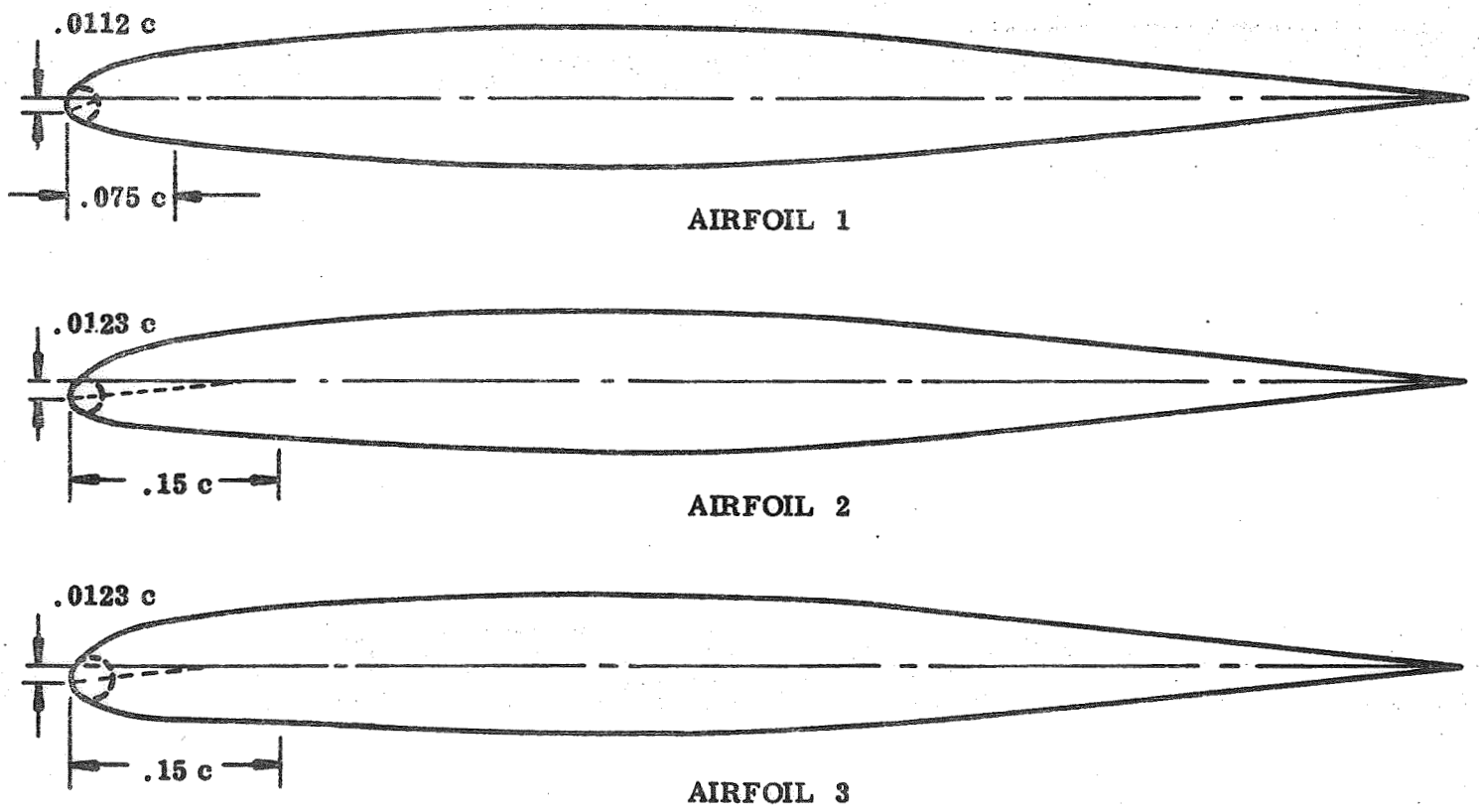

Figure 4 Effect of Leading Edge Modification on $c_{l_{max}}$

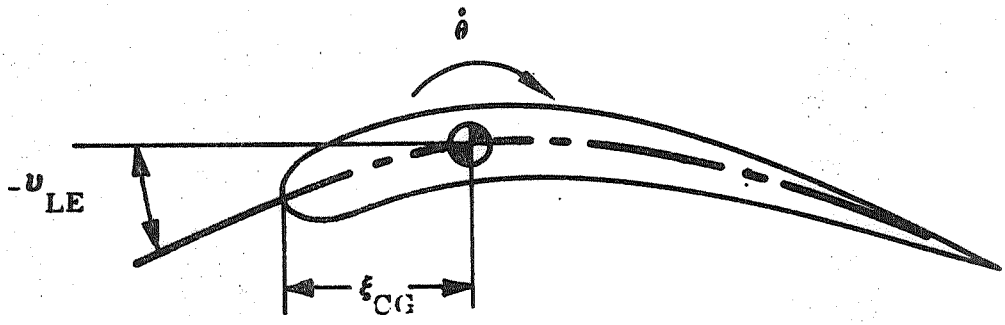

NOSE DROOP $\quad -v_{LE} = \xi_{CG} \ \frac{c\dot{\theta}}{U_\infty}$

Figure 5 Pitch Rate Induced Nose Droop

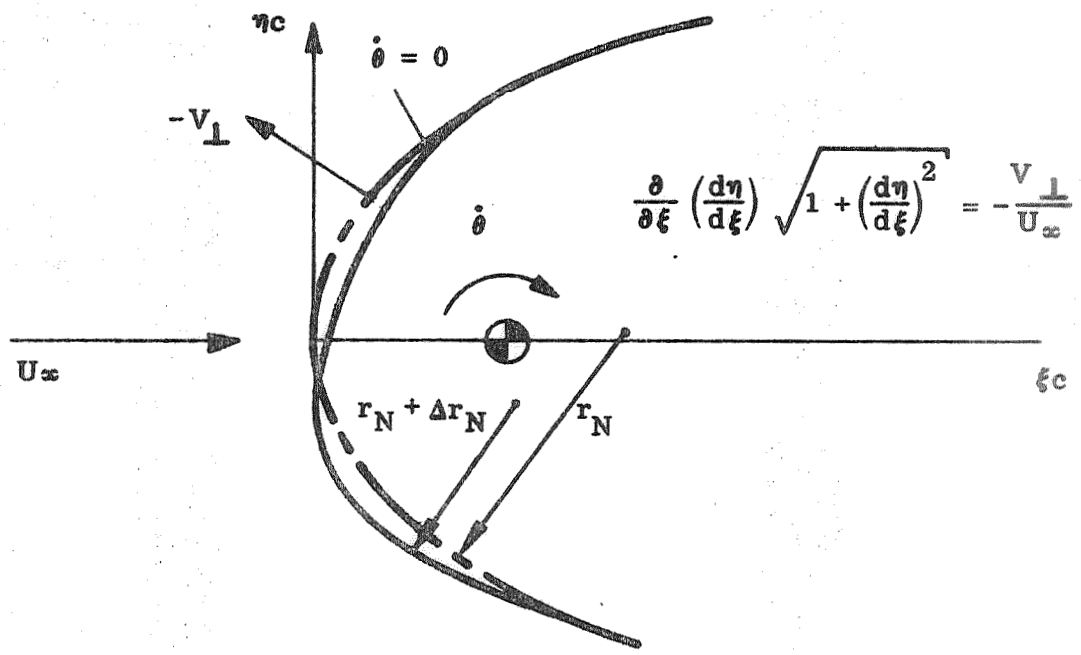

Figure 6 Pitch Rate Induced Change of Apparent Nose Curvature

$$\frac{\Delta r_N}{r_N} \approx \frac{\xi + \xi_{CG}}{\left(1 + \frac{\xi}{\rho_{N/2}}\right)^{1/2}} \frac{c\dot{\theta}}{U_\infty} \tag{25}$$

Again using the value $\xi_s = \rho_N$ for the location of the separation, we find that the magnitudes of the motion induced shape changes, as represented by the quasi-steady formulations in Eqs. (22) and (24), are very small. Certainly, the nose droop effect, Eq. (22), could not by itself account for more than a few percent increase in $c_{l_{max}}$.

The moving wall effect (Refs. 20-22 and Fig. 7), gives the following tangential velocity ratio for the airfoil.

$$\frac{U_w}{U_\infty} = \frac{\eta + \left(\xi_{CG} - \xi\right)\eta'}{\left(1 + \eta'^2\right)^{1/2}} \frac{c\dot{\theta}}{U_\infty} \tag{26}$$

Using Eq. (13) gives

$$\frac{U_w}{U_\infty} = \frac{\xi + \xi_{CG}}{\left(1 + \frac{\xi}{\rho_{N/2}}\right)^{1/2}} \frac{c\dot{\theta}}{U_\infty} \tag{27}$$

Again using the value $\xi_s \approx \rho_N$ for the location of separation, we find that the above effect is negligibly small.

Even if quasi-steady shape changes cannot by themselves produce any large effects, one may speculate that they could in some manner be amplified by oscillation induced increase of turbulence or effective Reynolds number. Increase in wind tunnel turbulence has been found to cause dramatic increase of static $c_{l_{max}}$ (Ref. 26 and Fig. 8).

In view of recent results for the quasi-steady influence on boundary layer transition (Ref. 19), one can find some reason to believe that the pitch oscillation can increase the effective Reynolds number, as was speculated earlier in regard to the peculiar dynamic data for the "sharp wing" obtained by Halfman et al. (Refs. 6 and 27).

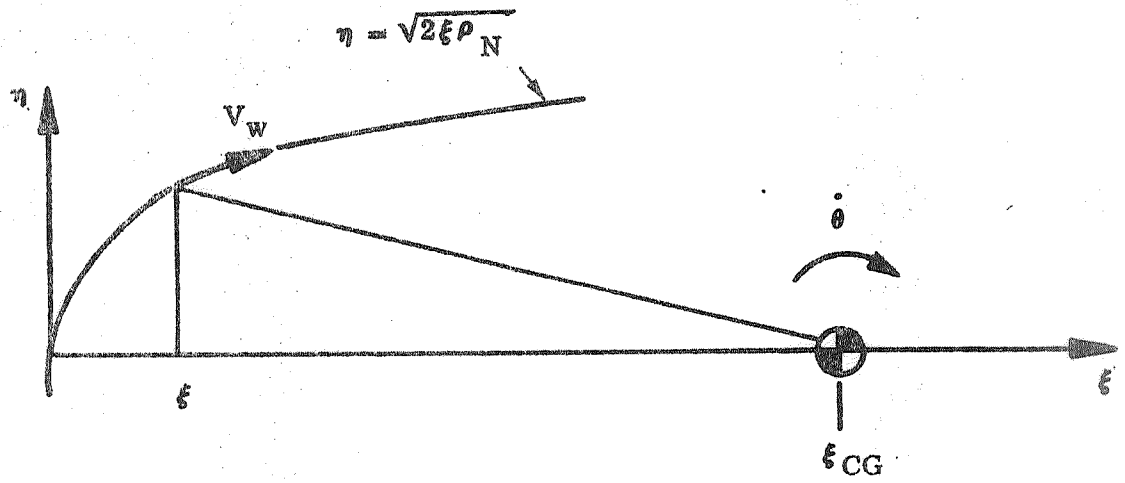

Figure 7 Leading Edge Moving Wall Effect

AR = 6. NACA AIRFOIL.

ROOT: 66(215)-116 (a = 0.6)

TIP: 66(215)-216 (a= 0.6)

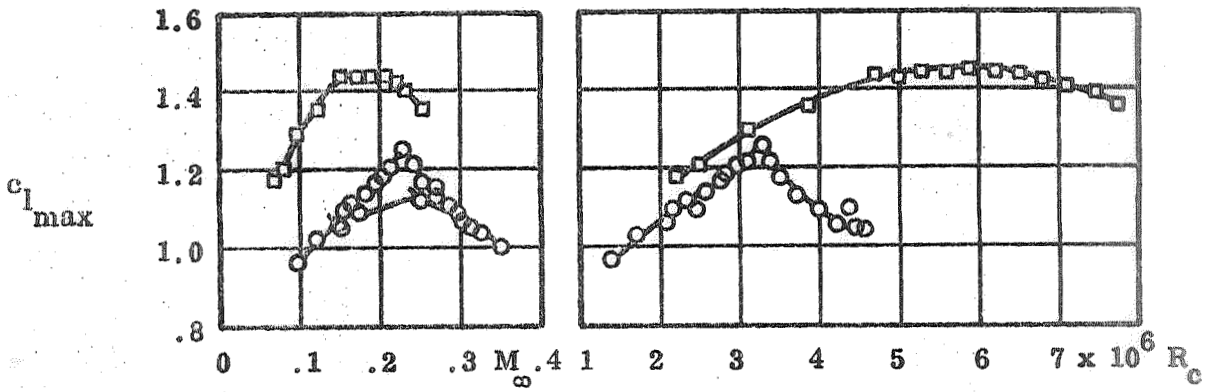

—o— LANGLEY 19-FOOT PRESSURE TUNNEL, ATMOSPHERIC PRESSURE

—□— LANGLEY 19-FOOT PRESSURE TUNNEL, PRESSURE, 33 LB/SQ IN.

—◇— LANGLEY 16-FOOT HIGH-SPEED TUNNEL

a. Wind Tunnel Turbulance

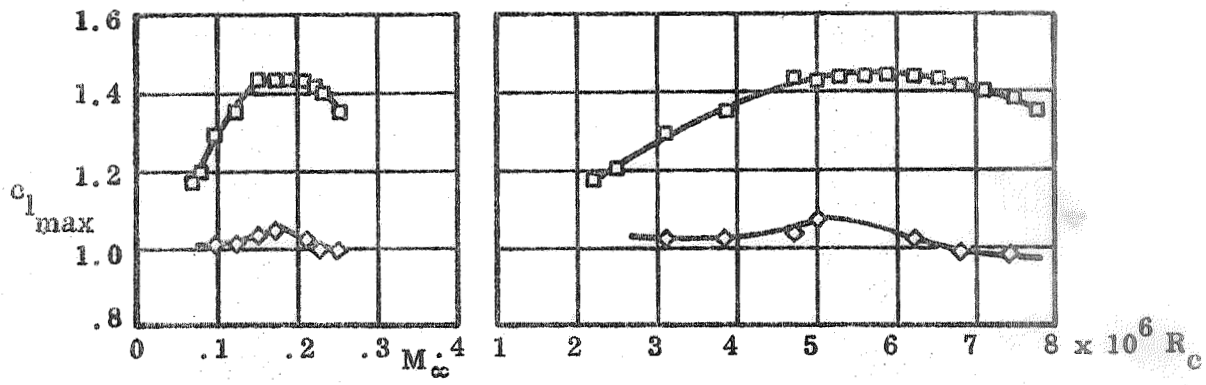

—□— SMOOTH L. E.

—◇— ROUGH L. E.

b. Surface Roughness

Figure 8 Effect of Turbulence and Surface Roughness on the $c_{l_{max}}$ of a NACA 66-Series Airfoil

However, one has great difficulty to see how any such mechanism can be present in the airplane pull-up maneuvers (Refs. 28 - 32) to cause the observed large dynamic overshoot of static stall, without it also being present in the quasi-steady simulations.

One could visualize the dynamic turbulence generation to be caused by leading edge vortex generators (in form of roughness spots), for which the vortex strength would be dependent upon the motion induced translatory velocity at the leading edge. This would explain the observed dynamic overshoot, and the leading edge translatory velocity* seems to supply the right correlation between oscillatory data obtained in pure translation and pure pitching motions (Ref. 27). Vortex generators have been found to be as effective as boundary layer suction in increasing the maximum lift (Ref. 33), and suction effectiveness has been shown to increase by as much as 50% when the suction slot is moved from three percent ($\xi = .03$) to one percent ($\xi = .01$) chord position (Ref. 34). The "flabby skin" effect on a sail-wing airfoil, giving infinite Reynolds number type of maximum lift ($C_{L_{max}} = 1.68$) at nominal Reynolds number of less than 1.5 million (Ref. 35), must also have been concentrated to the leading edge region.

The observed sensitivity of $C_{L_{max}}$ to leading edge roughness also suggests the possibilities of an increase of the effective Reynolds number. Leading edge roughness decreases $C_{L_{max}}$ if applied on the leeward side (Ref. 26 and Fig. 8b); increases it when applied to the windward side (Ref. 36). In the former case boundary layer thickening dominates; in the latter the improvement of boundary layer shape parameter is the dominant effect. One could speculate that such a leading edge roughness effect could be sensitive to the magnitude and direction of the leading edge movement, generating favorable effects on the upstroke, unfavorable on the down stroke, thus explaining the large overshoot and undershoot of static stall observed on oscillating airfoils (Refs. 2, 4, 6, 27, and 37.).

The only other mechanism, besides oscillation induced turbulence, that is not simulated in a quasi-steady modeling, is the moving wall effect. It was shown earlier, Eq. (26), that the moving wall effect on the pitching airfoil was of negligible magnitude.

*Relative to a reference point on the airfoil

However, a suddenly stopped wall would generate a wall-jet effect that might not be negligible. The "decelerating wall" around the leading edge of the moving airfoil generates such a wall-jet effect (Fig. 9). As the wing pitches upward the flow velocity at the leading edge surface is equal to the leading edge velocity ($U_{LE} = \xi_{CG} c\dot{\theta}/U_\infty$), thus satisfying the no slip condition at the surface. When this flow rounds the corner to the upper surface of the airfoil the tangential velocity of the wall decreases very rapidly and the near-wall-boundary-layer is left with an excess velocity. This leading edge induced wall-jet-effect fills out the profile near the wall, thus strengthening the boundary layer (Fig. 9a). On the downstroke the leading edge accelerates the flow downward causing a separation-prone boundary layer profile (Fig. 9b).

Perhaps it is easier to visualize the decelerating wall effect by the "roller-bearing" analogy in the flow sketches of Fig. 10. The pitching leading edge is similar to the rotating cylinder which produces a viscous flow about the cylinder that is independent of external flow. Add to this the normal boundary layer on the adjacent fixed wall; and the result is a strengthened boundary layer on the top of the fixed wall (which is analogous to the upper surface near the leading edge of the wing during the upstroke, Fig. 9a); and separated boundary layer on the bottom of the wall (which is analogous to the part of the wing forward of the stagnation point during the downstroke, Fig. 9b).

The "wall-jet-velocity" induced by the decelerating wall can be estimated from Eq. (26). A lumped measure of it is

$$\frac{U_{w_j}}{U_\infty} = \left[U_w(\xi = 0) - U_w(\xi)\right] \Big/ U_\infty$$

Eq. (27) gives

$$\frac{U_{w_j}}{U_\infty} = \left(\xi_{CG} - \frac{\xi_{CG} + \xi}{\left(1 + 2\xi/\rho_N\right)^{1/2}}\right) \frac{c\dot{\theta}}{U_\infty} \qquad (28)$$

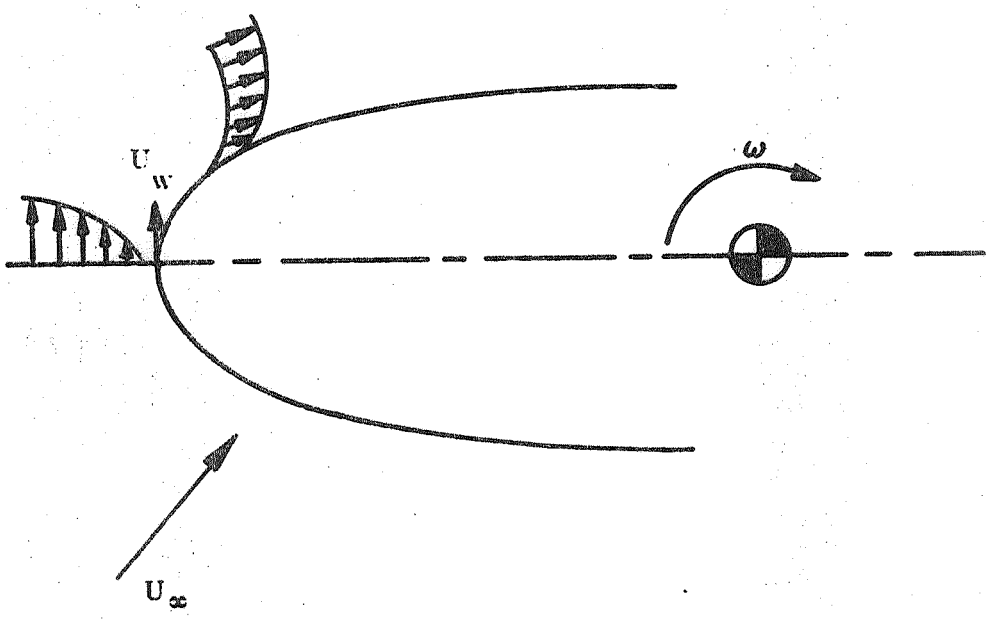

a. UPSTROKE

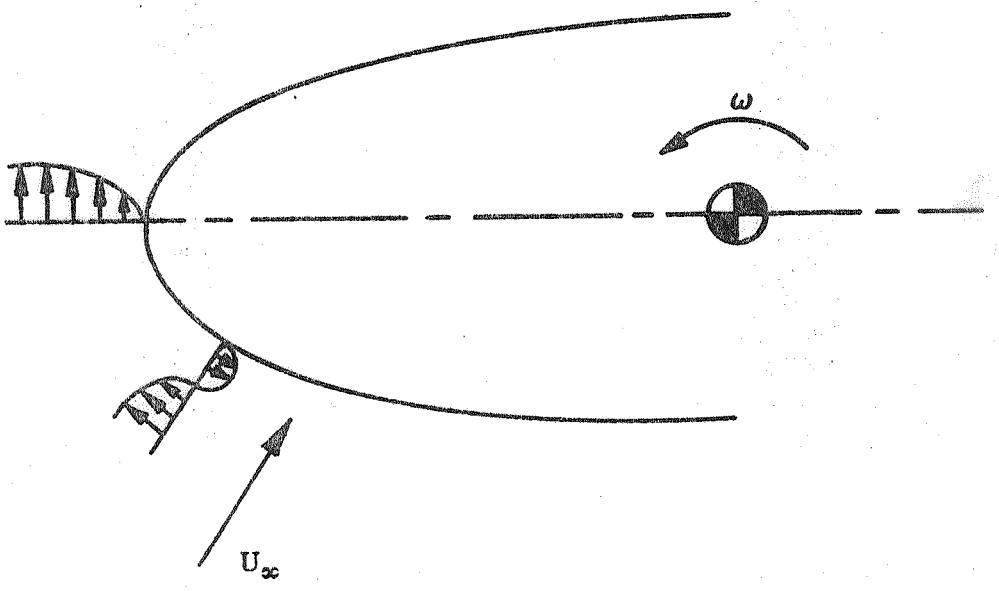

b. DOWNSTROKE

Figure 9 Pitch Rate Induced Decelerating Wall Effect

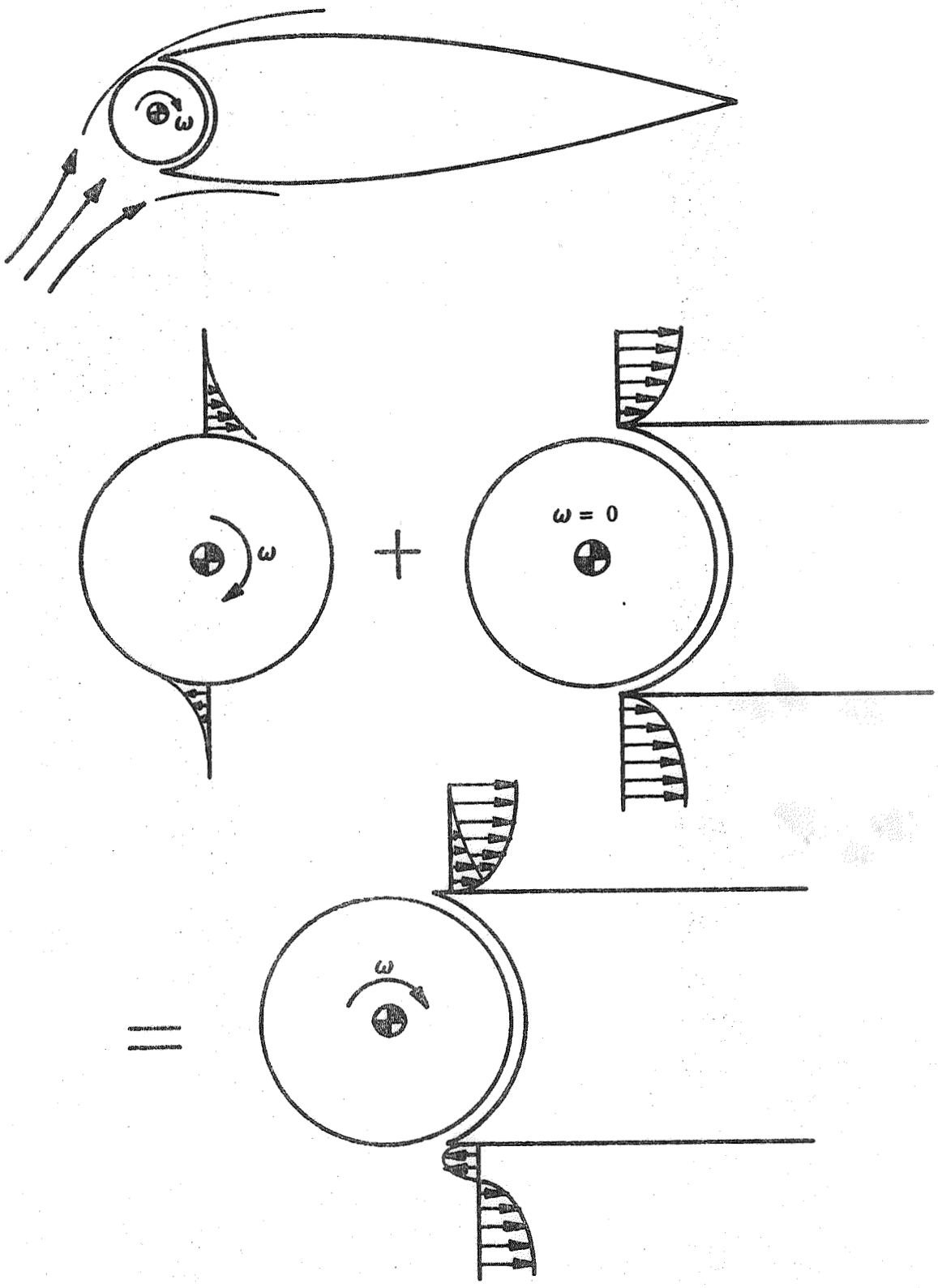

Figure 10 Pitch Rate Induced Leading Edge Wall Jet Effect

Translation:

$$\frac{U_{w_j}}{U_\infty} = -\left(\frac{\rho_N}{2\xi}\right)^{1/2} \frac{\dot{z}}{U_\infty} \tag{29}$$

It has been found that wall-jets that are too small to be traceable in the measured boundary layer velocity profiles can eliminate the leading edge separation bubble (Refs. 17 and 38, and Fig. 11). One can, therefore, suspect that the wall-jet effects of the moving airfoil, Eqs. (28) and (29), could be of sufficient strength to cause a large dynamic overshoot of static stall. The effect is reversed on the downstroke, causing a similarly large dynamic undershoot of static reattachment. This dynamic overshoot $(\Delta\alpha_{s_2})$ of the static stall angle (α_s) can be written

$$\Delta\alpha_{s_2} = K_{a_2} \frac{U_{w_j}}{U_\infty} \tag{30}$$

Of all the possible contributors to dynamic stall overshoot that we have examined, only two seem to be of significance, viz., $\Delta\alpha_{s_1}$ of Eq. (21) and $\Delta\alpha_{s_2}$, Eqs. (28) - (30). To what degree the two components contribute can probably only be determined by systematic dynamic tests. However, the following observations can be made based upon the developed analytic formulations.

For leading edge separation the accelerated flow effect does not induce any time lag effect, neither can the decelerating-wall-induced wall-jet effect be associated with any significant time lag (in addition to the regular Karman-Sears vortex-wake lag).

The accelerated flow induced overshoot $\Delta\alpha_{s_1}$ is not sensitive to pitch oscillation center (ξ_{CG}); the apparent wall-jet effect $\Delta\alpha_{s_2}$ is. Consequently, a test series with varying oscillation center could define the significance of the wall-jet effect relative to the accelerated flow effect.

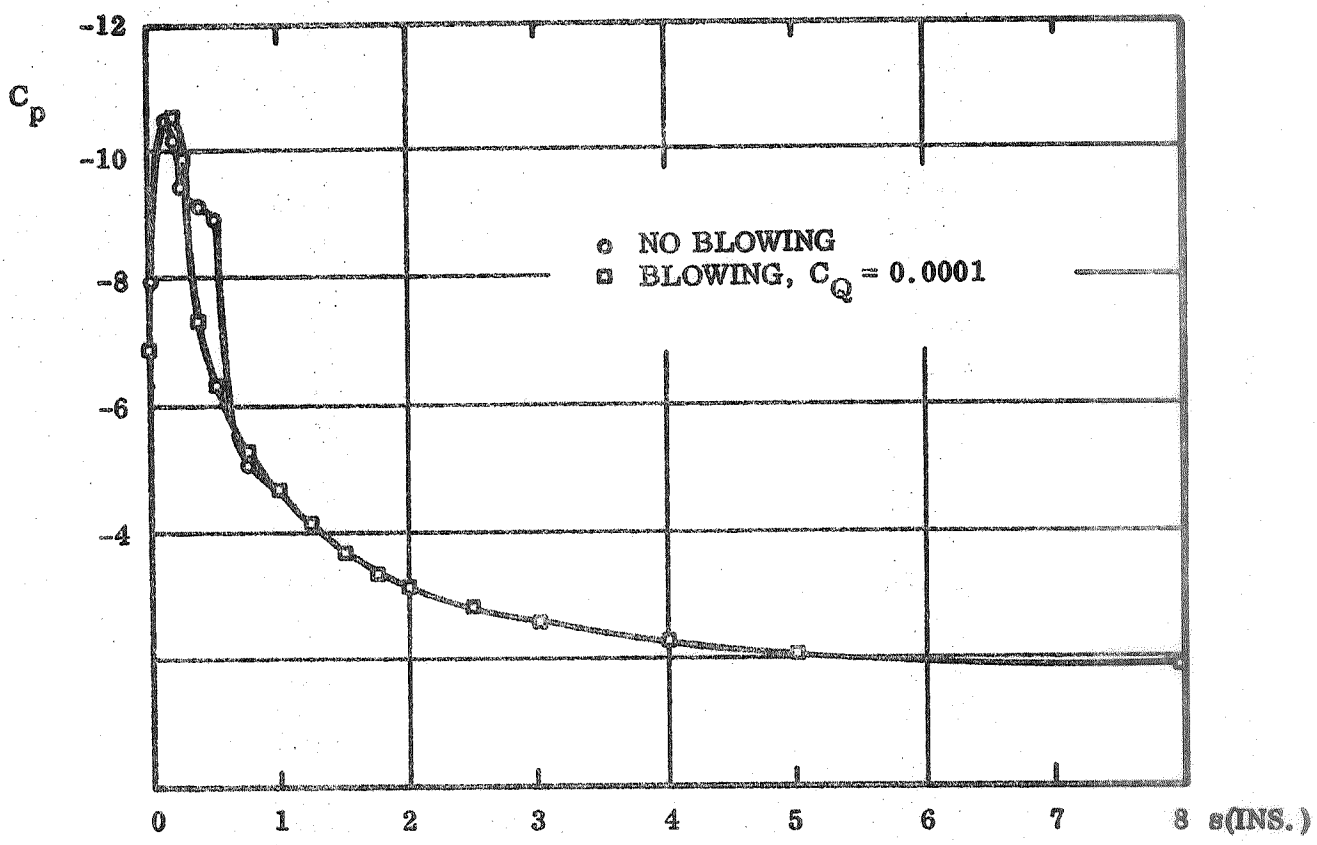

a. Pressure Distribution

Figure 11 Effect of Leading Edge Wall Jets on Laminar Separation and Leading Edge Stall

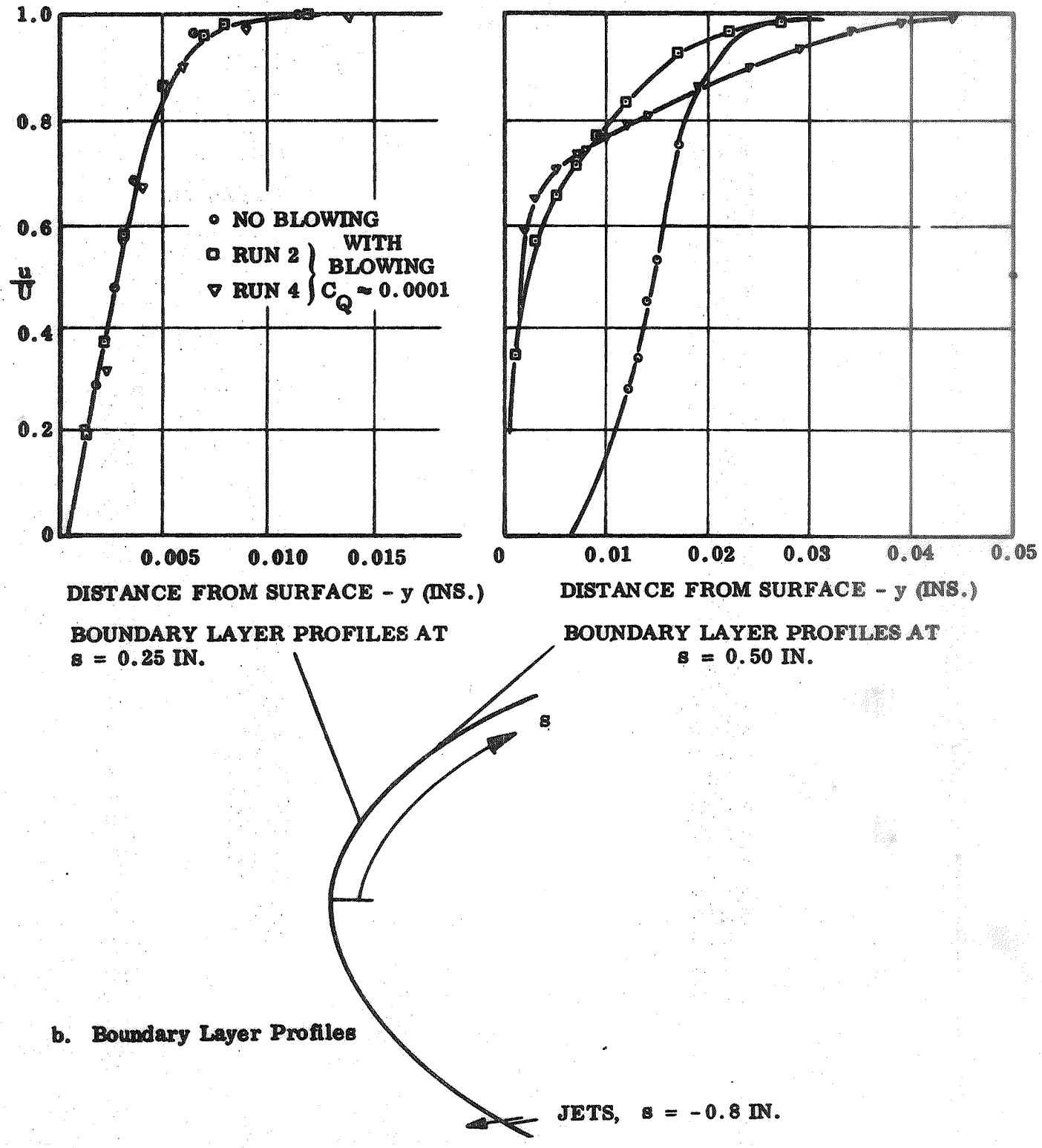

b. Boundary Layer Profiles

Figure 11 Effect of Leading Edge Wall Jets on Laminar Separation and Leading Edge Stall

Regardless of the outcome of such tests, the present analysis shows that both the pitching and translating airfoil will have dynamic overshoots of the static stall which can be formulated in the following manner:

$$\Delta\alpha_{s_{\dot{\theta}}} = K_{a_{\dot{\theta}}} \cdot \frac{c\dot{\alpha}}{U_\infty} \leq \Delta\alpha_{s_{max}} \tag{31}$$

$$\Delta\alpha_{s_{\dot{z}}} = K_{a_{\dot{z}}} \cdot \frac{\dot{z}}{U_\infty} \leq \Delta\alpha_{s_{max}} \tag{32}$$

$\Delta\alpha_{s_{max}}$ is the infinite Reynolds number limit.

2.2 COMPRESSIBLE FLOW AND SHOCK-INDUCED SEPARATION

At high subsonic Mach numbers the flow separation on the airfoil is caused by the normal shock terminating a local supersonic flow region (Ref. 39 and Fig. 12). Originally when angle of attack is increased, the shock and associated flow separation moves downstream (Ref. 40 and Fig. 13a). That is, the behavior is that expected for inviscid flow where the increasing leeward side Mach number with increasing angle of attack causes the shock to move downstream. This separation is very localized, with little effect on overall airfoil characteristics. Finally, however, when the separation bubble reaches the trailing edge, the increasing recompression demand with increasing Mach number (due to increased α) can no longer be met without extending the bubble size (as the recompression efficiency remains unchanged). Thus, the shock has to move forward with increasing angle of attack (and the resulting increased shock strength) until it finally takes the shape of a shock-augmented leading edge separation (Fig. 13b). This is typical for low speed airfoils, such as NACA-0012, with "peaky" velocity distribution (Ref. 41).

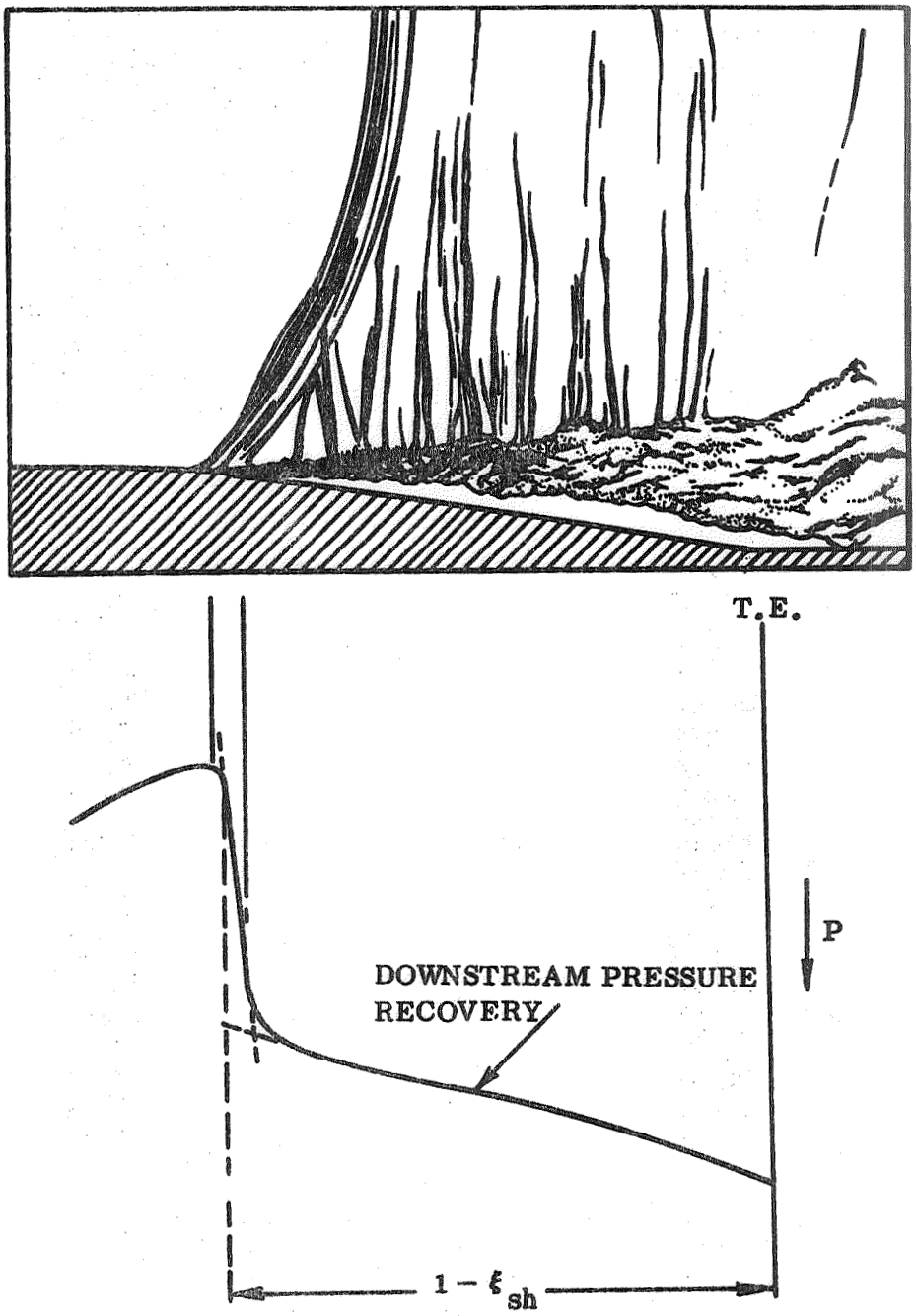

Figure 12 Shock Induced Boundary Layer Separation

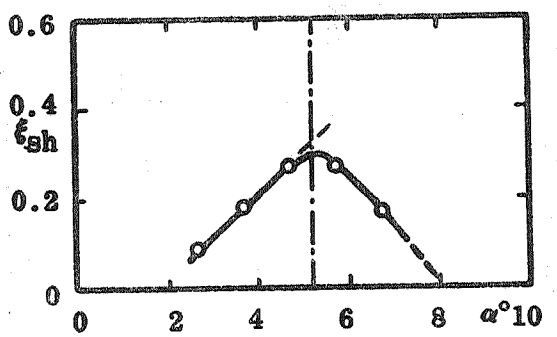

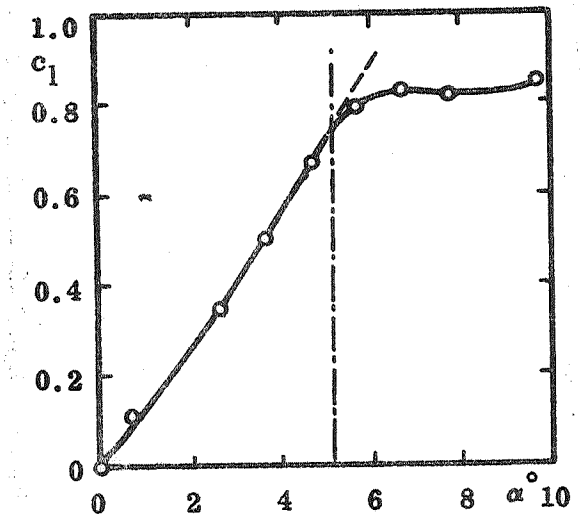

a. Angle of Attack at M = 0.75

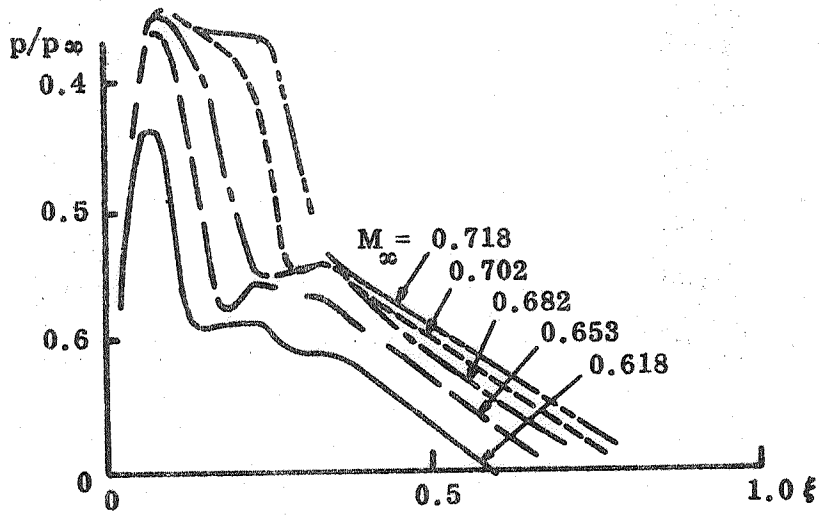

b. Mach Number at $\alpha = 3°$

Figure 13 Effect of Flow Parameters on Shock-Induced Separation

On high speed airfoils with "flat top" velocity distribution, the separation bubble has been observed to expand suddenly to reach the trailing edge when the forward leg of the lambda shock does not generate a subsonic downstream flow (Refs. 39 and 40). This "supersonic tongue" effect with its converging stream lines causes an additional "lift-off" of the separating boundary layer with resultant increase of the separation bubble. How this turning point varies with Mach number and angle of attack for a 6% thick airfoil is shown in Figure 14 (Ref. 40). At low Mach numbers also this airfoil approaches leading edge stall conditions.

For the short separation bubble upstream of the trailing edge, the adverse pressure gradient at separation is determined by the shock strength. However, once the separation bubble extends beyond the trailing edge, the situation approaches that for regular base flow; i.e., there is a direct coupling between lower and upper sides via upstream communication through the wake recompressing region (Ref. 25). The shock on the leeward side can be forced upstream by changing the trailing edge pressure; e.g., by using a spoiler on the windward side (Ref. 40 and Figure 15). Thus, changes in the flow along the wake play a vital part in the development of shock induced separation -- as it does also in low speed stall! The change in trailing edge pressure reflects a change in circulation lift, and one could, therefore, assume that the Karman-Sears vortex-wake model would apply also for this large shock-induced separation bubble. In the limit for high angle of attack, the shock induced separation has converted completely into a leading edge separation, augmented by a normal shock (Ref. 40, Fig. 13b). The Karman-Sears vortex wake effects apply, of course, in this case, and there is no real reason to believe that any drastic changes from this wake model occur as long as the trailing edge pressure dictates the shock position. That is, for the large shock-induced separation of interest in our analysis, the same vortex wake lag effects apply as in the low speed stall.

When the shock is standing near the leading edge, also the boundary layer development and its effect on the airfoil stall will be similar to the incompressible case, Eqs. (3) - (12). That is, the mathematical models for the accelerated flow and decelerating wall effects remain valid, but the magnitude of the induced effects changes because of compressibility effects. Thus, we find that the dynamic overshoot

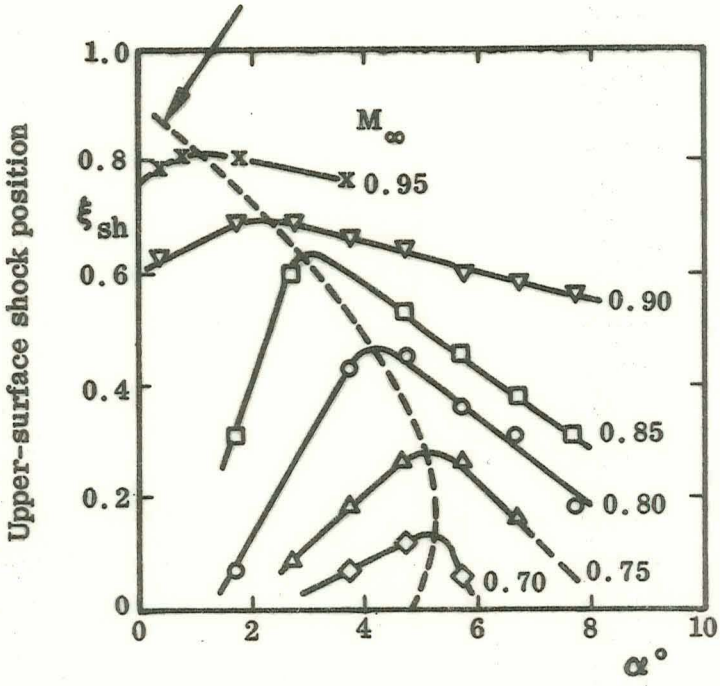

Figure 14 Effect of Mach Number and Angle of Attack on Initiation of Large Separation Bubble

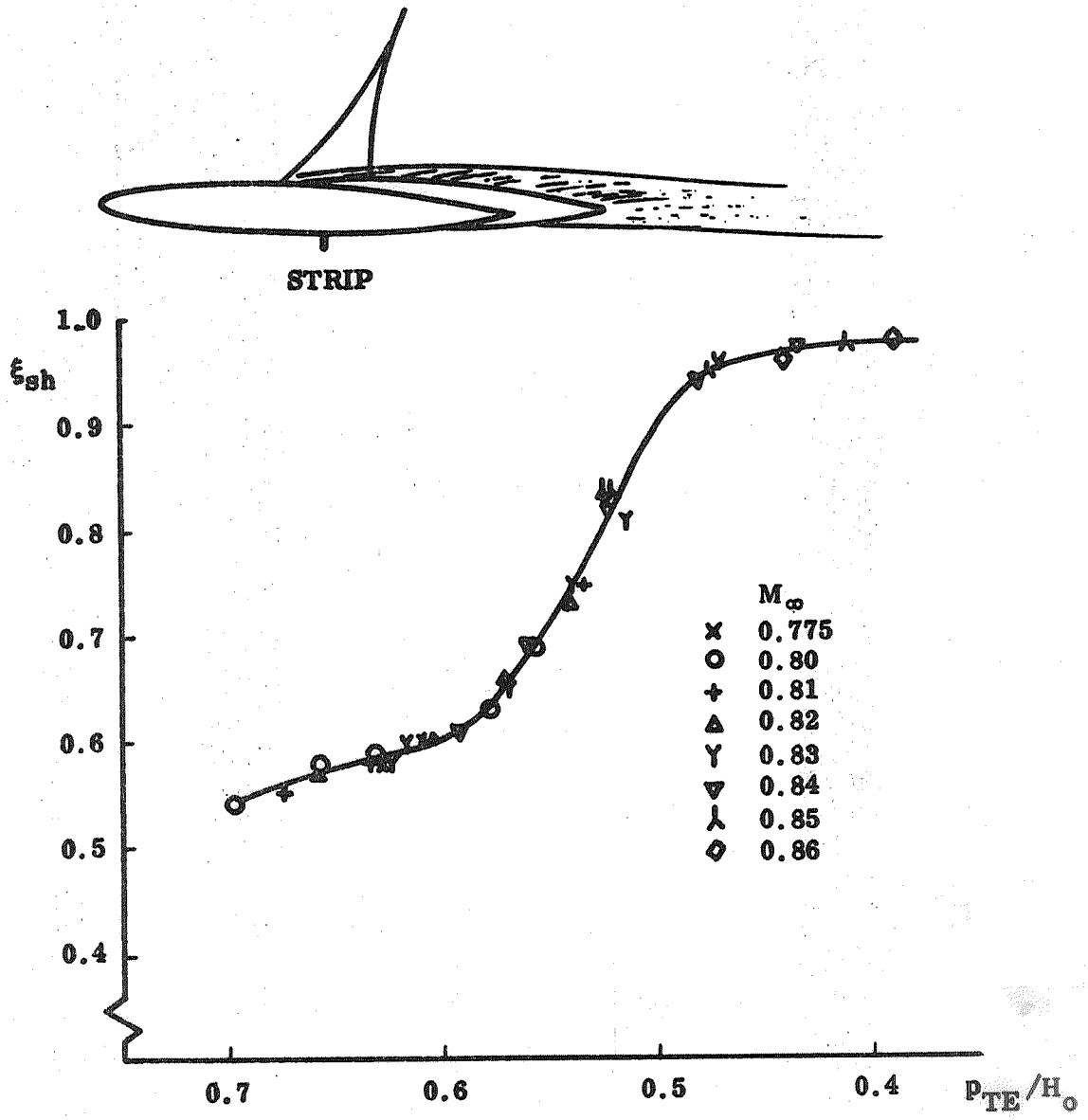

Figure 15 Trailing Edge Control of Shock Position

of leading edge stall* decreases with increasing Mach number** to reach a minimum in the range $0.4 < M < 0.6$ (Ref. 29, Figure 16). The beneficial effects of leading edge modification on static stall show similar Mach number dependence (Ref. 24 and Fig. 17a), whereas the effect of camber shows no such Mach number dependence (Ref. 42 and Fig. 17b). This indicates that the extensive leading edge modification with its redistribution of curvature and associated pressure gradient history is able to improve the boundary layer less the higher the subsonic Mach number is. That is, the compressibility effects severely restrict the latitude for boundary layer improvement. This is, of course, to be expected, as a straightforward application of the Prandtl-Glauert compressibility factor says that the same nose appears blunter to the flow the higher the subsonic Mach number is (Ref. 43). That is, the corresponding nose radius in incompressible flow is increased by the factor $(1 - M^2)^{-1/2}$.

The effectiveness of the pitch rate induced leading edge modification is not Mach number sensitive, i.e., the slope $\partial c_{l_{max}} / \partial \left(\frac{c\dot{\alpha}}{U_\infty}\right)$ remains unchanged (Fig. 16a). It is the margin for improvement that decreases with increasing Mach number, i.e., the infinite Reynolds number "$c_{l_{max}}$ - ceiling" is lowered. The pressure gradient redistribution effect, Eq. (21), and the decelerating wall effect, Eqs. (28) - (30), are both limited by this lowered "$c_{l_{max}}$-ceiling" to the same degree. It is only the maximum possible dynamic overshoot that changes with Mach number. That is, the proportionality constants in Eqs. (31) and (32) for the dynamic leading edge effect remain unchanged.

---

*Or laminar trailing edge stall, as is the case for the lowest Reynolds and Mach number where the largest overshoot was realized.

**The simultaneously increasing Reynolds number would have a similar effect on the overshoot, but the effect is negligible compared to the M-effect. In either case, it would not affect the upper bound for the $c_{l_{max}}$ overshoot.

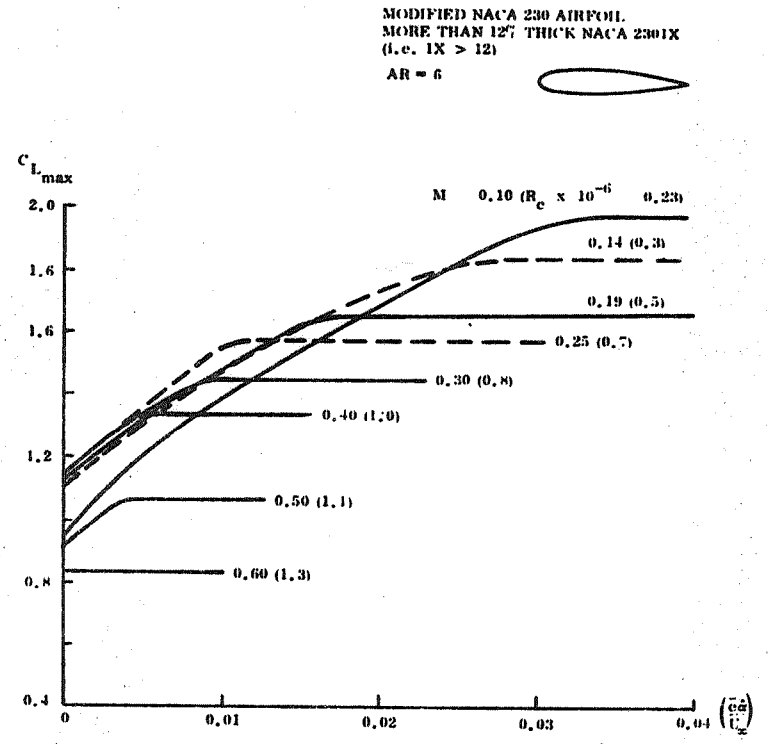

a. $C_{L_{max}}$ as a Function of Pitch Rate

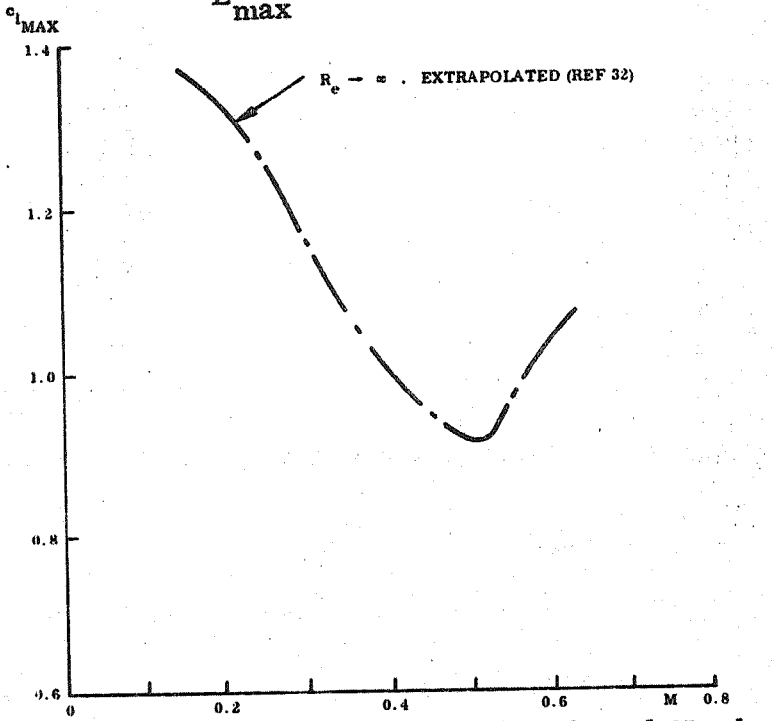

b. Limiting $C_{L_{max}}$ as a Function of Mach Number

Figure 16 Dynamic Overshoot of Static Stall in Airplane Pull-up Maneuvers

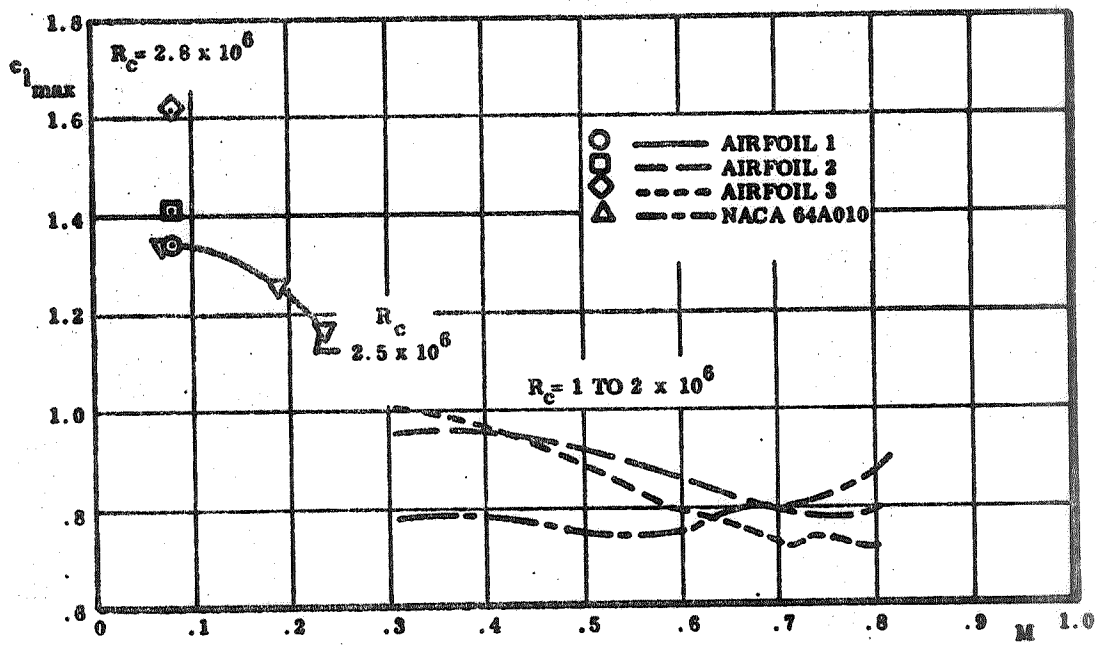

a. Leading Edge Modification

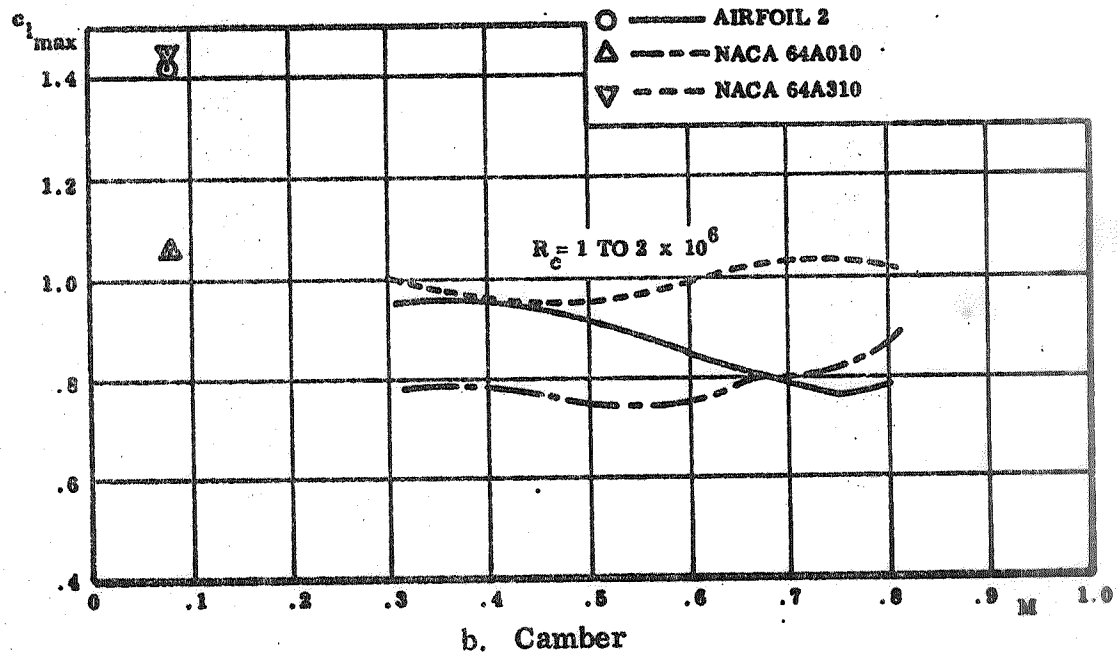

b. Camber

Figure 17 Effect of Mach Number on Effectiveness of High Lift Devices

When the Mach number is increased the shock leaves the leading edge region and starts moving back towards the trailing edge. As more and more boundary layer approach length is added with increasing (subsonic) Mach number, there is room for boundary layer improvement effects and the ceiling for dynamic overshoot effects is raised again (Fig. 16b). At the same time convective time lag effects start to become important (see discussion of Eq. (12)). W. P. Jones shows in his Minta Martin Lecture experimental data for the effect of pitch-up rate on the leeward side shock position of an airfoil at $M = 0.75$ (Refs. 44 and 45, and Figure 18a). The data show that when angle of attack is increased at a steady rate, $c\dot{\alpha}/U_\infty = 0.0059$, the shock is lagging the airfoil motion. The shock is also found to exhibit high frequency oscillations around some quasi-steady position.

One cause for the lag of the shock relative to the airfoil instantaneous angle of attack is, of course, the Karman-Sears wake lag. There is an additional delaying effect generated by the shock (and separation) movement itself. The shock is moving forward relative to the airfoil surface with the speed

$$\Delta U_s = c\dot{\xi}_s = -\frac{\partial \xi_s}{\partial \alpha} c\dot{\alpha} \tag{33}$$

That is, the Mach number ahead of the shock is increased by the amount

$$\frac{\Delta M_s}{M_s} = \frac{\Delta U_s}{U_e} = -\frac{\partial \xi_s}{\partial \alpha} \frac{c\dot{\alpha}}{U_e} \tag{34}$$

Figure 18b shows that this increase of Mach number will slow the forward shock motion down by the amount

$$\Delta \xi_s \left(M_s\right) = \frac{\partial \xi_s}{\partial M_\infty} \frac{M_\infty}{M_e} \Delta M_s \tag{35}$$

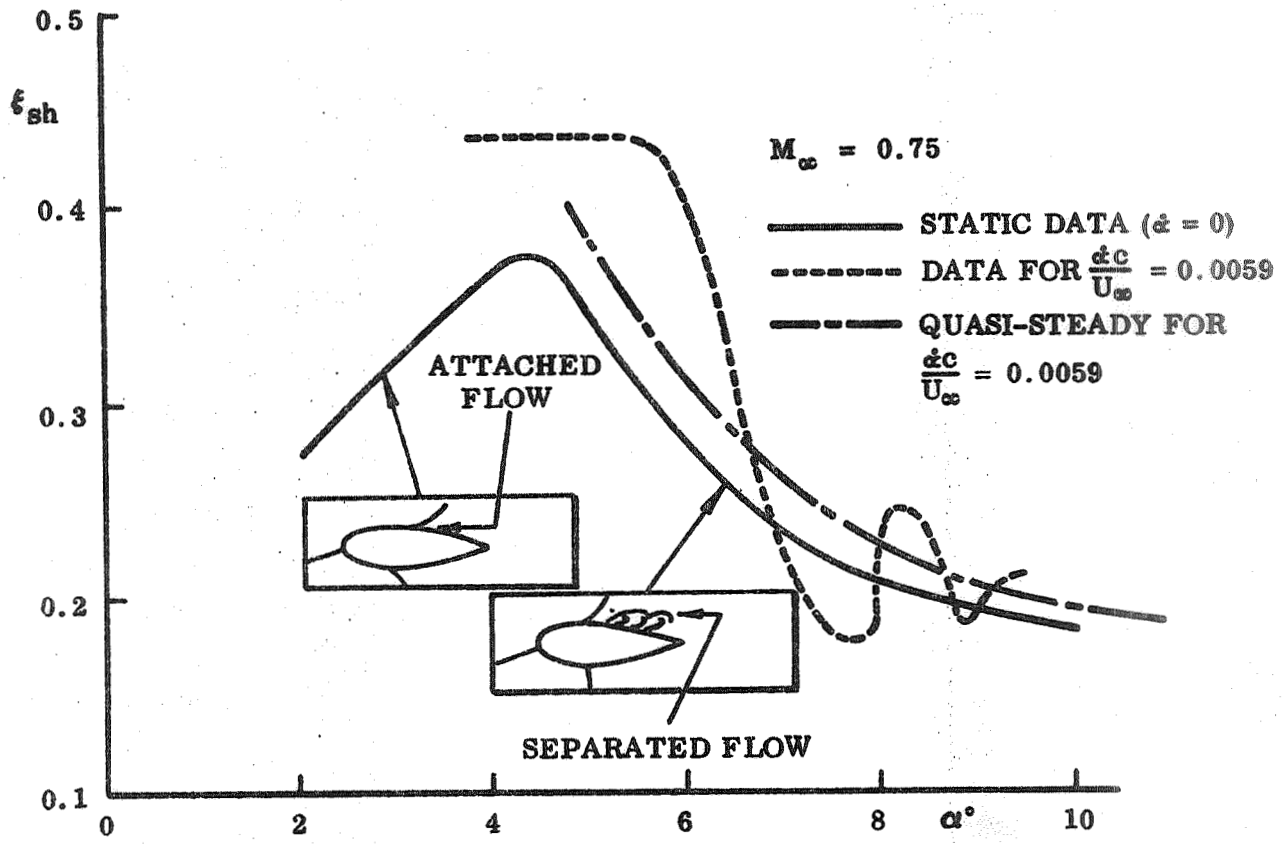

a. Angle of Attack and Angular Rate at M = 0.75

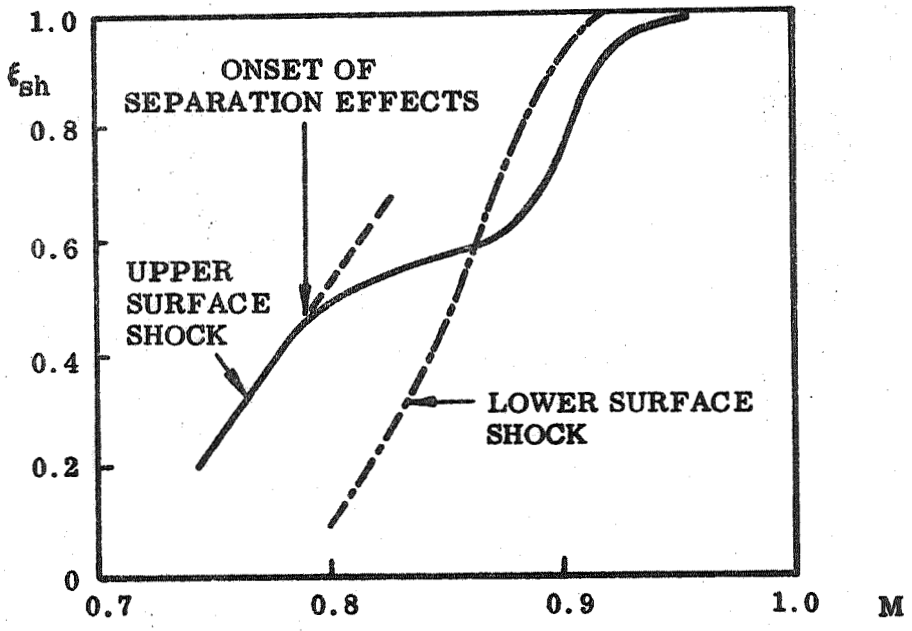

b. Free Stream Mach Number at $\alpha \approx 5°$

Figure 18 Effects of Flow Parameters on Shock Boundary Layer Interaction

The angle of attack can, therefore, be overshot by the amount

$$\Delta\alpha = \dot{\alpha}\ \Delta t_{sh} = \xi_{a_{sh}} \frac{c\dot{\alpha}}{U_e} \tag{36}$$

Eqs. (35) - (36) define the following value for the shock motion induced equivalent time lag

$$\xi_{a_{sh}} = \frac{\partial \xi_s}{\partial M_\infty} M_\infty \tag{37}$$

The quasi-steady lag $\Delta\xi_s$ of the shock induced separation is simply

$$\Delta\xi_s = \frac{\partial \xi_s}{\partial \alpha} \cdot \Delta\alpha \tag{38}$$

The lag angle $\Delta\alpha$ is

$$\Delta\alpha = -\dot{\alpha}\Delta t = -\left(\xi_{a_{sh}} + \xi_w\right) \frac{c\dot{\alpha}}{U_\infty} \tag{39}$$

ξ_w is the Karman-Sears vortex wake lag, $\xi_w = 1.5$. Figure 18b gives $\partial\xi_s/\partial M_\infty = 0.8$ for $M_\infty = 0.75$, and from Eq. (37) $\xi_{a_{sh}} = 0.6$.

Figure 18a gives

$$\frac{\partial \xi_s}{\partial \alpha} = \begin{cases} -4.2 \text{ at } \alpha = 5^\circ \\ -0.8 \text{ at } \alpha = 10^\circ \end{cases}$$

These values in Eqs. (38) and (39) give for $c\dot{\alpha}/U_\infty = 0.0059$

$$\Delta \xi_s = \begin{cases} 0.052 \text{ at } \alpha = 5^\circ \\ 0.010 \text{ at } \alpha = 10^\circ \end{cases}$$

This quasi-steady position is indicated by the dash-dotted line in Figure 18a. It seems to indicate a realistic quasi-steady mean position of the measured shock oscillation. The deviation is a high frequency oscillation with decreasing amplitude and increasing frequency. The α-half periods for the 4 half cycles shown are

$$\Delta\alpha = 2.5^\circ, 1.3^\circ, 0.7^\circ, \text{ and } 0.5^\circ$$

The corresponding angular frequencies are

$$\tilde{\omega} = \frac{\omega c}{U_\infty} = \frac{\pi}{\Delta\alpha}\frac{\dot{\alpha}c}{U_\infty} = \frac{180}{\Delta\alpha^0}\frac{\dot{\alpha}c}{U_\infty} = 0.425, 0.815, 1.52, \text{ and } 2.13$$

Examining this high frequency oscillation further reveals that its amplitude and frequency vary with α in a manner prescribed by the shock sensitivity to angular changes, $\partial \xi_s/\partial\alpha$. This is demonstrated in Figure 19, which shows that

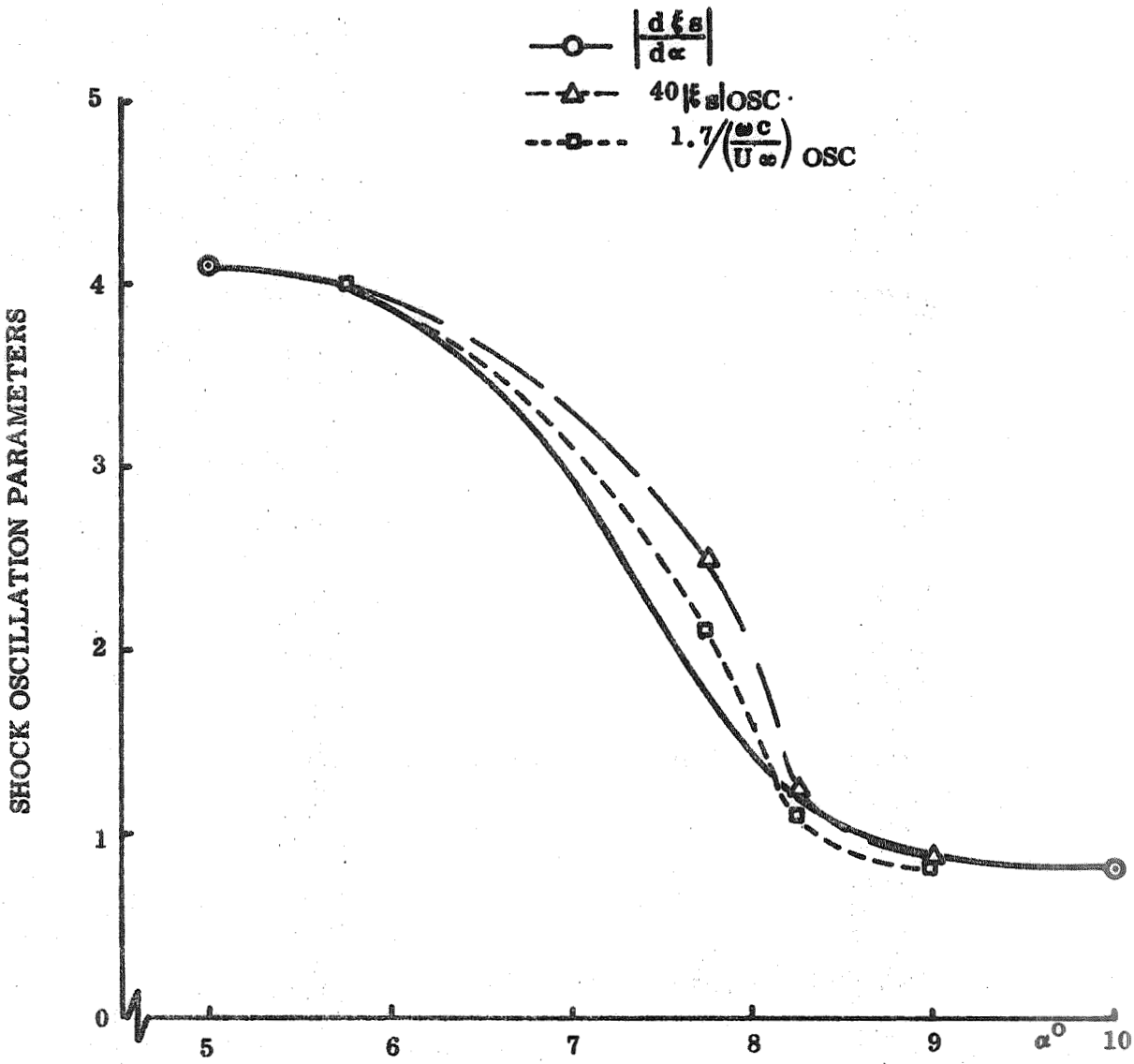

Figure 19 Oscillatory Shock Motion Parameters

$$\left|\xi_s\right|_{osc} \approx 0.025 \left|\frac{\partial \xi_s}{\partial \alpha}\right| \tag{40}$$

$$\left|\xi_s\right|_{osc} \bar{\omega}_{osc} \approx 0.0425 \tag{41}$$

As Trilling has found that shock boundary layer interactions can generate harmonic self-sustained oscillations (Ref. 46), one suspects that the present shock oscillations also are of harmonic nature. Such an oscillation can be as expressed as

$$\frac{d^2 \Delta^i \xi_s}{dt^2} + 2\zeta\omega \frac{d\Delta^i \xi_s}{dt} + \omega^2 \Delta^i \xi_s = 0 \tag{42}$$

where

$$\Delta^i \xi_s = \xi_s - \left(\xi_s\right)_{QS}$$

Using the dimensionless time $\tau = \left(\frac{U_\infty}{c}\right)t$ (time unit = time for airfoil to travel one chord length), Eq. (42) becomes

$$\frac{d^2 \Delta^i \xi_s}{d\tau^2} + 2\zeta\bar{\omega} \frac{d\Delta^i \xi_s}{d\tau} + \bar{\omega}^2 \Delta^i \xi_s = 0 \tag{43}$$

The solution to Eq. (43) is (see for example Ref. 47)

$$\Delta^i \xi_s(\tau) = \frac{\Delta^i \overset{\circ}{\xi}_s(0)}{\bar{\omega}^2\left(1 - \zeta^2\right)^{1/2}} e^{-\zeta\bar{\omega}\tau} \sin\left(\bar{\omega}\tau\left[1 - \zeta^2\right]^{1/2}\right) \tag{44}$$

where $\Delta^i \xi_s(0) = 0$ and $\frac{d\Delta^i \xi_s(0)}{d\tau} = \Delta^i \dot{\xi}_s(0)$ are the initial conditions.

If the damping as a fraction of critical, ζ, is assumed to be small, $\zeta^2 \ll 1$, Eq. (44) becomes

$$\Delta^i \xi_s(\tau) = \frac{\Delta^i \dot{\xi}_s(0)}{\bar{\omega}} \sin(\bar{\omega}\tau) \tag{45}$$

That is,

$$\left|\Delta^i \xi_s\right|_{\bar{\omega}} = \Delta^i \dot{\xi}_s(0) = \text{constant in accordance with Eq. (41).}$$

The initial rate $\Delta^i \dot{\xi}_s(0)$ can be determined as follows

$$\Delta^i \dot{\xi}_s(0) = \frac{\partial \Delta^i \xi_s}{\partial \alpha} \frac{c\dot{\alpha}}{U_\infty}$$

$\frac{\partial \Delta^i \xi_s}{\partial \alpha} = \frac{\partial}{\partial \alpha}\left[\xi_{sh} - \xi_s\right]$, where ξ_{sh} is the shock position for essentially attached flow, i.e., small separation bubble. Thus

$$\Delta^i \dot{\xi}_s(0) = \left[\frac{\partial \xi_{sh}}{\partial \alpha} - \frac{\partial \xi_s}{\partial \alpha}\right] \frac{c\dot{\alpha}}{U_\infty} \tag{46}$$

and Eq. (45) becomes

$$\Delta^i \xi_s(t) = \left[\frac{\partial \xi_{sh}}{\partial \alpha} - \frac{\partial \xi_s}{\partial \alpha}\right] \frac{c\dot{\alpha}}{U_\infty} \frac{1}{\bar{\omega}} \sin(\omega t) \tag{47}$$

From Figure 18a the shock derivatives at $\alpha = 5°$ are

$$\frac{\partial \xi_{sh}}{\partial \alpha} = 2.9 \; ; \; \frac{\partial \xi_s}{\partial \alpha} = -4.2$$

For $\dot{\alpha} c/U_\infty = 0.0059$ Eq. (46) gives $\Delta^i \overset{\circ}{\xi}_s(0) = 0.042$ and Eq. (47) becomes

$$\Delta^i \xi_s(0) = \frac{0.042}{\bar{\omega}} \sin(\omega t)$$

That is

$$\left| \Delta^i \xi_s \right| \bar{\omega} = 0.042$$

which is in excellent agreement with Eq. (41).

The self-sustained oscillations for laminar shock-boundary layer interactions predicted by Trilling (Ref. 46), and measured by Fizdon (Ref. 48), had characteristic frequencies that could be defined in two alternate ways (Ref. 46 and Fig. 20)

$$K = \omega l/U \tag{48}$$

$$k = \omega L/U_\infty = K/2 S_e^{\eta} \left(\Delta C_{p_{sh}} \right)_e \tag{49}$$

where $K = 1.79$ was the value for the lowest harmonic. Only when the shock has moved away from the trailing edge (control) can we expect the shock oscillation to be similar to the free interaction case treated by Trilling. At $\alpha = 10°$ the trailing edge influence, as reflected in $\partial \xi_s / \partial \alpha$, has dropped drastically and the similarity may exist.

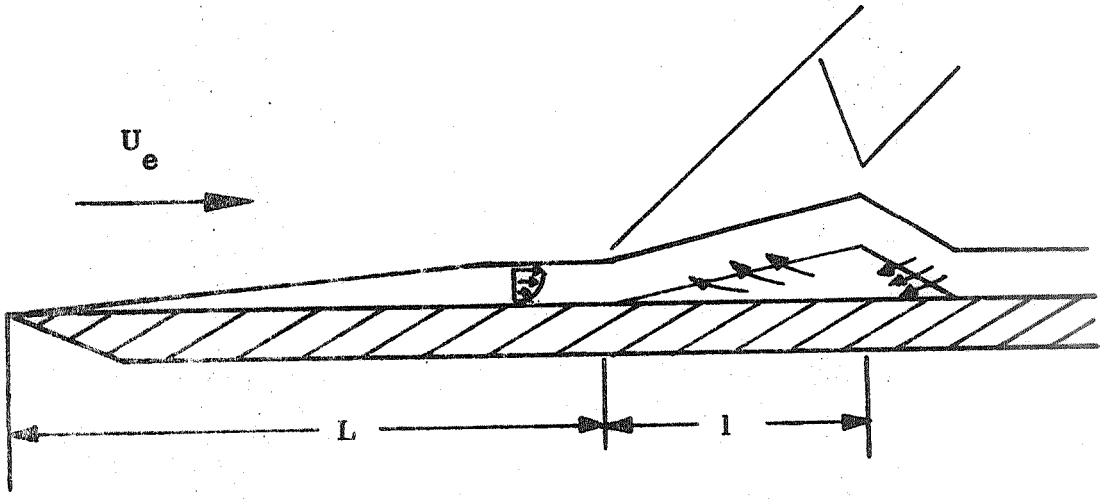

Figure 20 Shock-Induced Laminar Boundary Separation on a Flat Plate

Substituting $\xi_s c$ for L we get for the present case

$$k = \bar{\omega}\xi_s = K/2\, S_e^{n} \left(\Delta C_{p_{sh}}\right)_e$$

$$S_e = \rho_e/\rho_{wall} = \left(1 + 0.2\, M_e^{2}\right)^{-2.5} \tag{50}$$

$$\left(\Delta C_{p_{sh}}\right)_e = \left(\frac{\hat{p}_e}{p_e} - 1\right) / 0.7\, M_e^{2}$$

with $\hat{p}_e/p_e \approx 1.4$ (Ref. 40), $n \approx 3/4$ (Ref. 49) and $K = 1.79$, Eq. (50) gives

$$k = \bar{\omega}\xi_s = 0.43 \text{ ; i.e. } \bar{\omega} \approx 2.15 \text{ for } \xi_s \approx 0.2$$

This is admittedly in too good agreement with the value of $\bar{\omega} = 2.13$ actually measured. A value 25% off would have been more comfortable, as we only want to show the similarity between the present airfoil shock oscillation for $\alpha = 10°$ and the flat plate case treated by Trilling, both cases dealing with laminar boundary layer shock interaction.

When the shock is near the trailing edge, $\alpha = 5°$, it is a wake dominated situation similar to that for aft body separation off bulbous bases (Ref. 25). If we assume the "wake neck" to be very close to the trailing edge, as it would be for starting large bubble separation, we may substitute l with the distance from separation to trailing edge and back again.

$$k = 2\bar{\omega}\left(1 - \xi_s\right) \Big/ \frac{\bar{U}}{U_\infty} \tag{51}$$

with $K = 1.79$, $\bar{\omega} = 0.425$, and $\xi_s = 0.35$ Eqs, (50) and (51) give the mean wake velocity (at $\alpha = 5°$, Fig. 18a) $U/U_\infty \approx 0.31$, which is not unreasonable (Ref. 50).

The present calculations would predict that doubling the pitch rate $c\dot{\alpha}/U_\infty$ would give twice the quasi-steady displacement in Fig. 18a and the oscillation would have double the amplitude and half as many cycles (Eq. 47). That is, the analytic methods developed here will predict both the quasi-steady shock position and the associated high frequency oscillation, using static experimental data as the only input.

In order to be able to compute the unsteady aerodynamics one needs to determine the force change associated with the shock movement. Acoording to Pearcey (Ref. 40) the strength of the shock remains relatively constant, being determined by the pressure increase the upstream boundary layer can stand without separation. The pressure ratio through the shock is

$$\hat{p}_e/p_e \approx 1.4$$

At the turning point between small bubble separation, or essentially attached flow, and large separation, e.g., $\alpha = 5°$ in Fig. 18a, one knows enough to determine the separation induced load. That is

$$\Delta^i c_{n_{\alpha_s}} = \Delta C_{p_s}\left[\frac{d\xi_{sh}}{d\alpha} - \frac{d\xi_s}{d\alpha}\right] = \Delta C_{p_s}\frac{d\Delta^i\xi_s}{d\alpha} \tag{52}$$

$$\Delta C_{p_s} = \left(\frac{\hat{p}_e}{p_e} - 1\right)\frac{2}{\gamma M_\infty^2}\frac{p_e}{p_\infty} = \frac{4}{7}\frac{1}{M_\infty^2}\left[\frac{1 + 0.2\,M_\infty^2}{1 + 0.2\,M_e^2}\right]^{3.5}$$

where $M_e^2 \approx 2$ (Ref. 40)

The corresponding unsteady load is

$$\Delta^i c_{n_{sh}}(t) = \Delta^i c_{n_{\alpha_{sh}}} \tilde{\alpha}(t - \Delta t)$$

$$\Delta t = \left(\xi_{a_{sh}} + 1.5\right) c/U_\infty \tag{53}$$

$$\tilde{\alpha} = \alpha_o + \theta + \left(0.5 - \xi_{CG}\right) c\dot{\theta}/U_\infty$$

That is, for slow oscillations (See Eq. (11))

$$\Delta^i c_{n_{\dot{\theta}_{sh}}} = \frac{\partial \Delta^i c_{n_{sh}}}{\partial\left(\frac{c\dot{\theta}}{U_\infty}\right)} = - \Delta^i c_{n_{\alpha_{sh}}} \left(\xi_{a_{sh}} + 1.5\right)$$

and

$$\left.\begin{aligned} \Delta^i c_{m_{\dot{\theta}_{sh}}} &= - \Delta^i c_{m_{\alpha_{sh}}} \left(\xi_{a_{sh}} + 1.5\right) \\ \Delta^i c_{m_{sh}} &= - \Delta^i c_{n_{\alpha_{sh}}} \left(\xi_s - \xi_{CG}\right) \end{aligned}\right\} \tag{54}$$

It can be seen that Pete Jordan's rule of the double R's (Ref. 51) is valid for this separation induced effect (as it is for most). The "Reversed Reactions" rule says that if the separation affects static stability in one way, it will affect the dynamic stability in the opposite direction.

When the shock is not at its turning point, it is more difficult to determine what the separation induced effect is. Going back to Eq. (52), one knows $d\xi_s/d\alpha$ from static data, but does not know $d\xi_{sh}/d\alpha$ (for $\alpha > 5°$ in Fig. 18a, for example). The dilemma is the same as that encountered for the corresponding three-dimensional problem, i.e., shock-boundary layer interaction on cone cylinder bodies (Refs. 10 and 52). The solution is, of course, also the same. That is, one must in some manner determine what the shock position (and shock strength) would have been in attached flow. Sinnot has developed such a prediction method for the airfoil flow (Ref. 53).

When the oscillatory rates are high, one may have to consider the shock strength variation caused by its motion. That is, the Mach number ahead of the shock is increased by the amount ΔM_s, Eqs. (33) and (34), thereby increasing the shock strength.

For a strong shock wave (Ref. 49)

$$\frac{\hat{p}_e}{p_e} - 1 = \frac{2\gamma}{\gamma + 1}\left[M_s^2 - 1\right] \tag{55}$$

The logarithmic differential is

$$\frac{\partial\left(\frac{\hat{p}_e}{p_e} - 1\right)}{\frac{\hat{p}_e}{p_e} - 1} = \frac{\partial\left(\Delta C_{p_{sh}}\right)}{\Delta C_{p_{sh}}} = 2\frac{\Delta M_s}{M_s}\,\frac{M_s^2}{M_s^2 - 1} \tag{56}$$

Thus

$$\Delta C_{p_{sh}} = \left(\Delta C_{p_{sh}}\right)_{\dot{\theta}=0}\left[1 + \frac{2\Delta M_s}{M_s}\,\frac{M_s^2}{M_s^2 - 1}\right] \tag{57}$$

Or with Eq. (34)

$$\left(\Delta C_{p_{sh}}\right)_{\dot{\theta}} = \left(\Delta C_{p_{sh}}\right)_{\dot{\theta}=0} \left[1 - 2 \frac{\partial \xi_s}{\partial \alpha} \frac{M_s^2}{M_s^2 - 1} \frac{c\dot{\theta}}{U_e}\right] \tag{58}$$

A usual approximation for M_s is $M_s = 2^{1/2}$ (Ref. 40)

That is

$$-2 \frac{\partial \xi_s}{\partial \alpha} \frac{M_s^2}{M_s^2 - 1} \frac{c\dot{\theta}}{U_e} = -8 \frac{\partial \xi_s}{\partial \alpha} \frac{c\dot{\theta}}{U_e}$$

For $\partial \xi_s / \partial \alpha = -4.2$ (Fig. 18a) and $\frac{c\dot{\theta}}{U_e} = 0.04$ (Ref. 3) the M_s -term in the bracket of Eq. (58) is not negligible!

2.3 THREE DIMENSIONAL FLOW EFFECTS

It is a rather routine matter to account for aspect ratio in incompressible, attached flows. However, when the flow is separated the correction technique breaks down. For example, Figure 21 compares two dimensional results (Ref. 54) with corrected finite aspect ratio results (Ref. 55). The agreement is good only below stall. The stall is consistently more abrupt for the end plated or two dimensional result. Evidently the tip vortices on the finite aspect ratio configurations vent the stall region resulting in a more gradual loss of lift. The so-called two dimensional results exhibit poor agreement among themselves in the post stall region (Refs. 27, 31, 54, 56, and 58, Fig. 22). Thus, the flow is not truly two dimensional. The interaction between the wind tunnel wall and wing boundary layers generates vortices that act similarly to the traveling vortices for finite span models. Liiva has shown that wall

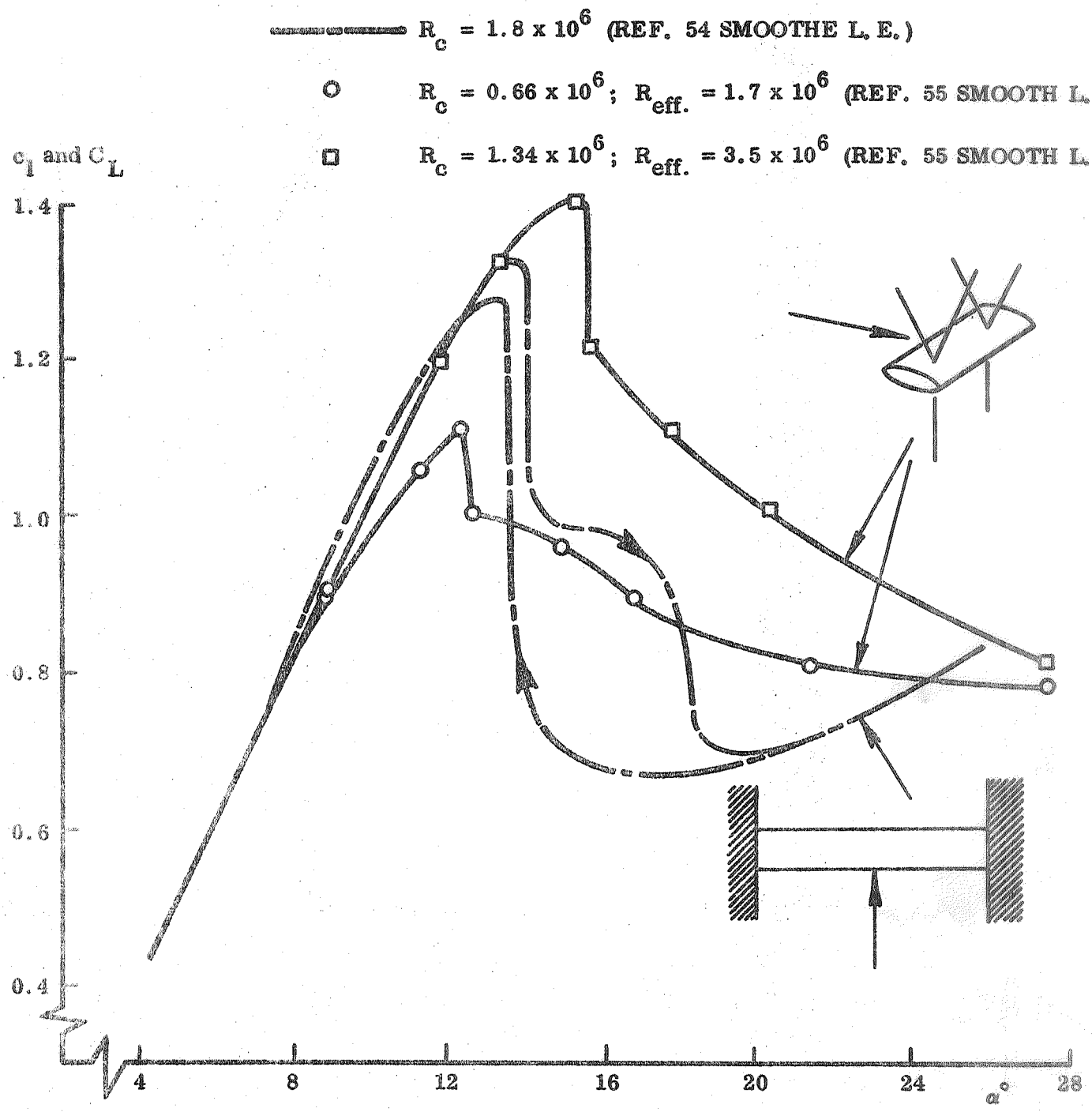

Figure 21 NACA-0012 Lift-Stall Characteristics

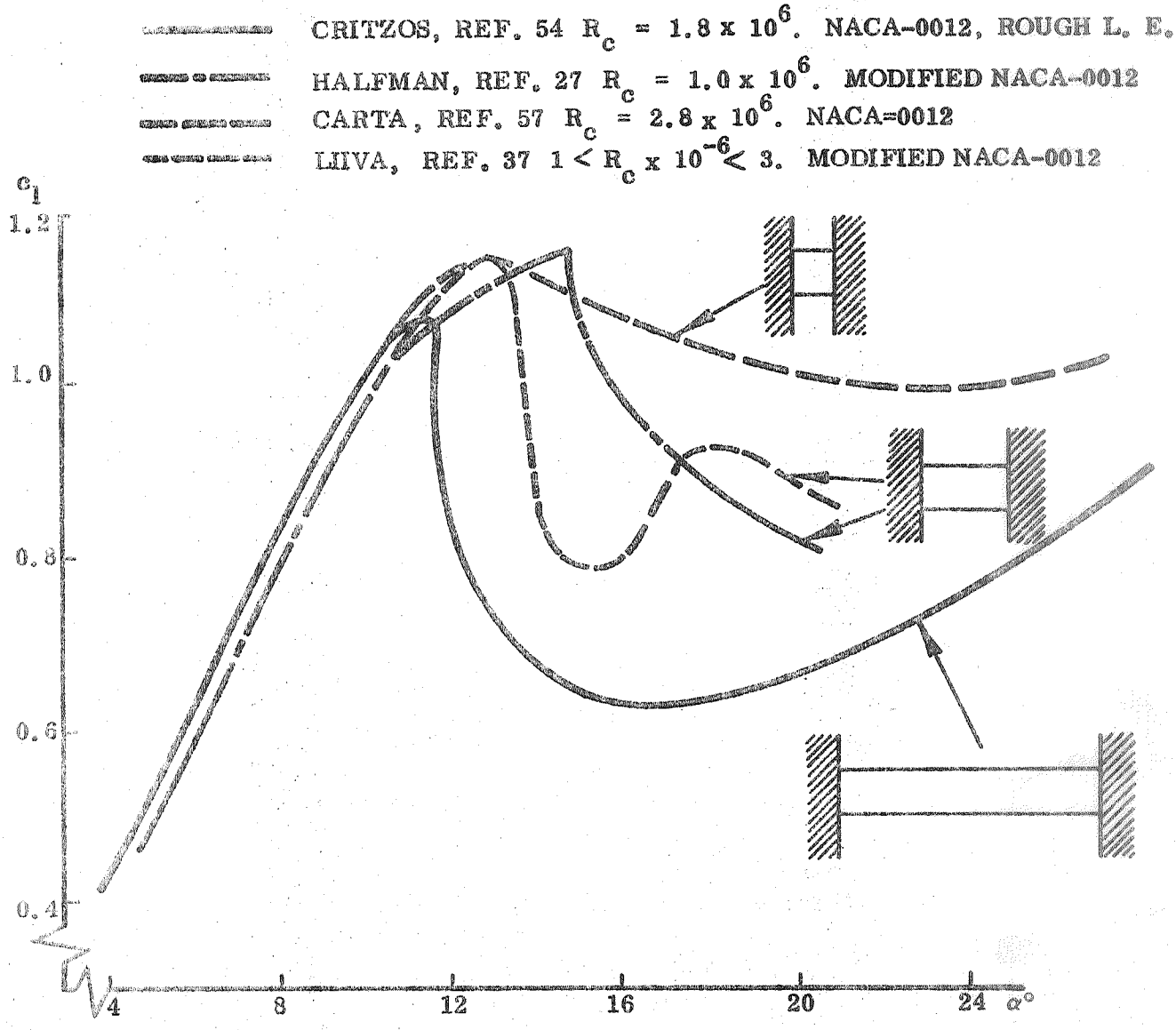

Figure 22 "Two-Dimensional" Stall of the NACA-0012 Airfoil Measured by Various Investigators

(in his case splitter plate) boundary layer control can significantly mitigate this effect (Ref. 37 and Fig. 23). Just how successful this is in simulating truly two dimensional flow is still questionable judging from the post stall "oscillations" of Liiva's static lift data (Fig. 22).

The most strikingly different results are those of Carta (Ref. 56). His lift curve looks more like turbulent trailing edge stall then the leading edge stall which normally occurs on the NACA-0012 airfoil in this range of Reynolds numbers (Refs. 13, 54, and 55). Comparison of lift and moment characteristics reveals that lift stall precedes moment stall, which is characteristic of trailing edge stall (Ref. 55). Carta placed his pressure taps at the 2/3 span as compared to the 1/2 span location on Liiva's model (Refs. 56 and 37). It is reasonable to suspect that the spanwise flow induced by the three dimensional flow at the wall could generate pockets of trailing edge stall near the splitter plates (Fig. 24). Thus, the different locations of the pressure orifices in the two tests could make a great deal of difference in the results, i.e., Liiva could measure leading edge stall while Carta measures trailing edge stall characteristics. Dynamically one could expect the trailing edge stall region to travel back and forth along the span as the vortices at the splitter plate-wing junction vary in strength with angle of attack. If one compares Liiva's and Carta's dynamic results, this flow model appears rather attractive. Liiva's results were well predicted by the present technique (Fig. 25); while Carta's results were not (Fig. 26). Furthermore, by using static characteristics that have been shifted, mainly in regard to reattachment angle of attack on the return stroke, the agreement can be improved substantially (Fig. 27). Thus, we see that dynamic stall penetration results are extremely sensitive to the experimental technique.

Even if one is able to produce truly two-dimensional results, their applicability to the full scale finite span case is highly questionable. It is desirable to simulate the full scale end conditions in order to better simulate the details of the lift and moment

NOTES: 1. M = 0.4
2. α = 12.5°
3. P_T = 50 PSI

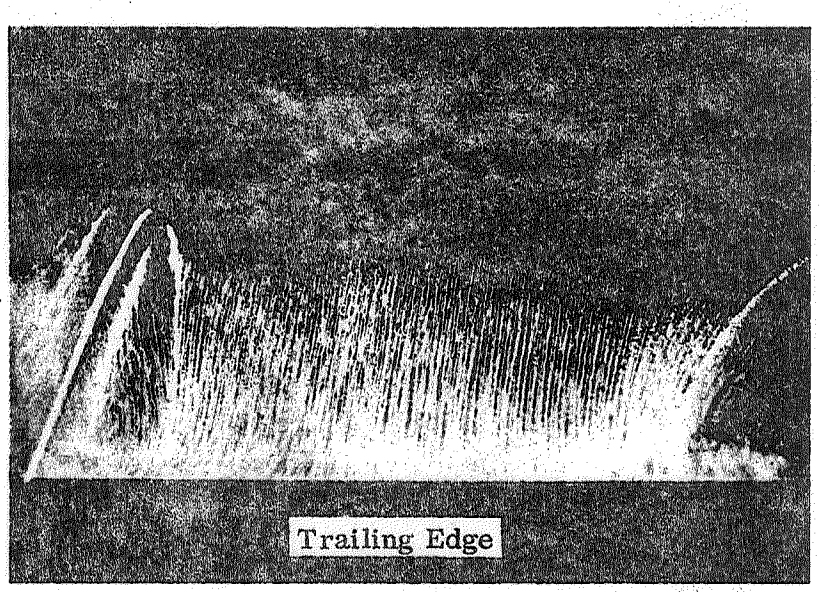

A) NO BLOWING

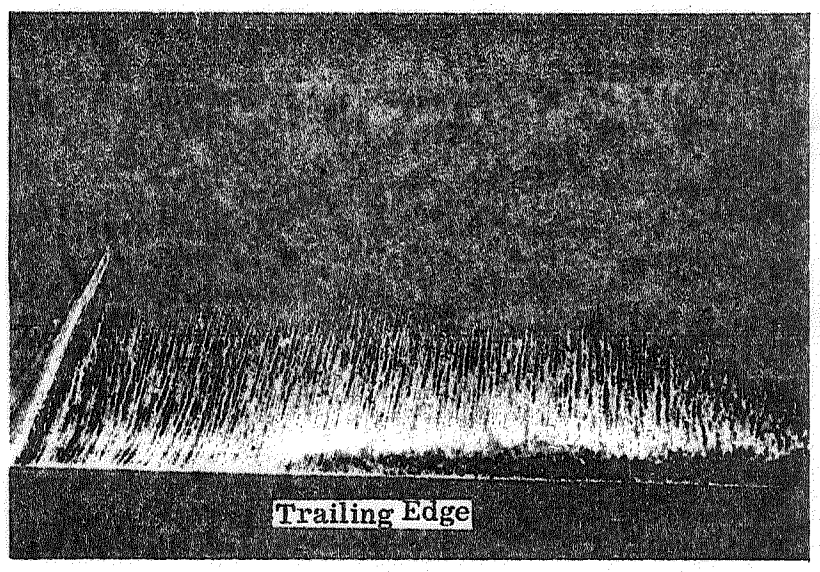

B) BLOWING

Figure 23 Effect of Side Wall Boundary Layer Control on "Two-Dimensional" Airfoil Flow

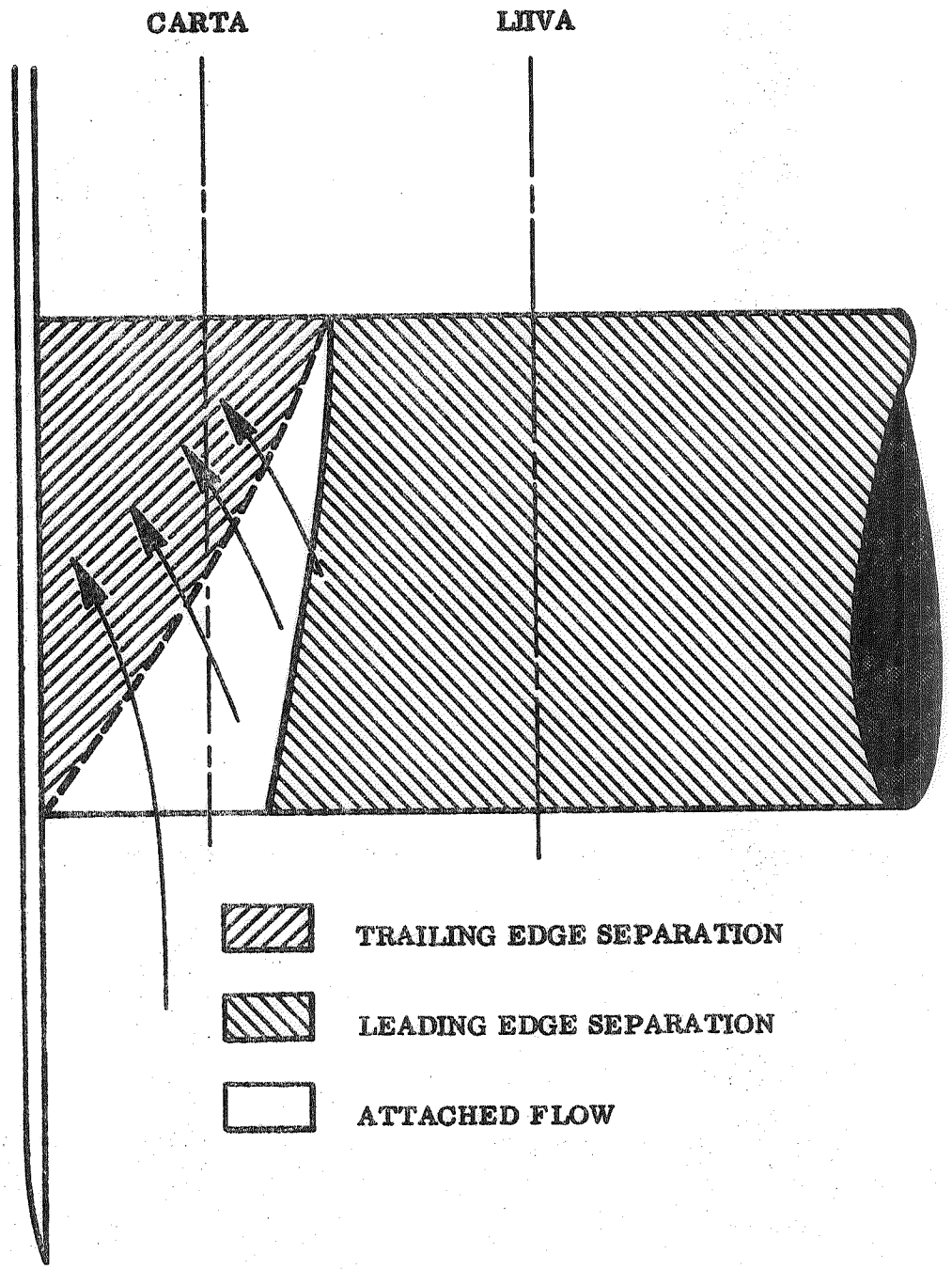

Figure 24 Separated Flow - Wall Boundary Layer Interaction

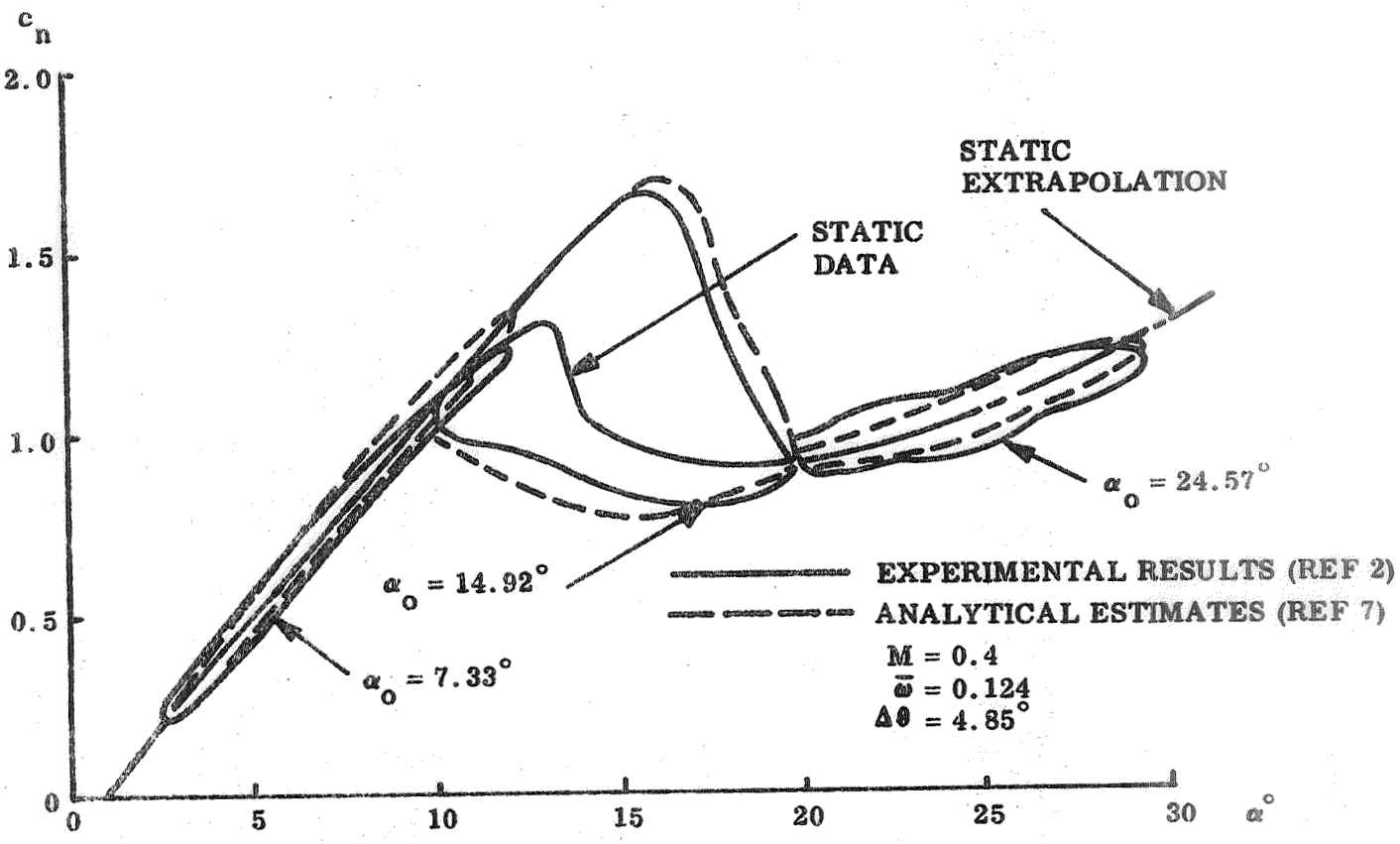

a. NORMAL FORCE

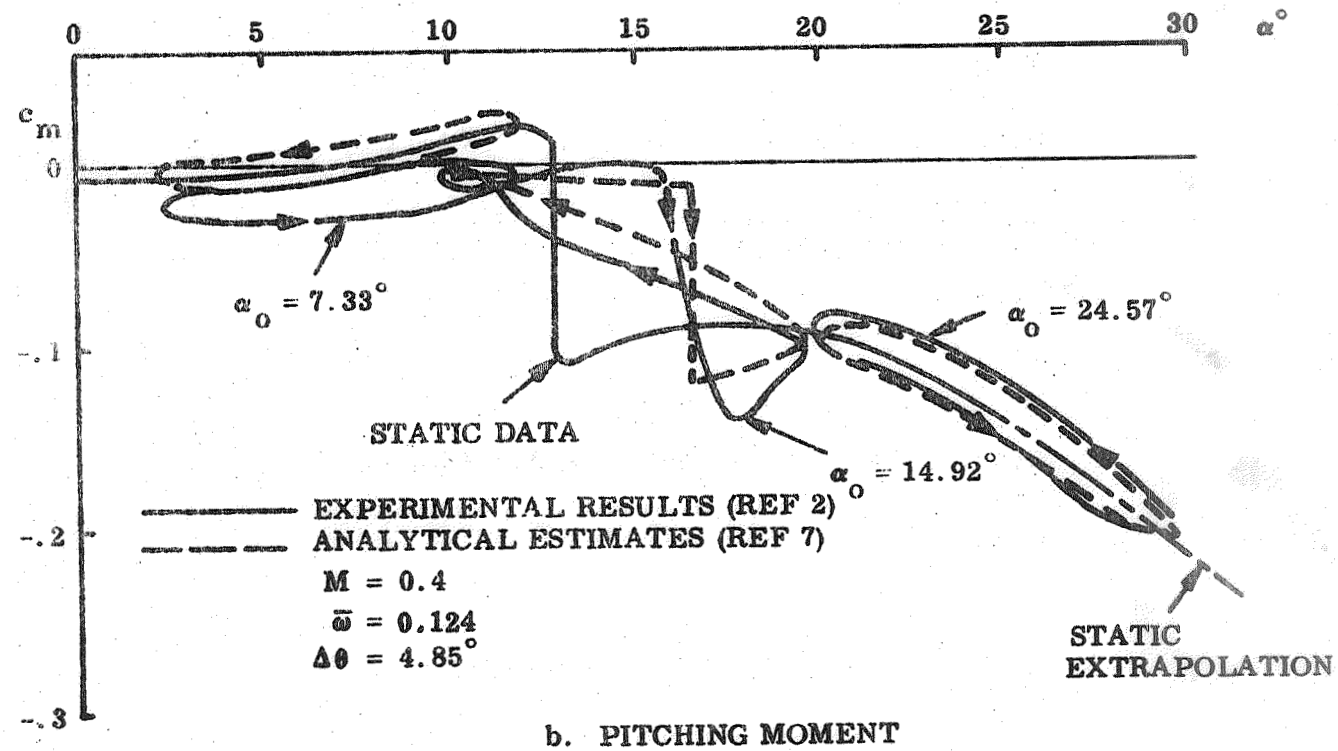

b. PITCHING MOMENT

Figure 25 Effect of Angle of Attack on Dynamic Characteristics (Vertol 23010-1.58 Airfoil Section)

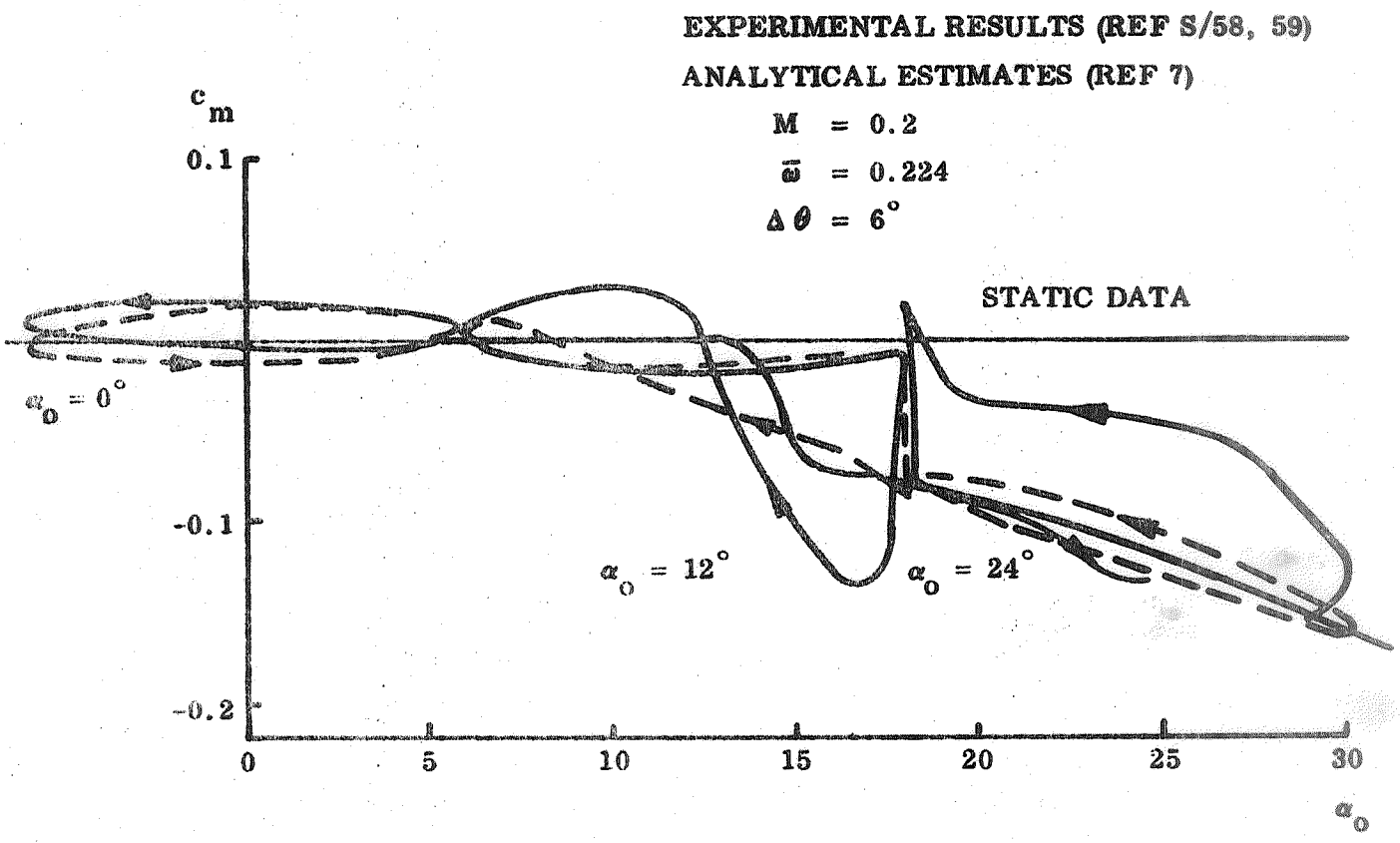

Figure 26 Effect of Angle of Attack on Dynamic Pitching Moment Characteristics (NACA-0012 Airfoil Section)

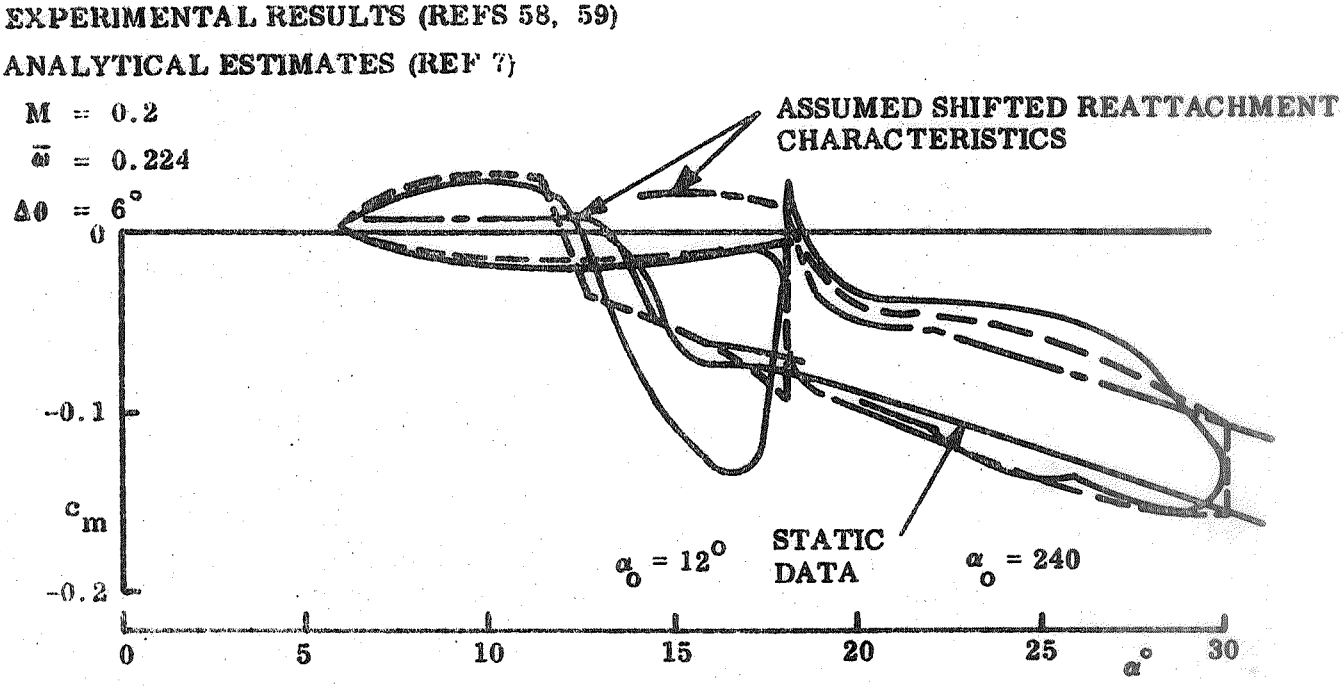

Figure 27 Prediction of NACA-0012 Dynamic Characteristics Using Adjusted Reattachment Characteristics

loops after stall. Thus, the wing aspect ratio and spanwise flow (sweep) must be simulated, making Reynolds number simulation more difficult unless the pitch rate is very high.* In addition to the L. E. sweep correction proposed by Harris et al (Ref. 59) the venting effect of the leading edge vortex has to be included.

Another three dimensional flow effect of importance for dynamic stall and stall flutter is the effect of "aspect ratio" on the von Karman vortex shedding. Theisen has shown that lateral venting of the wake flow is an essential requirement for establishment of the Karman type alternate vortex shedding (Ref. 60). Thus, a two dimensional test with a model of less than critical spanwise extent would not simulate the full scale wake behavior for a helicopter blade or a space shuttle wing.

*For very high pitch rates the lift and moment loop, thus the damping, are determined by the infinite and zero Reynolds number limits, eliminating the need for flight Reynolds number simulation.

Section 3
STALL FLUTTER ANALYSIS

Stall flutter (Refs. 56 and 61) like launch vehicle buffet (Refs. 62 and 63) is the result of separated-flow-induced negative aerodynamic damping, rather than a result of resonance between structural oscillations and dominant harmonics in the aerodynamic forcing functions. The forcing functions are present, and are of importance, but the stall flutter cannot be eliminated by getting off a critical structural frequency. It is present at all frequencies where negative aerodynamic damping exists, and can only be eliminated by increasing the structural damping, e.g., by increasing the structural stiffness and associated natural frequencies, or by decreasing the aerodynamic negative damping until it is less than the positive structural damping. For free oscillations, the latter is accomplished when the oscillation amplitude has increased to the limit cycle value, in which case the structure dissipates energy at the same rate as the surrounding airstream delivers it to the airfoil. In order to determine this limit cycle amplitude, and thereby the seriousness of the stall flutter, one needs to be able to determine the aerodynamic damping as a function of trim angle and oscillation amplitude. Today, 15 years after Rainey's review of the state of the art (Ref. 61), his conclusions can be repeated. "At the present time, no satisfactory stall flutter analysis has been developed." We hope the present work will help towards removing the negation in that statement.

A typical pitching moment loop for an airfoil in the stall region is shown in Figure 25b (Refs. 2 and 6). In the stall penetration region, the sense of the loop is reversed, generating negative aerodynamic damping. The net area enclosed by the loop is a direct measure of the damping. The prediction method developed earlier using graphical means (Refs. 6 and 7) is seen to predict the loop in Figure 25 rather well. It was found, however, that the agreement deteriorated very fast with increasing oscillatory frequency, and that for some combinations of trim angle and amplitude

near stall it never existed even at low frequencies. The latter differences could in some cases have been caused by dynamic simulation problems in the experiments (Ref. 8). However, there remained enough deviations from "good" test data to suggest that something was missing in our description of the dynamic stall and reattachment characteristics.

In the following analysis the old assumptions will be reexamined, and the analytic tools will be improved wherever possible. The three unsteady flow regions composing the stall flutter cycle, i.e., stall penetration, deep stall, and flow reattachment, will be analyzed in detail by themselves before an attempt is made to put all the pieces together to formulate a realistic description of the dynamic stall loop. Finally, the aerodynamic (negative) damping will be computed analytically using only static experimental data as an input.

3.1 STALL PENETRATION

In the previous analysis (Refs. 6 and 7) it was assumed that the dynamic stall overshoot could be represented by an equivalent time lag. The remaining unexplained amplitude dependence was blamed on oscillation induced turbulence that increased the "effective" Reynolds number for the dynamic test (somewhat similar to the turbulence generation that increases the effective Reynolds number in wind tunnels, Ref. 55). Examination of results from systematic measurements of this phase lag (Ref. 64) showed, however, that in addition to the equivalent time lag there would have to be amplitude dependent effects (Fig. 28). The present analysis (Section 2) shows two amplitude dependent effects, Eqs. (21), and (30), which could be significant contributors to the experimentally observed large overshoot of static stall.

The accelerated flow effect of Eq. (21) was envisioned before (Ref. 6). The "decelerating wall" effect, Eq. (30), however, is a new flow phenomenon that opens up interesting possibilities. The effect is directly proportional to the leading edge velocity normal to the oncoming free stream flow. That is, for a pitching airfoil the decelerating wall effect, Eq. (28), would be proportional to the oscillation center ξ_{CG}

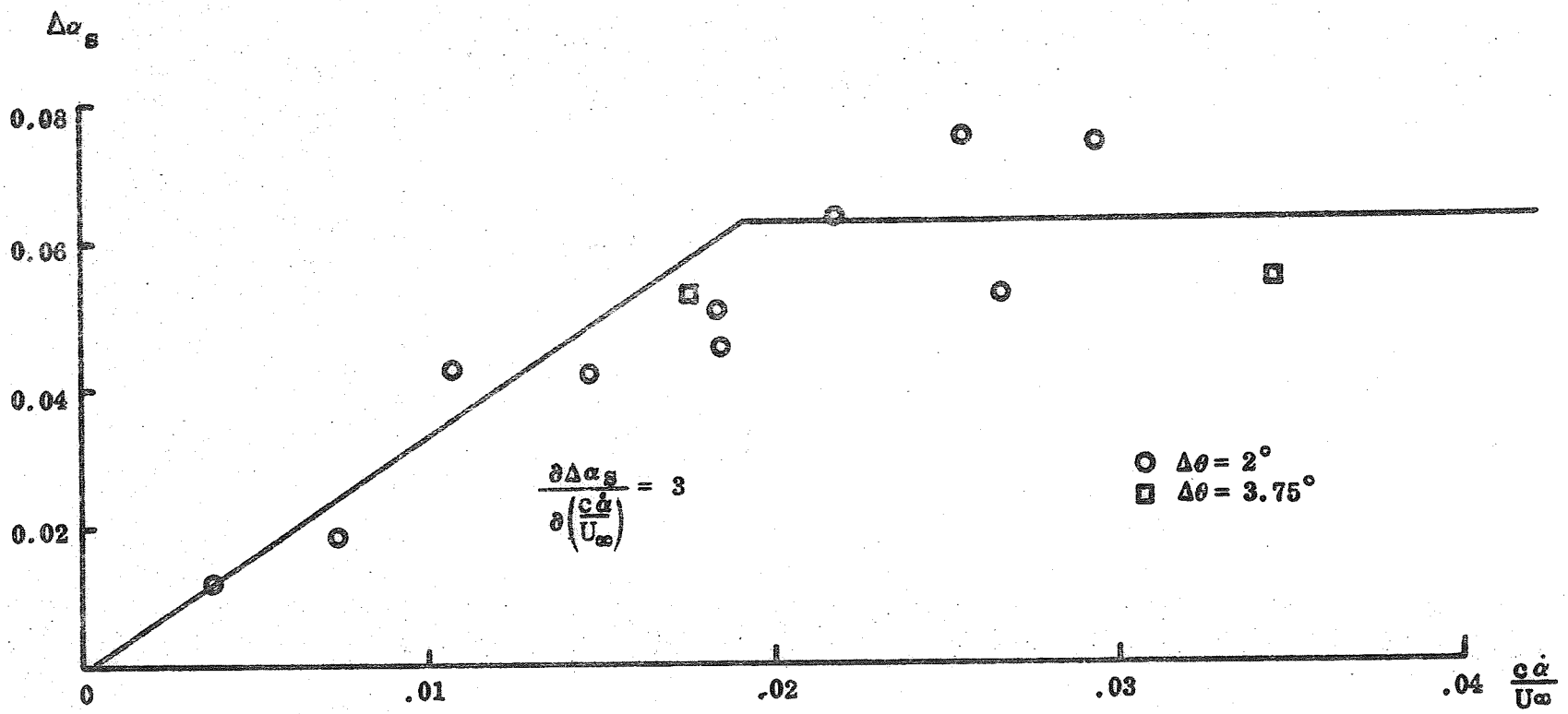

Figure 28 Pitch Rate Induced Delay of Stall on Oscillating Airfoil

whereas the accelerated flow effect, Eq. (21) is insensitive. A measure of the relative importance of the effects can be obtained from a dynamic test in which the oscillation center is varied. Ham has performed such a dynamic test series (Refs. 3 and 65). His ramp data seem to indicate, however, that the dynamic overshoot is, if anything, inversely proportional to the distance from leading edge to oscillation center (Fig. 29). That is, the airfoil oscillating about 75% chord stalls earlier than the one oscillating around 25% chord. The data also indicate that the lift is lagging the motion more for the forward oscillation center than for the aft, which is contrary to basic principles.

From Eqs. (5)-(6) of Reference 7, one obtains (for $\ddot{\alpha} = \ddot{\theta} \approx 0$)

$$\left.\begin{aligned} c_l(t) &= c_l(\alpha_o) + \frac{A}{A_o}\left[c_{l_\alpha}\,\tilde{\alpha}(t-\Delta t) + c_{l_\sigma}\,\sigma(t)\right] + \left(c_{l_{\dot\theta}}\right)_{AM}\frac{c\dot\theta}{U_\infty} \\ \tilde{\alpha} &= \theta + \left(0.5 - \xi_{CG}\right)\frac{c\dot\theta}{U_\infty} \\ \sigma &= \frac{c\dot\theta}{U_\infty} \\ \Delta t &= \xi_w\, c/U_\infty \end{aligned}\right\} \quad (59)$$

The equivalent angle of attack lag for the airfoil in the pitch-up maneuver is

$$\Delta\alpha_{lag} = \left[\xi_w - \left(0.5 - \xi_{CG}\right) - \frac{c_{l_\sigma}}{c_{l_\alpha}} - \frac{\left(c_{l_{\dot\theta}}\right)_{AM}}{c_{l_\alpha}}\right]\frac{c\dot\theta}{U_\infty} \quad (60)$$

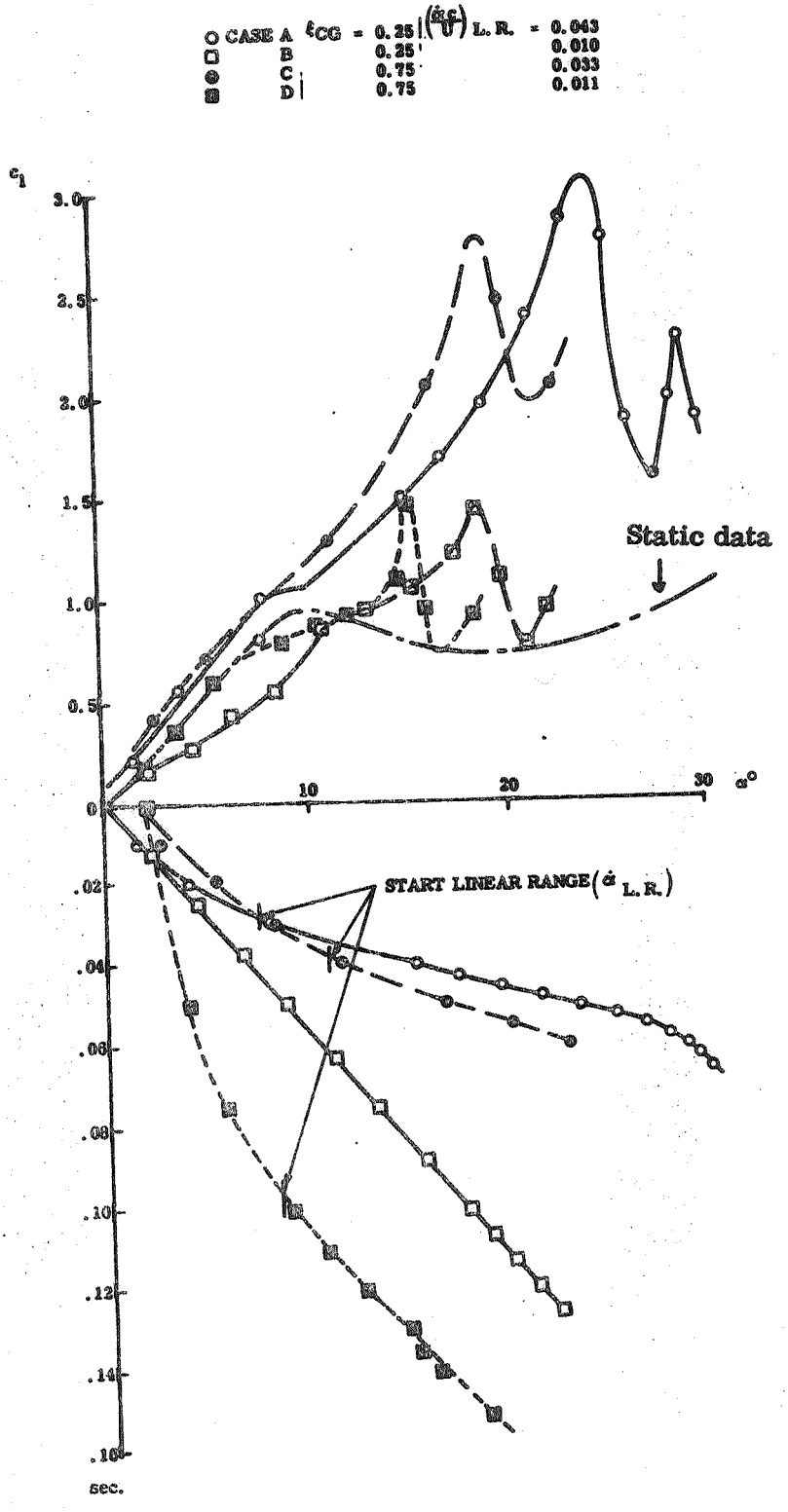

Figure 29 Effect of Ramp-wise Change of Angle of Attack on NACA-0012 Airfoil Stall

Using thin airfoil theory

$$\frac{c_{l_\sigma}}{c_{l_\alpha}} = \frac{\left(c_{l_{\dot\theta}}\right)_{AM}}{c_{l_\alpha}} = \frac{1}{4}$$

Thus

$$\Delta\alpha_{lag} = \left(\xi_w + \xi_{CG} - 1\right)\frac{c\dot\theta}{U} \tag{61}$$

That is, with $\xi_w = 1.5$* (Ref. 7) we obtain for cases A - D in Fig. 29

Case	$\frac{c\dot\alpha}{U_\infty}$	ξ_{CG}	α	$\left(\Delta\alpha_{lag}\right)_{Th.}$	$\left(\Delta\alpha_{lag}\right)_{Meas.}$	$\left(\Delta\alpha_{lag}\right)_{Meas.} - \left(\Delta\alpha_{lag}\right)_{Th.}$
A	.043	.25	> 8°	1.85°	0	-1.85°
B	.010	.25	> 0	0.43°	4°	3.57°
C	.033	.75	>12°	2.35°	-2°	-4.35°
D	.011	.75	> 9°	0.77°	2°	1.23°

As can be seen from the table the substall data in Figure 29 are in complete disagreement with theoretical predictions for attached flow on two accounts: It shows

1. The high angular rate data to lead more than low rate data, when the theoretical predictions are that the data should lag in both cases, the high rate data more than the low rate data.
2. The $\left(\xi_{CG} = 0.75\right)$-data to lead more for high angular rates and lag less for low angular rates than the $\left(\xi_{CG} = 0.25\right)$-data.

*The constant phase lag limit applies only to oscillaroty α-changes.

It has been verified earlier (Ref. 6) that the lag angle measured in airplane pull-up maneuvers (Refs. 28 and 29) is indeed predicted by Eq. (61). Likewise it is well verified that moving the oscillation axis aft increases the phase lag (Refs. 6 and 65). Thus, one has to conclude that something is wrong with the data. In order to know what it might be, one would have to study the test set-up further, as was done for Carta's and Liiva's tests earlier (Section 2.3, Refs. 57 and 37). Such information is not contained in either of References 3 or 65. In any case, the data are inconclusive in regards to determining the relative importance of the decelerating wall effect, Eq. (28).

Ham's data (Refs. 3 and 65) are, however, very valuable in spite of possible dynamic simulation difficulties (Ref. 8). So, for example, do they show not only an overshoot of the static stall, but of the deep stall as well (Figs. 29 and 30). The dynamic boundary layer improvements are apparently large enough to extend the early post stall transient conditions into the deep stall region. Even static data (Ref. 54) indicate that every airfoil has an early post stall region in which the separation point is not fixed but is still moving forward (Fig. 31). It is not difficult to visualize that this transient condition can be extended into the deep stall region to higher angles of attack by the same dynamic effects that caused the large overshoot of static stall in the first place.

Pursuing this transient stall concept a little further, one can also see how an extra oscillatory overshoot of the quasi-steady overshoot could happen, setting up an oscillatory system similar to the one analyzed earlier for the shock-induced separation (Section 2.2). Examining the post stall oscillations observed by Ham (Refs. 3 and 65, and Fig. 29), one finds the same nonlinear behavior; the amplitude decreases with time and the frequency increases. The decrease in amplitude appears to follow the trend of decreasing $\left| \partial c_l / \partial_\alpha \right|$ in Fig. 30, all in perfect agreement with the characteristics for shock-boundary layer interaction analyzed earlier.

It is, of course, not hard to visualize that the dynamic stall, including the oscillatory behavior around a quasi-steady mean, remains similar as the Mach number is gradually increased from $M = 0$ to $M = 0.75$. However, at incompressible speed there can be no coupling between the separation movement and the external forces through a shock motion induced Mach number perturbation, as was the case in Trilling's analysis (Ref. 46) and in our shock-induced separation analysis earlier,

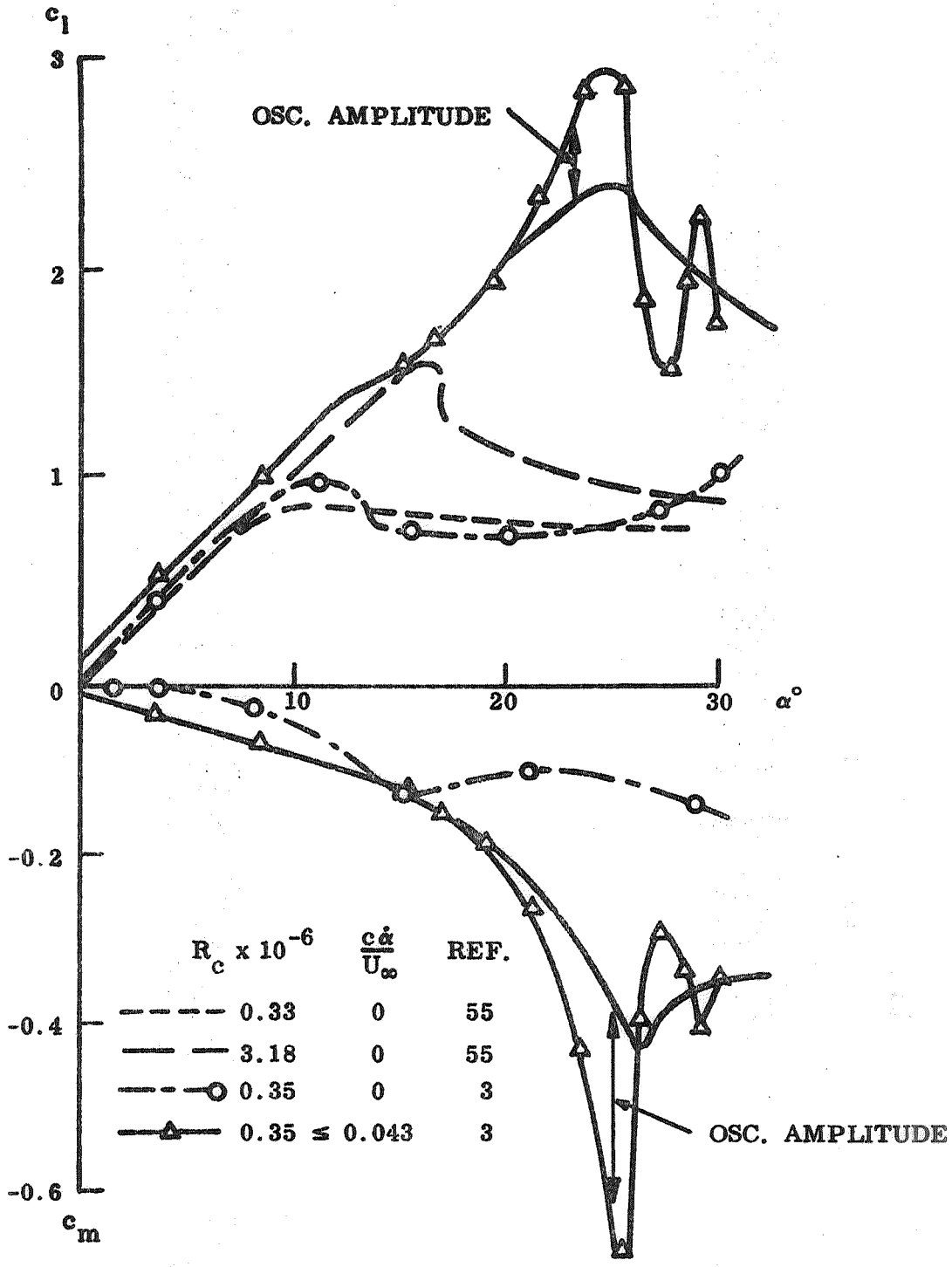

Figure 30 Time Histories of Dynamic Leading Edge Stall

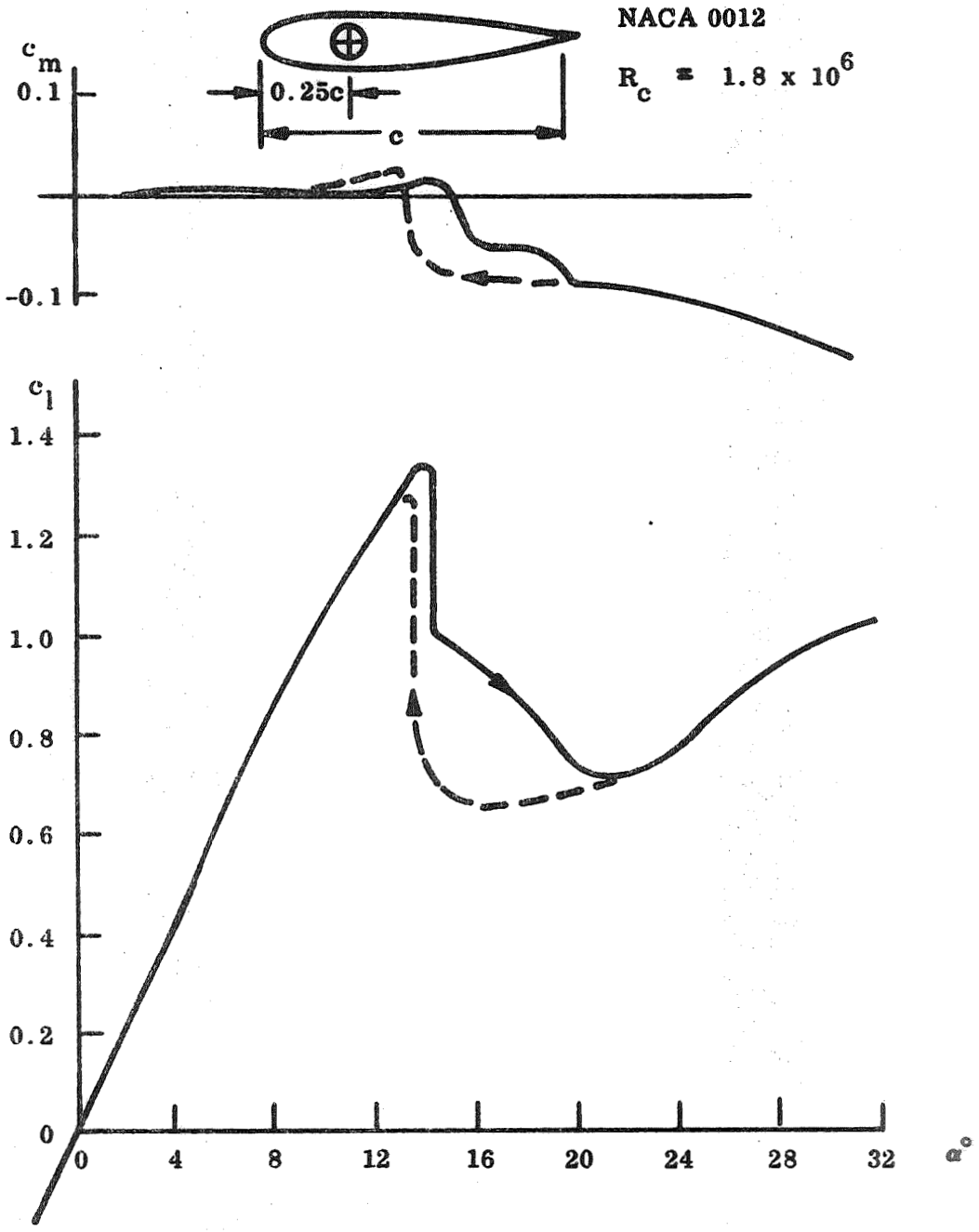

Figure 31 Static Aerodynamic Hysteresis for Leading Edge Stall

Eqs. (33)-(37). We need another mechanism for coupling between separation movement and external flow field. Moore has discussed such a mechanism (Ref. 20). When the separation point moves upstream, the boundary layer, ready to separate, sees a downstream moving wall, and the beneficial effects on the near wall boundary layer delays separation. Whereas it was true that the moving wall effect as caused by the pitching motion itself was small, Eq. (26), this is no longer true when the apparent wall movement is caused by a fast moving separation point (Fig. 32). The apparent wall velocity U_{w_s} is

$$\frac{U_{w_s}}{U_\infty} = \frac{d\xi_s}{d\alpha}\,\frac{c\dot{\alpha}}{U_\infty} \tag{62}$$

Whereas the proportionality constant was of magnitude 0.1 in Eq. (26), it is two orders of magnitude larger in Eq. (62). Using the separation point movement for the compressible case, Fig. 18a in Section 2.2, we would get

$$\frac{d\xi_s}{d\alpha} \approx -4$$

There is no reason to believe that the sudden separation movement for imcompressible high angle of attack stall would be slower in comparison to the shock-induced separation in compressible stall. Thus, the velocity ratio in Eq. (62) reaches magnitudes of 0.1 or 0.2 for Ham's fast α-ramp, $c\dot{\alpha}/U_\infty = 0.04$ (Figs. 29 and 30). It has been shown that substantial delay of separation is possible for those types of velocity ratios (Refs. 21 and 22).

The separation point will lag its static position due to this moving wall effect by

$$\Delta\xi_s\left(\frac{U_{w_s}}{U_\infty}\right) = \frac{\partial\xi_s}{\partial\left(\frac{U_{w_s}}{U_\infty}\right)}\,\frac{U_{w_s}}{U_\infty} \tag{63}$$

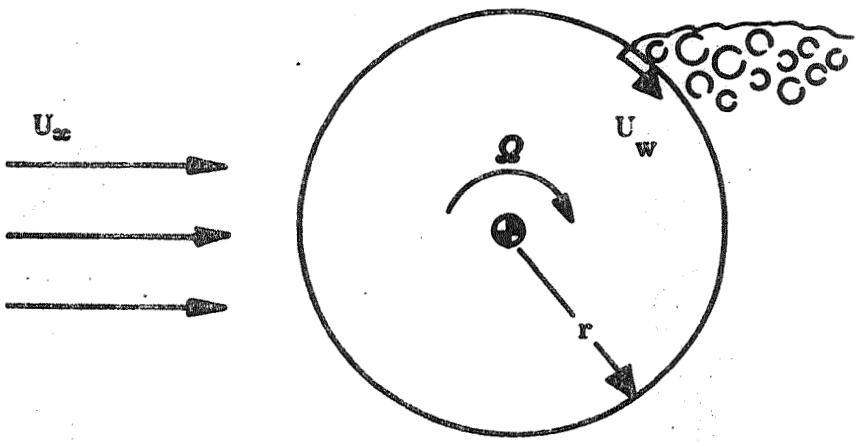

a. Rotating Cylinder

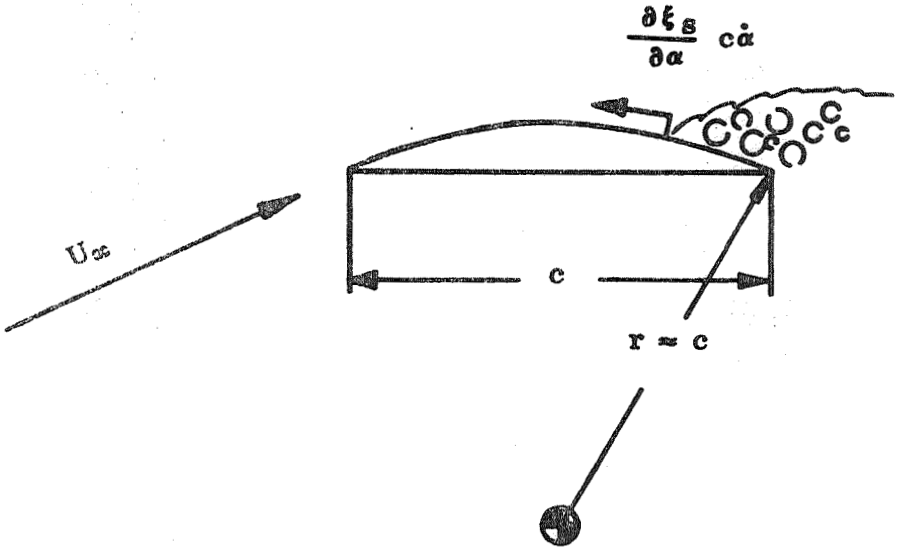

b. Circular Arc Airfoil

Figure 32 Moving Wall - Moving Separation Point Analogy

The corresponding overshoot of angle of attack is

$$\Delta\alpha\left(\frac{U_{w_s}}{U_\infty}\right) = \Delta\xi_s\left(\frac{U_{w_s}}{U_\infty}\right)\Big/\frac{\partial\xi_s}{\partial\alpha} = \xi_{a_s}\,\frac{c\dot{\alpha}}{U_\infty} \tag{64}$$

Eqs. (62)-(64) define the equivalent time lag ξ_{a_s} as follows

$$\xi_{a_s} = \frac{\partial\xi_s}{\partial\left(\frac{U_{w_s}}{U_\infty}\right)} \tag{65}$$

Using the rotating cylinder data obtained by Brady and Ludwig (Ref. 21), a circular arc airfoil (Fig. 32) would have

$$\partial\xi_s\Big/\partial\left(\frac{U_{w_s}}{U_\infty}\right) \approx \begin{cases} 0.7\ ; \text{ Supercritical Reynolds numbers} \\ 3.0\ ; \text{ Subcritical Reynolds numbers} \end{cases} \tag{66}$$

The supercritical case is somewhat representative of the turbulent trailing edge separation. This lag ξ_{a_s}, due to separation movement, exists also in the compressible case, i.e., ξ_{a_s} should be added to $\xi_{a_{sh}}$ and ξ_w in Eq. (39). The value of $\xi_{a_s} = 0.7$ gives an additional angle of attack lag $\Delta\alpha_s = 0.24°$ which should be added to the quasi-steady lag used in Fig. 18. That is, the effect is small and can be neglected in regards to the discussion of the shock-oscillation in Fig. 18.

The subcritical case is more representative of the laminar separation bubble and associated leading edge separation. For leading edge type stall, this delay ξ_{a_s} would only affect the post stall behavior, i.e., the gradual loss of lift after the stepwise change due to bubble burst (Fig. 31). However, for high pitch-up rates the leading edge bubble may be eliminated due to dynamic effects, such as the decelerating wall effect, Eq. (28). Data obtained by Ham (Refs. 3 and 65) and others (Refs. 31 and

32) indicate that this is happening (Fig. 33). The static leading edge stall is converted to a dynamic trailing edge stall overshooting the infinite Reynolds number limit for LE-stall. The analogy between the "decelerating wall effect" and the wall-jet effect measured by Wallis (Refs. 17 and 38, Fig. 11) makes this dynamic stall change seem very probable. In this case the delay ξ_{a_s} will affect all the separation induced aerodynamic forces during stall, as there is no stepwise change due to bubble burst which it has no effect upon.

The "dual sheet" Karman vortex shedding (Ref. 67) supplies another explanation for the post stall oscillations (Fig. 34a). The shedding frequency $\left(\bar{\omega}_w\right)$ in response to airfoil oscillations $\left(\bar{\omega}_o\right)$ is

$$\bar{\omega}_w = \left(\frac{1 + \left(\xi_s\right)^{1/2}}{2}\right)^2 \bar{\omega}_o \quad . \tag{67}$$

The initial overshoot of the separation starting the oscillations in Fig. 30 is caused by the airfoil motion. If one assumes that Eq. (67) would apply to the ensuing oscillation of the separation point, the wake oscillation from the stalled airfoil $\left(\xi_s = 0\right)$ would have the following frequency

$$\bar{\omega}_w = \frac{\bar{\omega}_o}{4} = \frac{\pi}{2} S_o / \sin \alpha_s \tag{68}$$

$2\pi S_o / \sin \alpha_s$ is the cylinder shedding frequency. With $S_o \approx 0.2$ and $\sin \alpha_s \approx 0.2$, $\bar{\omega}_w$ is

$$\bar{\omega}_w \approx \frac{\pi}{2} \approx 1.6 \tag{69}$$

If one instead considers the Karman vortex shedding frequency set by the distance between separation point, $\xi_s = 0$, and the trailing edge (Fig. 34b), one gets exactly half the regular cylinder shedding frequency,

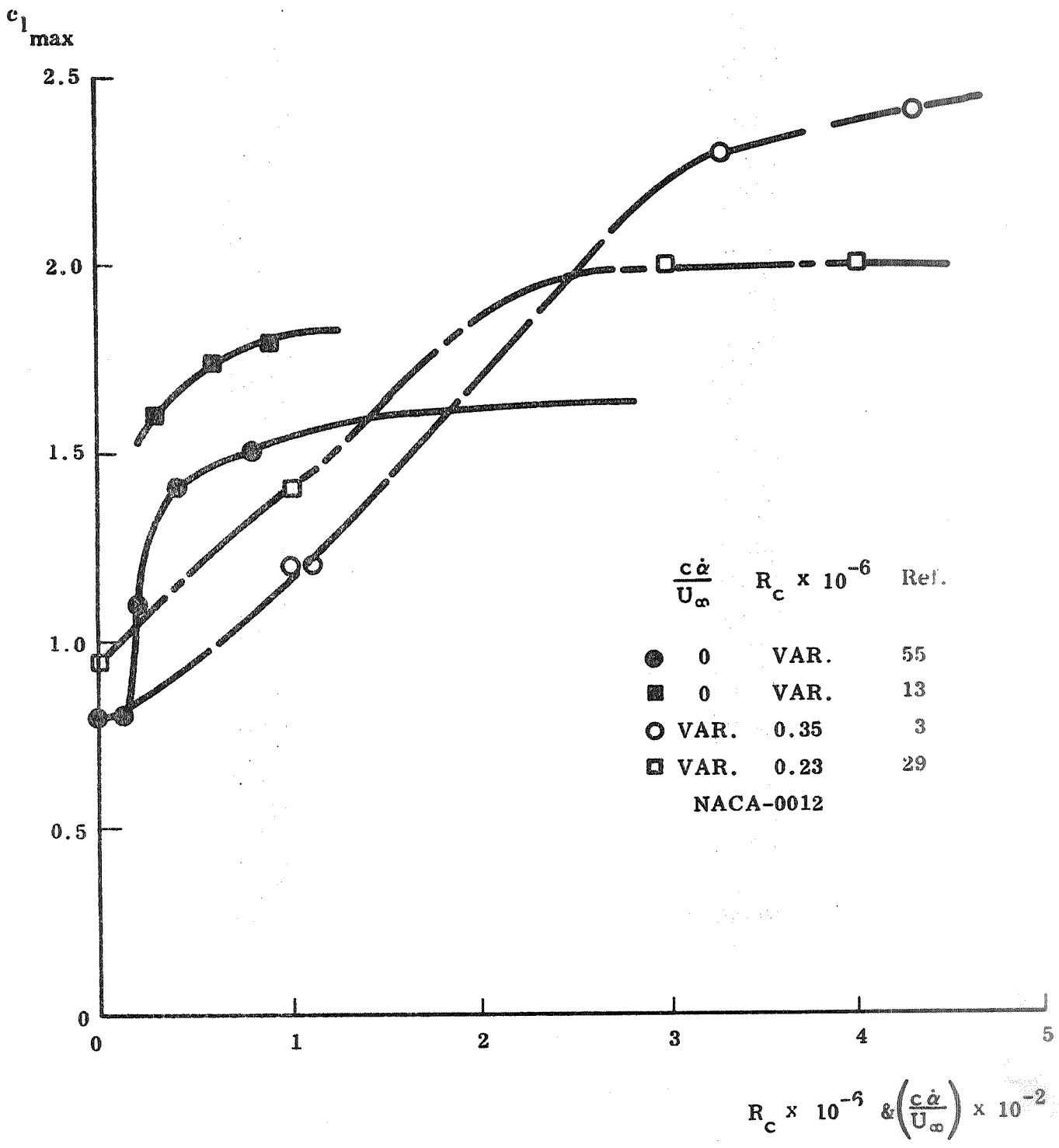

Figure 33 Pitch Rate Induced Change of Stall Type

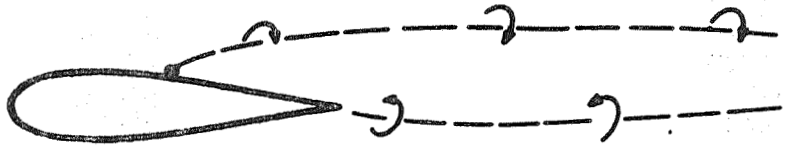

a. Forced Oscillations

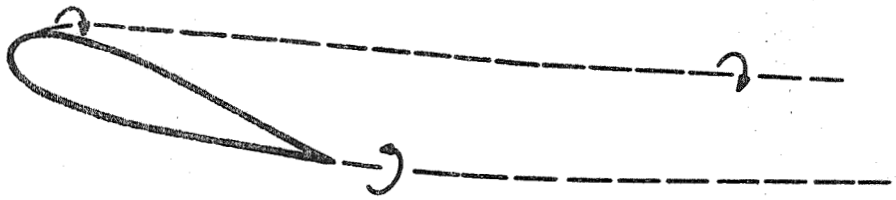

b. Oscillating Separation Point

Figure 34 Airfoil Wake Shedding

$$\bar{\omega}_w = \frac{\bar{\omega}_o}{2} \tag{70}$$

Thus, one could expect the stalled airfoil vortex shedding frequency to be in the following range

$$1.6 < \bar{\omega}_w < 3.2 \tag{71}$$

The frequencies of the first three half cycles for case A in Fig. 24 increase from $\bar{\omega} = 2$ to $\bar{\omega} = 3$.

With the separation point free, rather than fixed, there is a mechanism for initial overshoot and associated motion dependence of the frequency and amplitude of the wake oscillation. It has been shown by Parkinson (Ref. 68) that the Karman vortex shedding off circular cylinders can be amplitude modulated, and also be driven off the Karman vortex shedding frequency (up to 40%) by oscillating the cylinder normal to the oncoming flow. That is, even on a cylinder the separation point (= vortex shedding point) is coupled to the body motion. The same delay of separation due to separation point movement exists on the cylinder, as on the airfoil discussed above. It has been demonstrated that oscillating an airfoil near its dual vortex sheet shedding frequency produces the same result observed by Parkinson on the cylinder (Ref. 69). When the airfoil (natural) oscillation frequency is close to this wake frequency, $\bar{\omega}_w$, strong coupling effects can, of course, be expected.

3.2 DEEP STALL CHARACTERISTICS

In our previous analysis (Refs. 6 and 7) the deep stall was assumed to be similar to the attached flow case, the only difference being that the aerodynamic derivatives would have different magnitude. Using negative camber effects suggested by Clark-Y airfoil data (Ref. 70) gave rather good prediction of the deep stall dynamic loops. However, it was found later that more appropriate static experimental camber data gave a substantial underprediction of the size of the deep stall loops for several of the airfoils tested.

The present analysis indicates that the dynamic boundary layer improvement effects, Eqs. (21) and (30), should also work in the early post stall region, as indicated by Ham's ramp data (Figs. 29 and 30). Furthermore, the airfoil oscillation can build up this boundary layer attachment effect without the amplitude being large enough to "reach down" to the static characteristic (Ref. 56 and Fig. 35). The leading-edge wall-jet and other dynamic effects discussed here supply a much more satisfactory explanation for this phenomenon than the oscillation induced turbulence suggested earlier for lack of anything better (Ref. 6). Thus, one would expect, in view of these new flow mechanisms, that the deep stall value of a ramp would be the same regardless of whether or not the static stall angle was ever penetrated.

3.3 REATTACHMENT CHARACTERISTICS

As the dynamic boundary layer improvement effects are completely reversible, one would expect that a pitch down movement back from the deep stall region (Figs. 29 and 30) would produce an undershoot of static reattachment of the same magnitudes as the overshoot of static stall (provided static α-hysteresis is not present). That is, Eqs. (21), (25), and (30) would be valid also for the undershoot angles of static reattachment. As there is a limit for overshoot of stall, the infinite Reynolds number limit discussed earlier, there is a limit for the undershoot of reattachment. That limit is, of course, the zero Reynolds number limit, as long as the dynamically induced apparent shape changes are not large enough to change the effective airfoil shape (which usually is true, see section 2).

3.4 DYNAMIC LOOP CONSTRUCTION

In the previous analysis (Ref. 6) it was assumed that the upstroke characteristics for the oscillating airfoil were those for infinite Reynolds number, and that the back stroke characteristics were those for zero Reynolds number. The former is the case only for high test Reynolds number and high oscillatory rate, the latter only if the test Reynolds number is low and/or the oscillatory rate is high. As the oscillations analyzed all were of large amplitudes, $\left|c\dot{\alpha}/U_\infty\right|$ was rather large. This is the reason for

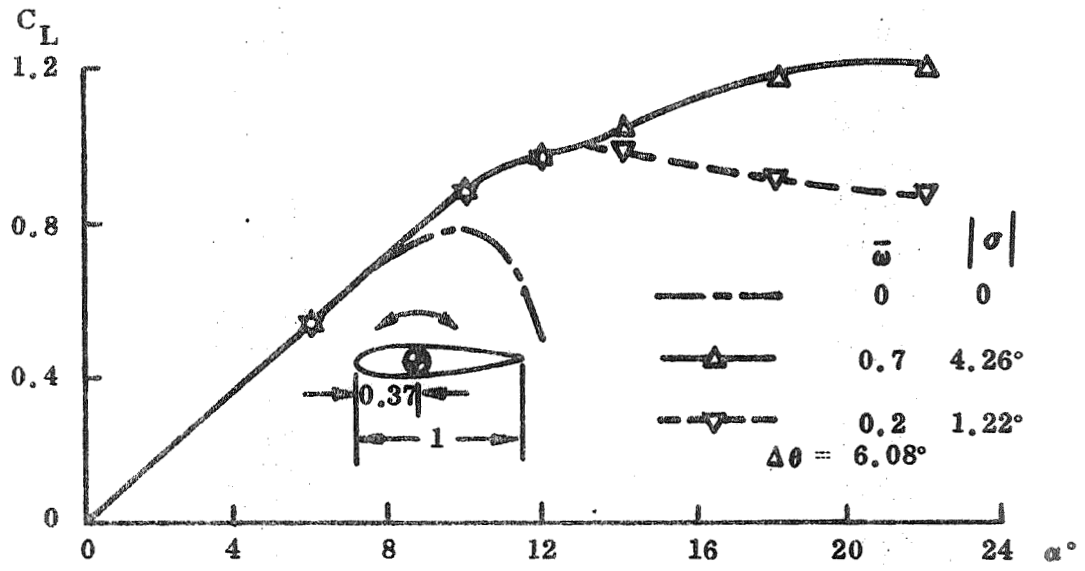

Figure 35 Time Average $C_L(\alpha)$-Curves for Thin Wing at $R_c = 10^6$ (Ref. 56)

the good predictions obtained using upstroke and down-stroke characteristics unmodulated for amplitude effects, only time shifted with the extra time lag effect $\xi_a = 2.0$.

In the present analysis both upstroke and down-stroke characteristics are modulated by the angular rate, $c\dot{\alpha}/U_\infty$. The stall induced forces are associated with the extra time lag ξ_{a_s}, given by Eqs. (65) and (66). In the compressible case the shock motion induces an additional time lag $\xi_{a_{sh}}$, Eq. (37).

When the airfoil describes oscillations in pitch, it operates between the limits given by the up- and down-stroke ramps shown in Fig. 36. The dynamic ramp data have been phase shifted back to agree with static data, i.e., they are shown versus the phase shifted angle of attack.

$$\alpha^i = \alpha_o + \theta(t - \Delta t) = \alpha_o + \Delta\theta \sin\left(\omega t - \phi - \phi_s\right)$$

$$\phi = \begin{cases} 1.5\,\omega\,; \bar{\omega} \leq 0.16 \\ 0.245\,; \bar{\omega} > 0.16 \end{cases}$$

$$\phi_s = \begin{cases} 0 & ; \ \alpha^i \leq \alpha_s \\ \left(\xi_{a_s} + \xi_{a_{sh}}\right)\bar{\omega} & ; \ \alpha^i > \alpha_s \end{cases} \tag{72}$$

When the pitch-up rate is constant, as in the case of a ramp, the stall overshoot $\Delta\alpha_s$ is determined by the constant pitch rate, $c\dot{\alpha}/U_\infty$, Eq. (31) and Fig. 37. The limit $\Delta\alpha_{s_{max}}$ corresponds to the infinite Reynolds number limit, i.e.,

$$\alpha_s + \Delta\alpha_{s_{max}} = \left(\alpha_s\right)_{Re \to \infty} \tag{73}$$

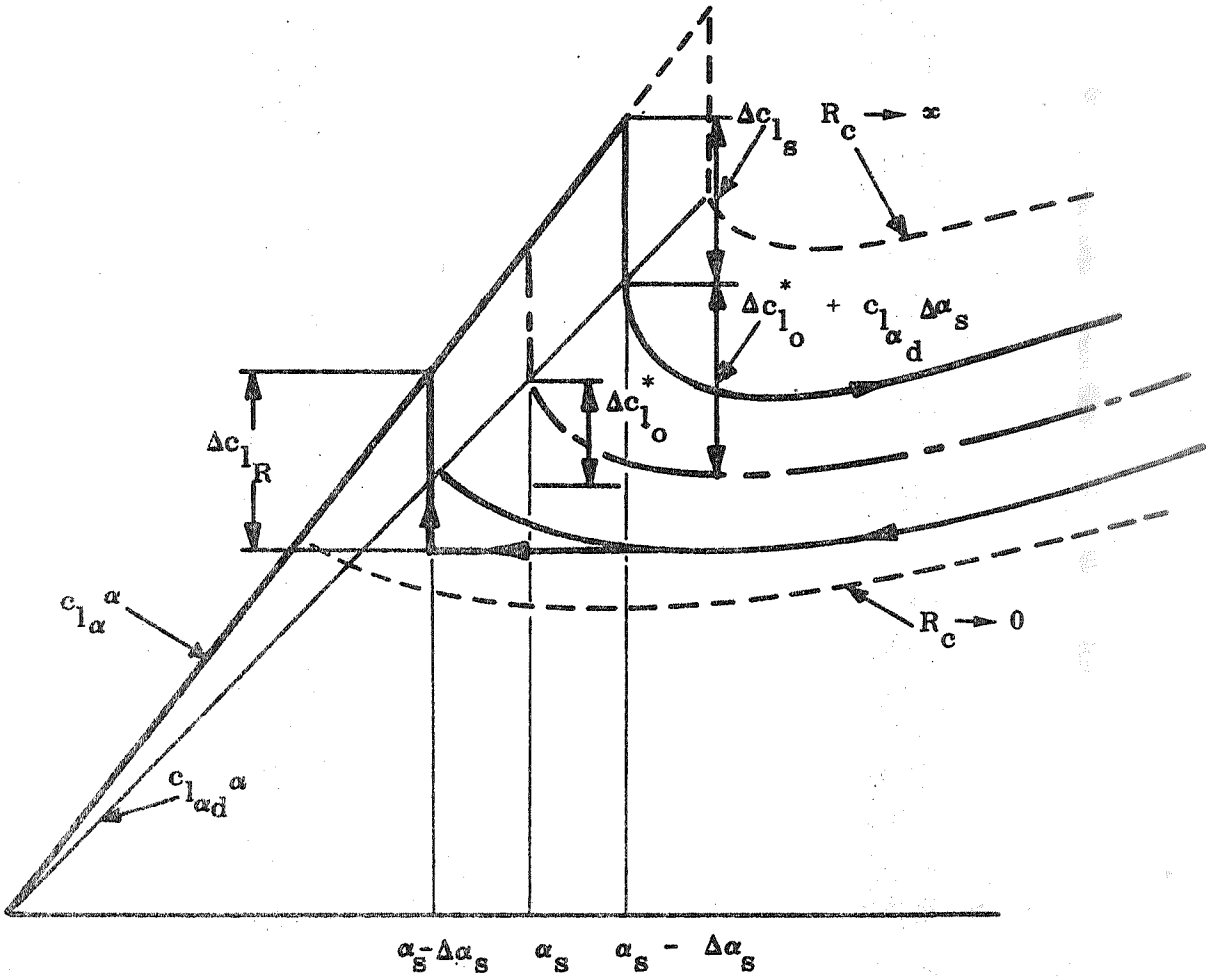

Figure 36 Dynamic Stall Penetration

For lower rates than $\left(\frac{c\dot{\alpha}}{U_\infty}\right)_{crit}$, the rate giving $\Delta\alpha_{s_{max}}$ (Fig. 37), the stall overshoot will be less than the maximum possible. Such a case is illustrated in Fig. 36. Based upon Ham's ramp data (Refs. 3 and 65), and the transient post stall concept discussed earlier, Section 3.1, it is expected that the early post stall improvement due to dynamic boundary layer effects will last throughout the deep stall until tapering off to zero at high α where flat plate stall dominates.

As the dynamic boundary layer effects are completely reversible, the return or pitch-down ramp with the same constant angular rate would be completely symmetrical, as sketched in Figure 36, provided that the boundary layer separation at α_s reacts in a linear manner to these dynamic flow effects. This should be a rather good assumption as long as static α-hysteresis effects are not present. When the back-stroke angular rate is high enough, the zero Reynolds number limit is approached.

$$\alpha_s - \Delta\alpha_{R_{max}} = (\alpha_s)_{Re\to 0} \tag{74}$$

When static hysteresis is present, as it often is (Ref. 54), it will introduce a "pure play" effect (Fig. 37). That is, the stall overshoot for rates below $\left(\frac{c\dot{\alpha}}{U_\infty}\right)_{crit}$ is not a linear function of angular rate, but is rather a random event. Consequently, the overshoot $\Delta\alpha_s \leq \Delta\alpha_{s_H}$ is independent of rate, and is determined by such things as daily wind tunnel turbulence variations, etc. Model vibrations, via its support, will reduce this hysteresis effect, as will an increase of Reynolds number (see Fig. 37). That is, when the wind tunnel test Reynolds number is low one can expect the hysteresis effect to be large. Of course, the margin of overshoot until α_{s_∞} is reached has also increased. It is probable that the ratio $\Delta\alpha_{s_H}/\Delta\alpha_{s_{max}}$ remains fairly constant, as is sketched in Fig. 37. When the rate is higher than $\left(c\dot{\alpha}/U_\infty\right)_{crit}$, the linear relationship exists again, and the presence of static hysteresis effects are never noticed in the dynamic overshoot.

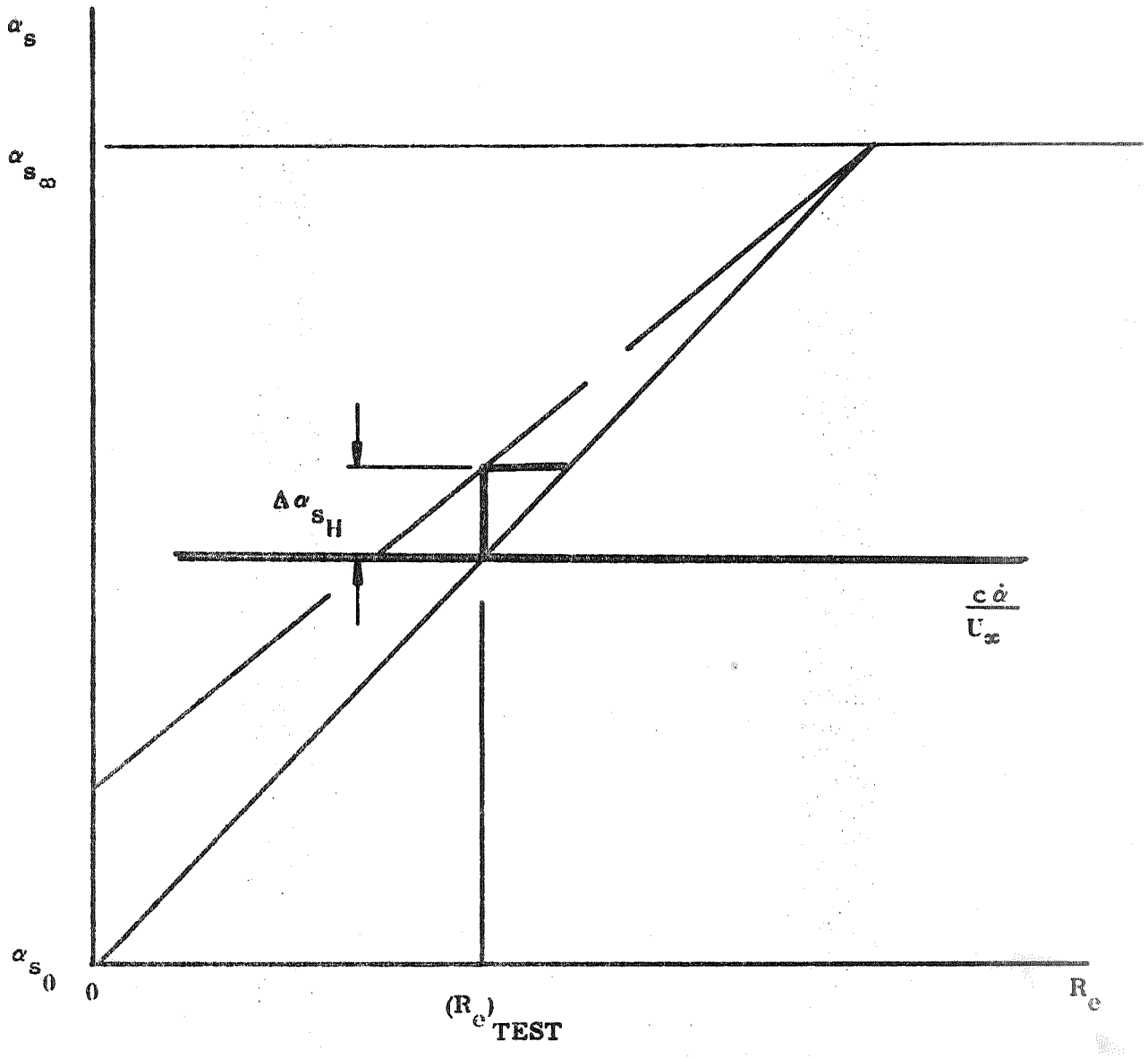

Figure 37 Dynamic Overshoot and Undershoot of Static Stall and Reattachment as a Function of Pitch Rate and Reynolds Number

The reattachment is, in contrast, a rather steady event. No random variations of noticeable magnitudes were ever observed in the transonic flow separations existing on blunt bodies of revolution, although the separation angle of attack could vary several degrees between repeat runs (Ref. 71). That is, for angular rates above the critical value $\left(c\dot{\alpha}/U_\infty\right)_{crit}$, the up- and down-strokes are essentially antisymmetric events. The only exception is the near reattachment conditions. As the dynamic effects that extended the transient conditions into deep stall, by delaying the separation movement to its most forward point, are reversed on the downstroke, fixing the separation at its most forward location, the reattachment jump will occur all the way from the full stall condition (Fig. 36).

When the angular upstroke rate is higher than $\left(c\dot{\alpha}/U_\infty\right)_{crit}$ or the downstroke rate is beyond $\left(c\dot{\alpha}/U_\infty\right)_0$ (Fig. 37), the infinite and zero Reynolds number limits cut off any further over- and under-shoot of the static characteristics. That is, the upstroke and downstroke occur along the characteristics marked $R_e \to \infty$ and $R_e \to 0$ in Fig. 36. This is true as long as a change of stall type does not occur.

When an airfoil is oscillating around a trim angle α_o that is close to the static stall angle α_s, it should experience this "ceiling and floor" for its $c_{l_{max}}$ and $c_{l_{min}}$, provided the oscillation amplitude is of sufficient magnitude. The systematic measurements by Liiva (Ref. 37) do indicate this effect (Fig. 38). That is, as the frequency is increased, increasing $\left|c\dot{\alpha}/U_\infty\right| = \Delta\theta\bar{\omega}$, the maximum and minimum lift values recorded in the dynamic loops approach the infinite and zero Reynolds number limits (Fig. 38a).* Accordingly one can assume the static stall angle limits to be approached in a similar way (Fig. 38b). When constructing the pitch moment loops

*The undershoot of the zero Reynolds number limit is not understood. It could possibly be a result of wind tunnel and support interference (see earlier dis-dussion in Section 2.3).

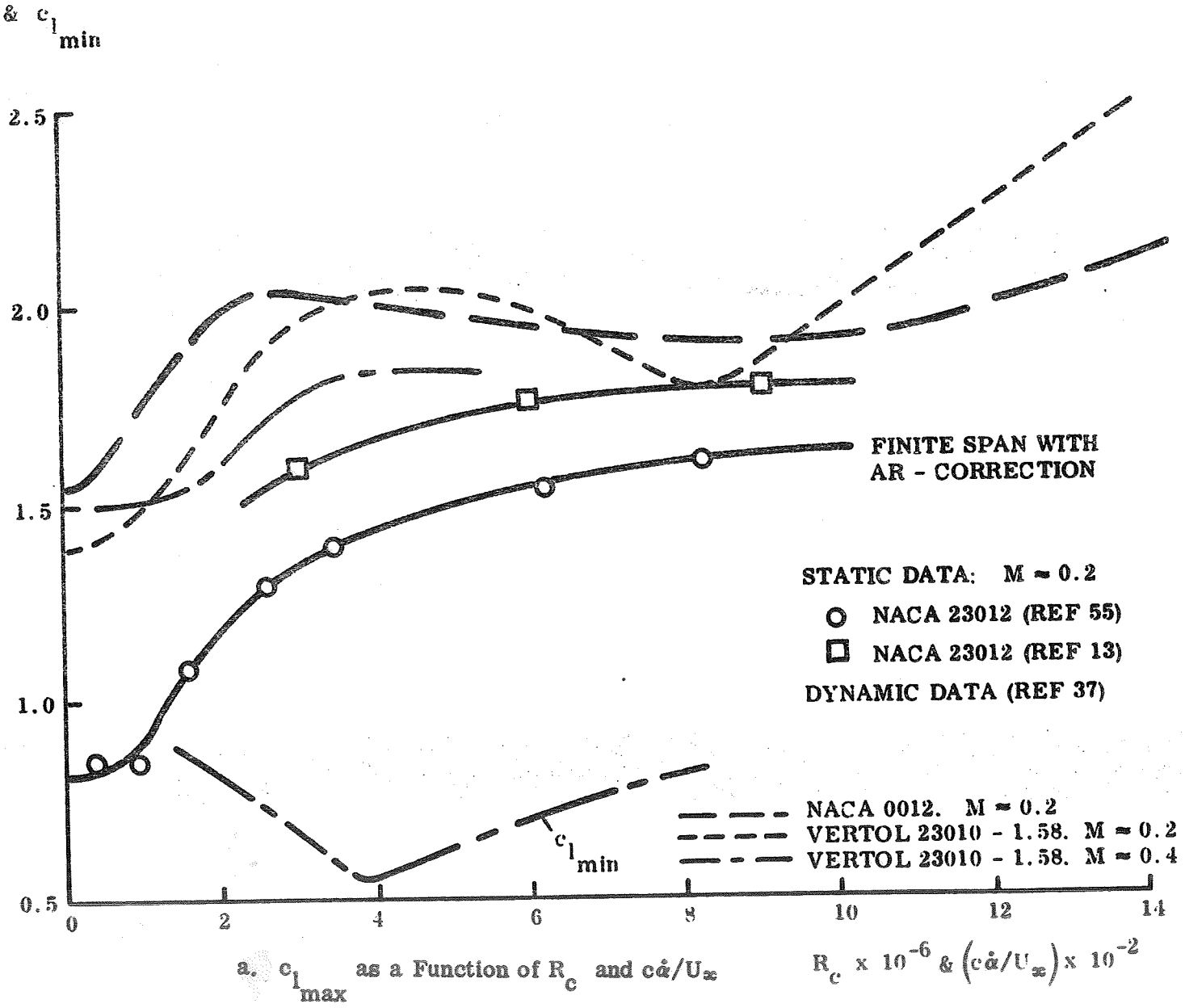

Figure 38 Experimentally Observed Dynamic Overshoot and Undershoot of Static Stall Compared to Infinite and Zero Reynolds Number Limits

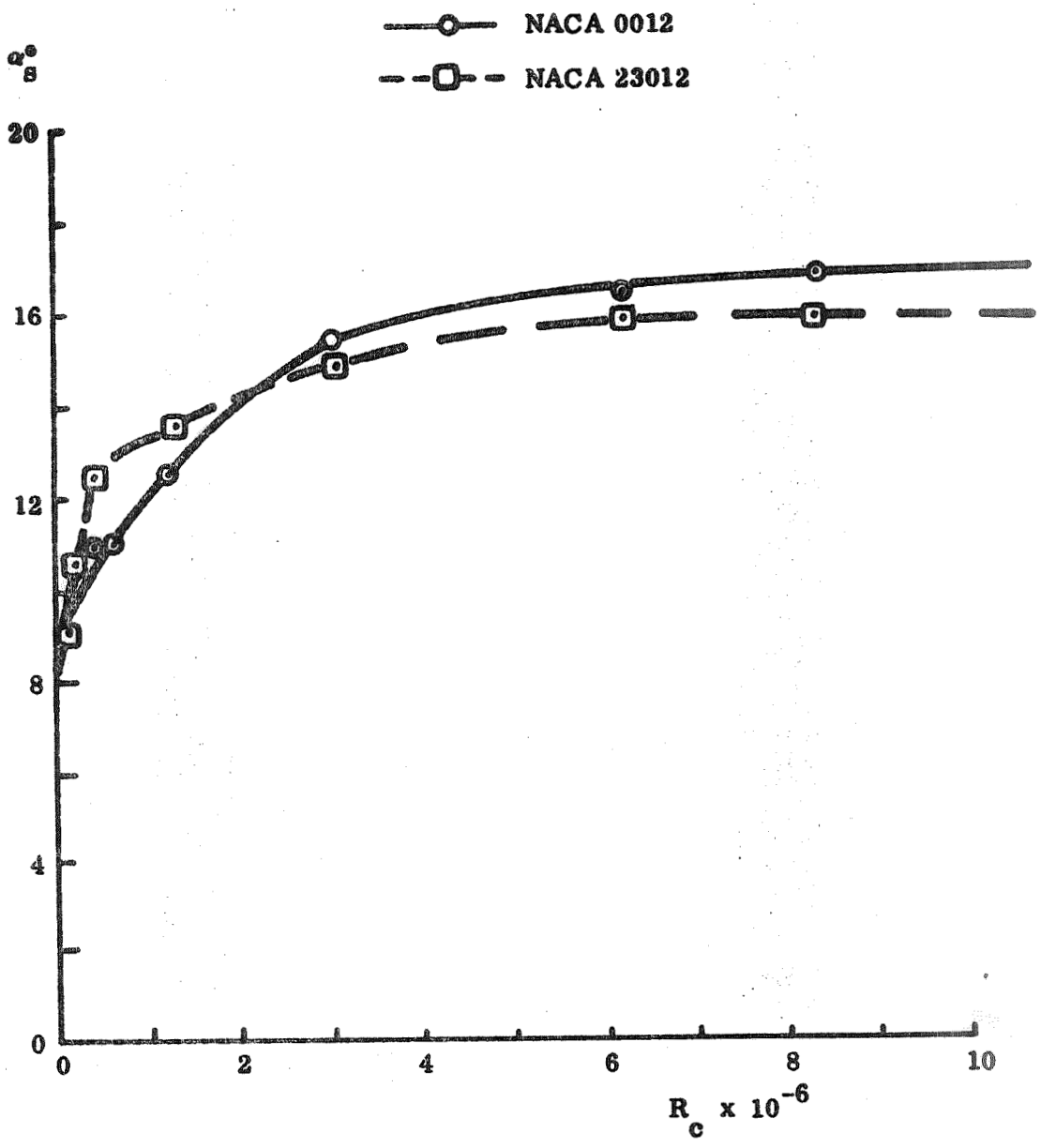

b. Static Stall Angle (α_s) as a Function of R_c

Figure 38 Experimentally Observed Dynamic Overshoot and Undershoot of Static Stall Compared to Infinite and Zero Reynolds Number Limits

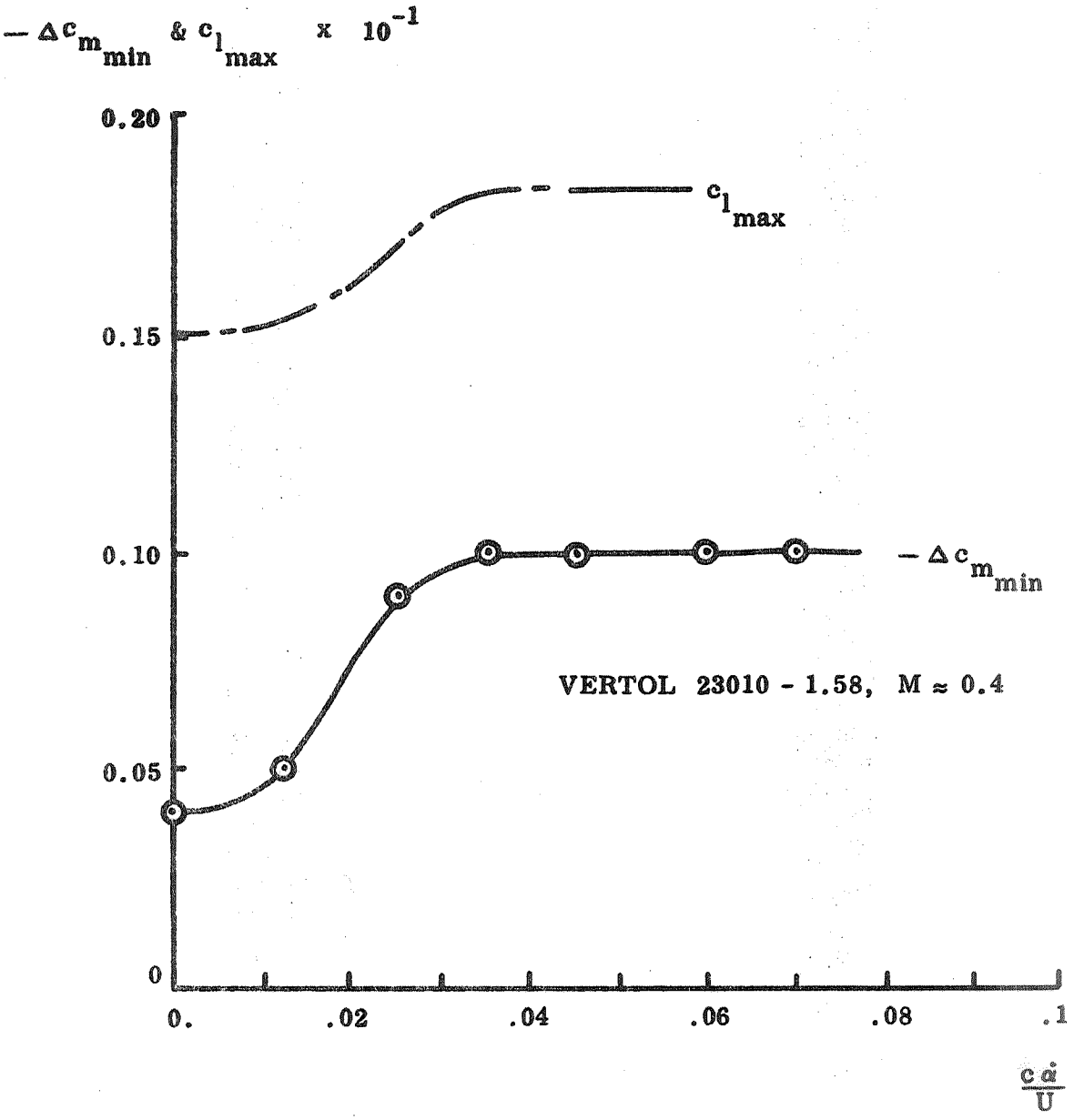

c. $c_{l_{max}}$ and $-\Delta c_{m_{min}}$ as a function of $c\dot{\alpha}/U_\infty$

Figure 38 Experimentally Observed Dynamic Overshoot and Undershoot of Static Stall Compared to Infinite and Zero Reynolds Number Limits

for high frequencies it becomes apparent that the lumped moment measurement from static data does not give the needed resolution of the separation induced force distribution. By using Liiva's moment loops, extracting camber and apparent mass effects, the minimum moment coefficient registered during the loop, corresponding to the lift overshoot, can be plotted versus pitch rate (Fig. 38c). As can be seen, this stall induced increase of the stabilizing moment correlates well with the pitch rate induced increase of $c_{l_{max}}$. It is expected that this separation induced moment increase could be defined from detailed static data. In the meantime, however, we are using the dynamic measurement of it (Fig. 38c).

As the angular rate $c\dot{\alpha}/U_\infty$ varies during the oscillation cycle, the determination of the dynamic stall overshoot in the oscillatory case is a little more involved than for the pure ramp function.

For harmonic oscillations in pitch the instantaneous angle of attack is

$$\alpha = \alpha_o + \Delta\theta \sin \omega t \tag{75}$$

The effective cross flow angle determining the separation is α^i, given by Eq. (72)

The stall angle is (see Eq. (31)*

$$\begin{aligned} \alpha_s + \Delta\alpha_s &= \alpha_s + K_{a_{\dot\theta}} \bar\omega \Delta\theta \cos(\omega t - \phi) \\ &\le \alpha_\beta + \Delta\alpha_{s_{max}} \end{aligned} \tag{76}$$

*In presence of static α-hysteresis, the lower (reattachment) value is used for α_s.

The stall on the oscillating airfoil occurs when $\alpha^i = \alpha_s + \Delta\alpha_s$, that is when the phase angle $\psi = \omega t$ is

$$\psi_s = \phi + \begin{cases} \arctan\left(K_{a_{\dot\theta}}\bar{\omega}\right) + \arcsin\left(\dfrac{\alpha_s - \alpha_o}{\Delta\theta\sqrt{1+\left(K_{a_{\dot\theta}}\bar{\omega}\right)^2}}\right); & \Delta\alpha_s < \Delta\alpha_{s_{max}} \\ \arcsin\left(\dfrac{\alpha_s + \Delta\alpha_{s_{max}} - \alpha_o}{\Delta\theta}\right); & \Delta\alpha_s = \Delta\alpha_{s_{max}} \end{cases} \tag{77}$$

The reattachment angle is $\alpha_s - \Delta\alpha_s$, according to our linearized assumptions, giving the following phase angle.

$$\psi_R = \phi + \pi - \begin{cases} \arcsin\left(\dfrac{\alpha_s - \alpha_o}{\Delta\theta\sqrt{1+\left(K_{a_{\dot\theta}}\bar{\omega}\right)^2}}\right) - \arctan\left(K_{a_{\dot\theta}}\bar{\omega}\right); & \Delta\alpha_s < \Delta\alpha_{s_{max}} \\ \arcsin\left(\dfrac{\alpha_s - \Delta\alpha_{s_{max}} - \alpha_o}{\Delta\theta}\right); & \alpha_s = \Delta\alpha_{s_{max}} \end{cases} \tag{78}$$

If the angular rate at stall were kept constant, the deep stall lift would carry the full increase $c_{l_{\alpha_d}} \cdot \Delta\alpha_s + \Delta c_{l_o}^*$ (Fig. 36). However the rate decreases as $\cos(\psi - \phi)$ and the c_l - increase is modulated (Figs. 36 and 39).

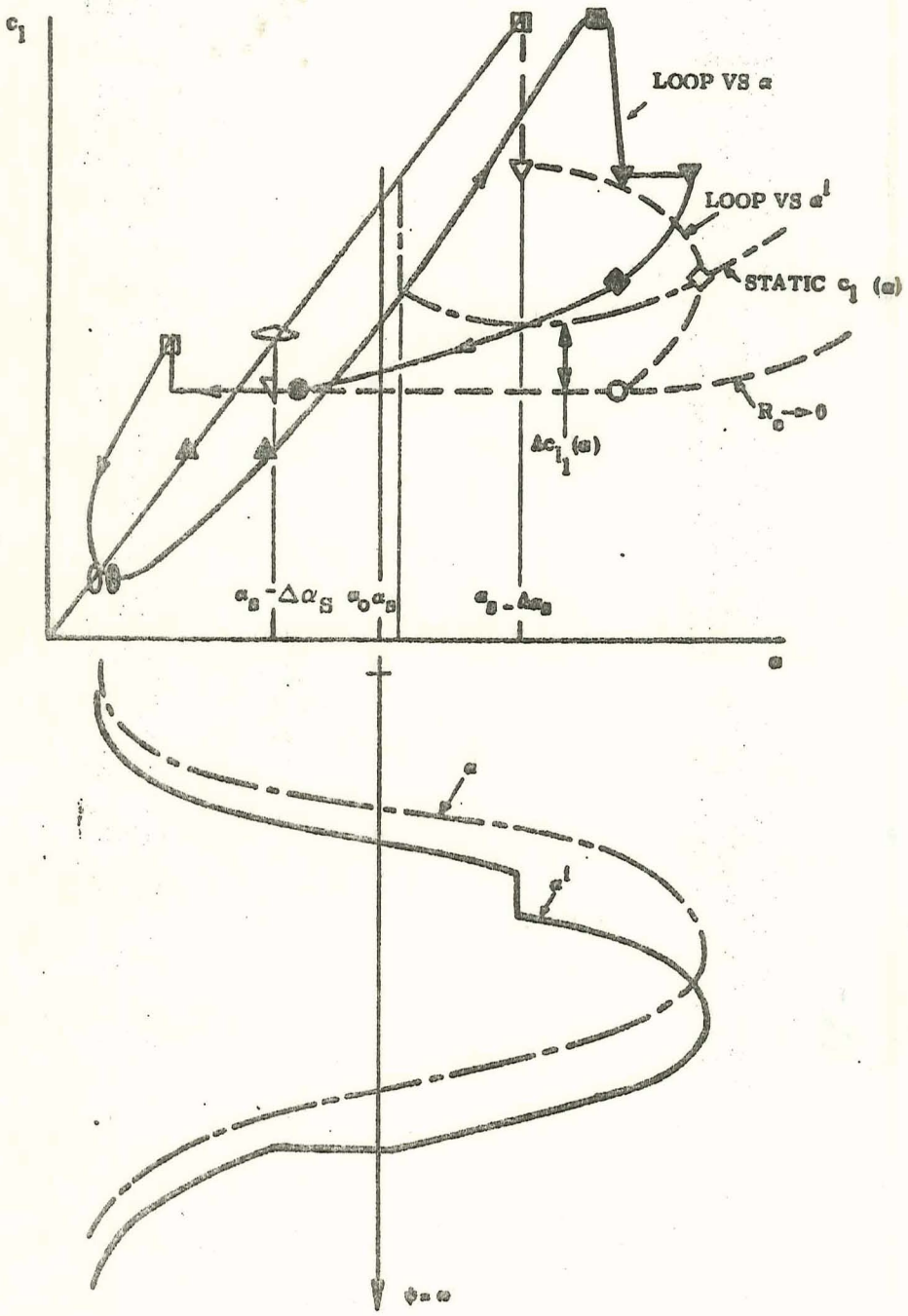

Figure 39 Oscillatory Stall Penetration

$$\Delta c_l^* = \Delta c_{l_{max}}^* \cos\left(\psi - \phi\right) \; ; \; \psi_s < \psi < \pi + \phi - \bar{\psi}$$

$$\Delta c_{l_{max}}^* = \left(\Delta c_{l_o}^* + c_{l_{\alpha_d}} \Delta\alpha_s\right) \Big/ \cos\left(\psi_s - \phi\right)$$

(79)

$$\bar{\psi} = \pi + \phi - \begin{cases} \arcsin\left(\dfrac{\alpha_s - \alpha_o}{\Delta\theta}\right); & \Delta c_{l_{max}}^* \leq \Delta c_{l_l}(\alpha) \\ \Delta\psi^* & ; \; \Delta c_{l_{max}}^* > \Delta c_{l_l}(\alpha) \end{cases}$$

$$\Delta c_{l_l} = c_l(\alpha) - c_l(\alpha)\; R_c \to 0$$

Having solved for the critical points, we know c_l as a function of the "separation-inducing" angle α^i. Those c_l-values are plotted as a function of the instantaneous value α in the $c_l - \alpha$-plane to construct the dynamic loops. Earlier, this transformation from α^i to α was done graphically (Ref. 6), using the $\alpha^i(\psi)$ and $\alpha(\psi)$ phase relationships in the bottom half of Fig. 39.

Experimental values of $K_{a_{\dot\theta}}$ obtained by Steiner (Ref. 64) on an NACA 0012 airfoil are used in the loop construction. Essentially, he measured the phase lag between static and dynamic stall from flow visualization results. The results for various frequencies and amplitudes are well correlated as a function of $c\dot\alpha/U_\infty$ (Fig. 28). These results indicate that $K_{a_{\dot\theta}}$ is a constant up to some critical pitch rate where the stall overshoot is limited, $\Delta\alpha_{s_{max}} = K_{a_{\dot\theta}} \left(\dfrac{\dot\alpha c}{U_\infty}\right)_{crit.}$ This gives further credence to the concept of the infinite Reynolds number limit for stall overshoot (as long as no

*It is assumed that $\Delta\theta$ is small enough so that $\Delta c_{l_{max}}^*$ can be assumed to be constant.

change of stall type occurs). In addition to these effects of α^i, the total lift also has components due to pitch rate induced attached flow type effects, which will further deform the dynamic loop shown in Fig. 39. The total lift coefficient is **(Ref. 7).

Attached Flow:

$$\psi_R \leq \psi \leq \psi_s$$

$$c_l(t) = c_l(\alpha_o) + \frac{A}{A_o} c_{l_\alpha} \Delta\theta \left\{ \sin(\psi - \phi) + \left[\left(0.5 - \xi_{CG}\right) + \frac{c_{l_\sigma}}{c_{l_\alpha}} \right] \bar{\omega} \cos(\psi - \phi) \right\}$$

$$+ \left(c_{l_{\dot{\theta}}}\right)_{AM} \Delta\theta\bar{\omega} \cos\psi - \left(c_{l_{\ddot{\theta}}}\right)_{AM} \Delta\theta\bar{\omega}^2 \sin\psi$$

$$A/A_o = \begin{cases} 1.000 & ; \ \bar{\omega} \leq 0.16 \\ 0.475 \left[1 + (10\bar{\omega})^{-1/2}\right] & ; \ \bar{\omega} > 0.16 \end{cases}$$

$$\phi = \begin{cases} 1.5\ \bar{\omega} & ; \ \bar{\omega} \leq 0.16 \\ 0.245 & \bar{\omega} > 0.16 \end{cases} \qquad (80)$$

**A similar expression is obtained for the pitching moment.

Using thin airfoil theory (Ref. 72) the camber derivative is $c_{l_\sigma} = \pi/2$ and the lift derivative $c_{l_\alpha} = 2\pi$, i.e., $c_{l_\sigma}/c_{l_\alpha} = 1/4$. Experimental data is used for c_{l_α}, and only the ratio $c_{l_\sigma}/c_{l_\alpha}$ is determined from thin airfoil theory. The apparent mass derivatives are (Ref. 72A), $\left(c_{l_{\dot\theta}}\right)_{AM} = \pi/2$, $\left(c_{l_{\ddot\theta}}\right)_{AM} \quad \frac{\pi}{2}\,(0.5 - \left(\xi_{CG}\right)$

Separated Flow:

$$\psi_s < \psi < \psi_R$$

$$c_l(t) = c_l(\alpha_o) + c_{l_\alpha}(\alpha_s - \alpha_o + \Delta\alpha_s) + \sum_o^N \left\{ \frac{A}{A_o} c_{l_{\alpha_n}} \Delta\theta \right.$$

$$\left. \left[\sin(\psi - \phi) + (0.5 - \xi_{CG})\,\bar\omega \cos(\psi - \phi) \right] \right\}$$

$$+ \frac{A}{A_o} c_{l_{\sigma_s}} \Delta\theta\bar\omega \cos(\psi - \phi) + \left(c_{l_{\dot\theta}}\right)_{AM_s} \Delta\theta\bar\omega \cos\psi$$

$$- \left(c_{l_{\ddot\theta}}\right)_{AM_s} \Delta\theta\bar\omega^2 \sin\psi + \Delta i c_l$$

$$\Delta^i c_l = -\Delta c_{l_s} - c_{l_o}^* - c_{l_\alpha} \Delta\alpha_s + \begin{cases} \Delta c_{l_{max}}^* \cos(\psi - \phi - \phi_s); & \psi_s < \psi < \pi + \phi + \phi_s - \Delta\psi \\ -\left[c_l - c_l(R_e \to 0)\right] & \pi + \phi + \phi_s - \Delta\psi < \psi < 2\pi + \psi_R \end{cases}$$

$$\Delta\psi = \text{smallest of} \begin{cases} \arcsin \dfrac{\alpha_s - \alpha_o}{\Delta\theta} \\ \Delta\psi^* \end{cases}$$

$$\Delta\alpha_s = K_{a_{\dot\theta}}\,\bar\omega\,\Delta\theta\,\cos(\psi_s - \phi)$$

$$\phi_s = \xi_{a_s} \bar{\omega}$$

$$\left[c_l - c_l\left(R_e \to 0\right)\right] = \sum_{o}^{m} \Delta c_{l_{N-m}} + \Delta c_{l_{\alpha_{N-m}}} \left(\alpha_o - \alpha_{N-m}\right)$$

$$+ \Delta c_{l_{\alpha_{N-m}}} \Delta\theta \sin\left(\psi - \phi\right) \tag{81}$$

$\Delta\psi^*$ is given by the intersection between

$$\Delta c_l^* = \Delta c_{l_{max}}^* \cos\left(\psi - \phi - \phi_s\right)$$

and

$$\left[c_l - c_l\left(R_e \to 0\right)\right] = \sum_{o}^{m} \Delta c_{l_{N-m}} + \Delta c_{l_{\alpha_{N-m}}} \left(\alpha_o - \alpha_{N-m}\right)$$

$$+ \Delta c_{l_{N-m}} \Delta\theta \sin\left(\psi - \phi\right)$$

$$\Delta\psi^* = \beta + \cos^{-1}\left\{ - \frac{\left[\sum_{o}^{m} \Delta c_{l_{N-m}} + \Delta c_{l_{\alpha_{N-m}}} \left(\alpha_o - \alpha_{N-m}\right) \cos\beta\right]}{\Delta c_{l_{max}}^* - \Delta c_{l_{\alpha_{N-m}}} \Delta\theta \sin\phi_s} \right\}$$

$$\beta = \tan^{-1}\left[\frac{\Delta c_{l_{\alpha_{N-m}}} \Delta\theta \cos\phi_s}{\Delta c_{l_{max}}^* - \Delta c_{l_{\alpha_{N-m}}} \sin\phi_s}\right] \tag{82}$$

The camber effect after stall is the same as the attached flow value, as indicated by static airfoil data (Ref. 55). Likewise the apparent mass effects remain the same. Conversely, the angle of attack effect (whether it is the result of attitude or pitch rate) varies with the local c_{l_α}. In the present case the lift curve slope is approximated by a series of straight lines such that $c_{l_{\alpha_n}}$ applies over the interval, $\alpha_{n-1} \leq \alpha \leq \alpha_n$, i.e. when the phase angle ψ is (See Fig. 39)

$$\sin^{-1}\left(\frac{\alpha_{n-1} - \alpha_o}{\Delta\theta}\right) \leq \psi - \phi - \phi_s \leq \sin^{-1}\left(\frac{\alpha_n - \alpha_o}{\Delta\theta}\right) \tag{83}$$

On the return stroke linearity of the stall delay is assumed; thus, the limiting or critical downstroke lift curve is shifted negatively an amount equal to the stall delay, Eqs. (31) and (32).

The applicable ψ-range for $c_{l_{\alpha_n}}$ on the downstroke is then given by Eq. (83) with $\psi + \pi$ substituted for ψ. This holds as long as the zero Reynolds number limit is not exceeded. That is, as long as $\psi < \pi + \phi + \phi_s + \Delta\psi^*$ where $\Delta\psi^*$ is given by Eq. (8).

Generally the pitching moment expression is similar. It contains contributions due to lift and the moment about the aerodynamic center, i.e., $c_m = c_l\left(\xi_{AC} - \xi_{CG}\right) + c_{m_{AC}}$. The two apparent mass forces are centered at the 50% chord position. In addition, there are two $c_{m_{AC}}$-terms, viz: $(c_{m_\sigma})_{AC} = -\pi/8$ and $(c_{m_{\ddot{\theta}}})_{AC} = -\pi/64$. Figure 40 shows the lift and moment values thus obtained for a typical case plotted versus the instantaneous angle of attack $\alpha = \alpha_o + \Delta\theta \sin\psi$.

3.5 AERODYNAMIC DAMPING

Having the aerodynamic characteristics defined analytically for the complete dynamic loop, as described in the previous section, one can formulate in explicit form the energy dissipation per cycle and define an effective dynamic damping derivative, similarly to what was done earlier for the rigid body damping of blunt reentry bodies with separated flow (Refs. 73, 74). The work per cycle extracted from the aerodynamic forces for an airfoil oscillating in pitch around a fixed center of gravity is

$$W = \frac{\rho U^2}{2} Sc \int_{t_o}^{t_o + T} c_m(t)\, d\theta = \frac{\rho U^2}{2} Sc \int_{t_o}^{t_o + T} c_m(t)\, \dot{\theta} dt$$

$$= \frac{\rho U^2}{2} Sc \int_{t_o}^{t_o + T} c_{m_{\dot{\theta}}} \frac{\dot{\theta} c}{U}\, \dot{\theta} dt \qquad (84)$$

$c_{\bar{m}_{\dot{\theta}}}$ is the linear measure of the energy dissipation, i.e., $c_{\bar{m}_{\dot{\theta}}}$ is an effective damping derivative defined by

$$c_{\bar{m}_{\dot{\theta}}} = \frac{\int_{t_o}^{t_o + T} c_m(t)\, \dot{\theta} dt}{\frac{c}{U} \int_{t_o}^{t_o + T} \dot{\theta}^2 dt} \qquad (85)$$

For the airfoil describing harmonic oscillations in pitch, $\theta = \Delta\theta \sin\omega t$ where $\omega t = \psi$ is the phase angle of the pitch oscillation, the effective damping derivative becomes simply

$$\bar{c_m}_{\dot{\theta}} = \frac{1}{\pi \Delta\theta \bar{\omega}} \int_{\psi_o}^{\psi_o + 2\pi} c_m(\psi) \cos \psi \, d\psi \tag{86}$$

c_m is determined by the center of gravity location, ξ_{CG}, and the effective angle of attack.

$$\begin{aligned} c_m(\psi) &= c_m\left(\xi_{CG}, \tilde{\alpha}\right) \\ &= c_m(0.25, \tilde{\alpha}) - \left(\xi_{CG} - 0.25\right) c_n(\tilde{\alpha}) \end{aligned} \tag{87}$$

$c_n(\tilde{\alpha})$ and $c_m(0.25, \tilde{\alpha})$ are given by Eqs. (77)-(83) with c_n- and c_m- derivatives substituted for the c_l-derivatives.

Section 4
DISCUSSION OF RESULTS

The construction of the dynamic lift and moment loops has been mechanized as has the computation of the aerodynamic damping. Sample results are shown in Figure 40 and compared with Liiva's experimental measurements (Ref. 37). The agreement is quite good, particularly for the moment curves which are indicative of the torsional aerodynamic damping. This is borne out by the computed damping results which are in excellent agreement with Liiva's measurements at low reduced frequency (Figure 41).

The present results do not agree with the measured values quite as well as did the previous graphical technique of Ref. 6 (compare Figures 25 and 40). The primary areas of disagreement for stall penetration are at stall and reattachment. This is due in part to the fact that the representation of stall used in the present computer program is rather simplistic compared to the somewhat subjective graphical technique used earlier. The present computer technique neglects the fall off in lift preceding stall, and assumes a simultaneous, discontinuous change in phase lag. The graphical technique approximated the lift fall off prior to stall and faired out the change in phase lag over a two degree amplitude range. Certainly the lift fall off is real and could be accounted for in the program by using as sophisticated a fit to the lift curve as desired. A more reasonable approach to the phase lag variation would be to start lagging the lift loss where separation starts (that is, where the lift fall off begins), and to increase the lag to reach the full separation lag at stall. Figure 42 illustrates such a scheme where the phase lag is varied linearly between these two points. This certainly does improve both lift and moment loops and the high frequency loops are now predicted a great deal better than with the earlier method (Ref. 6). Liiva's lift and moment loops are predicted fairly well (Ref. 37 and Figures 43 and 44). For the moment construction in Figure 44, the Δc_m^* extrapolated from Liiva's dynamic test (Figure 38c) is used. However, with detailed load distribution data the Δc_m^*-term could be determined in a static experiment. Once it is determined, however,

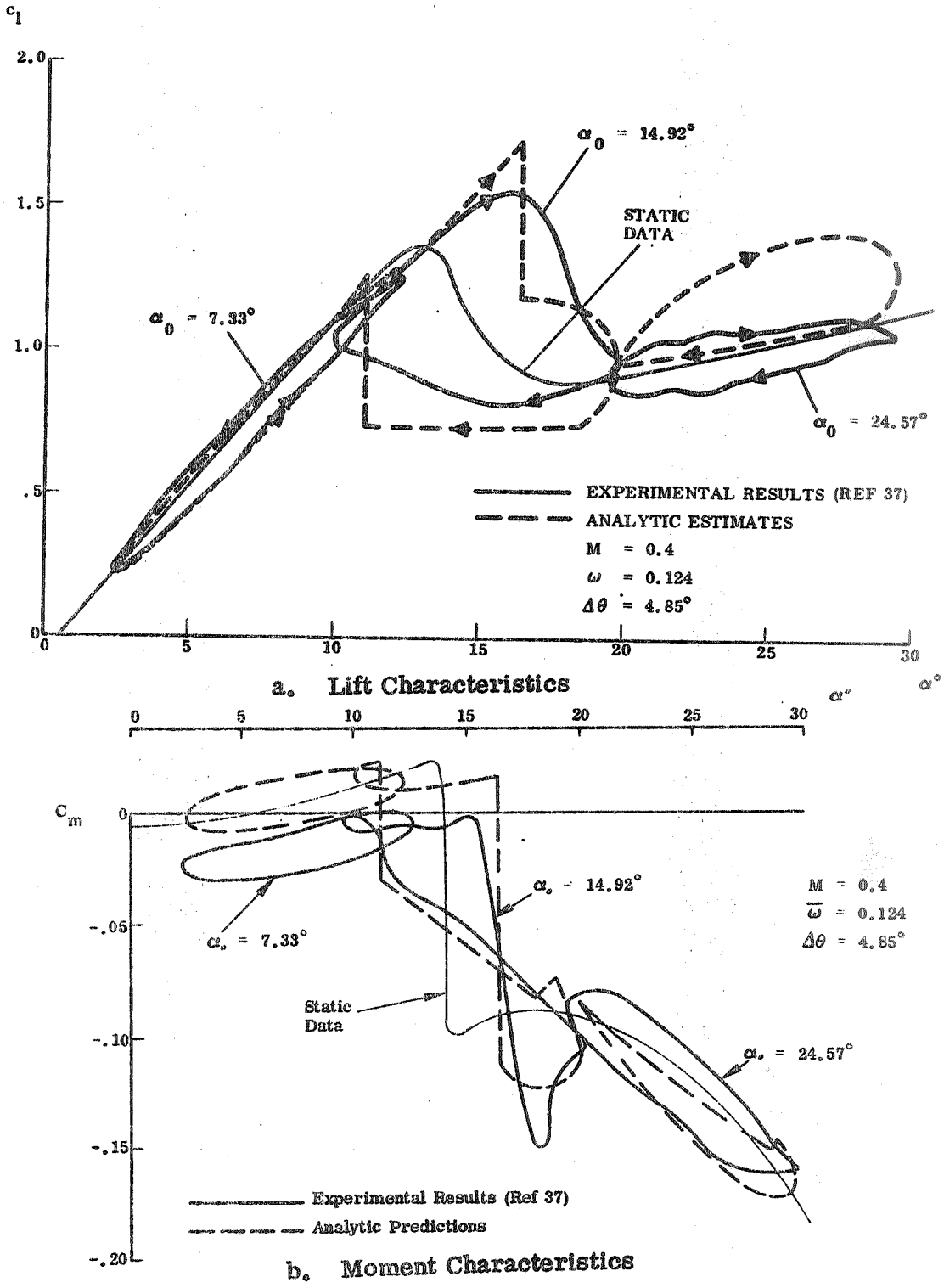

Figure 40 Predicted and Measured Dynamic Loops at Low Frequency

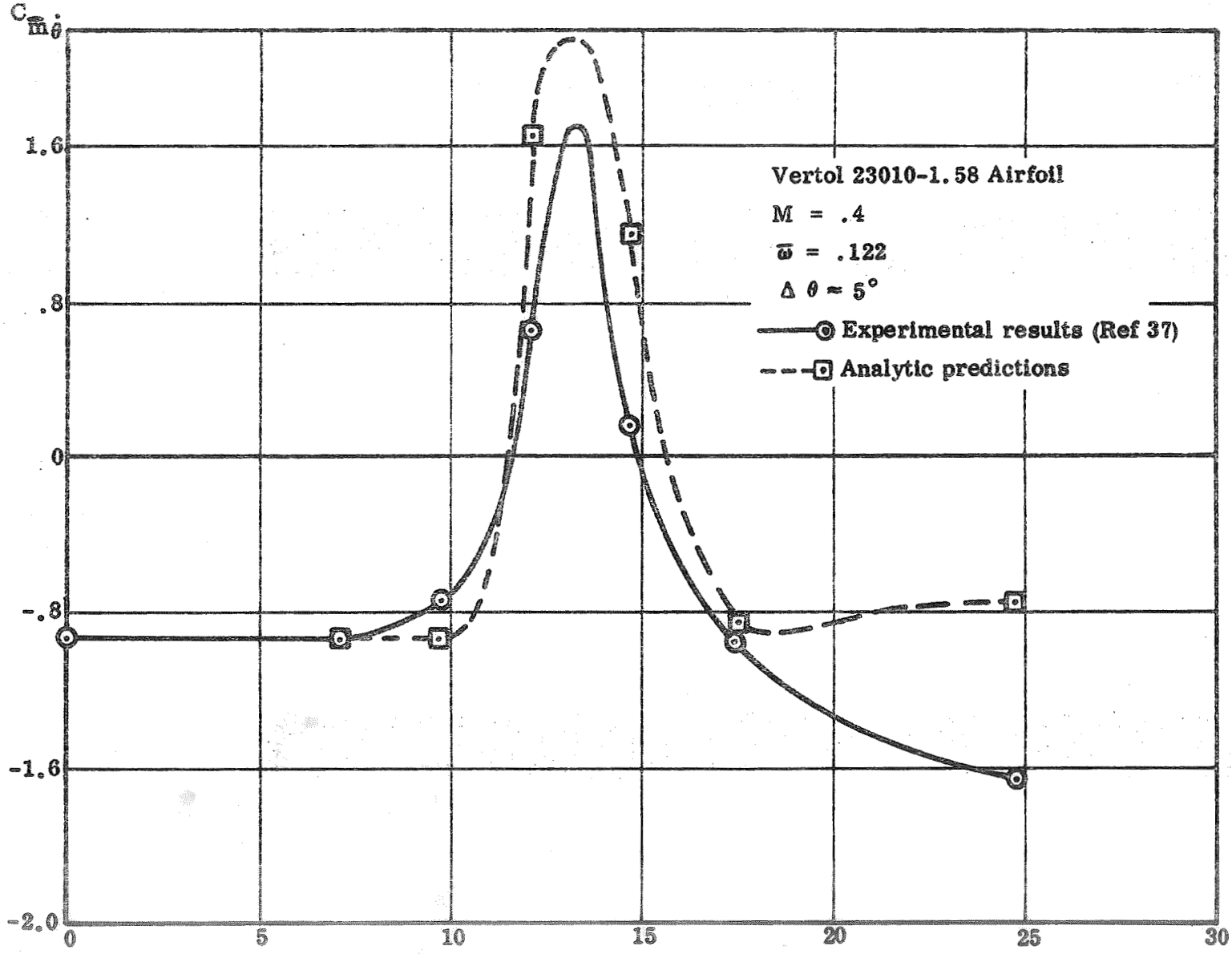

Figure 41 Predicted and Measured Pitch Damping at Low Frequency

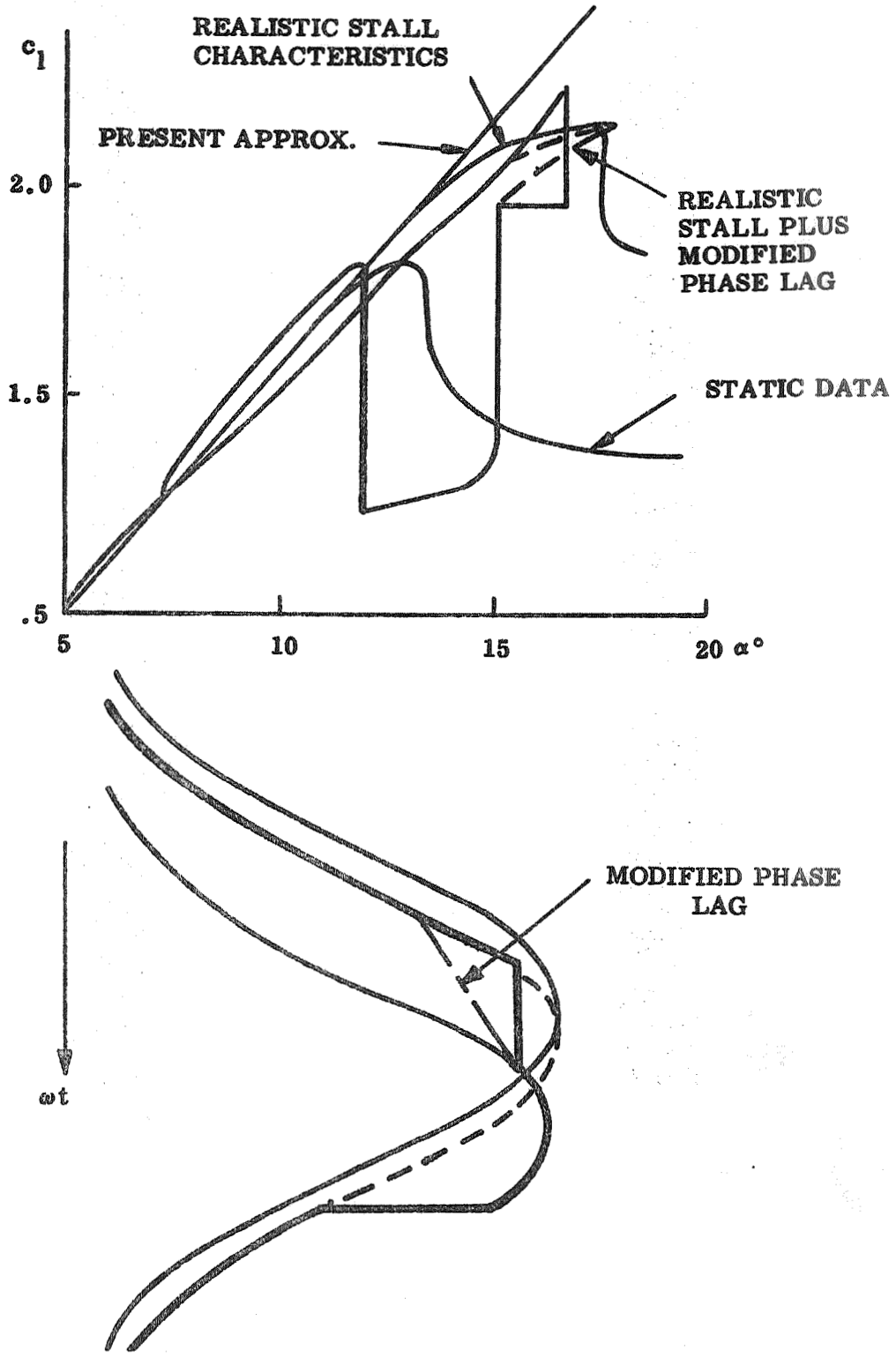

Figure 42 Needed Modifications of the Present Analytical Method

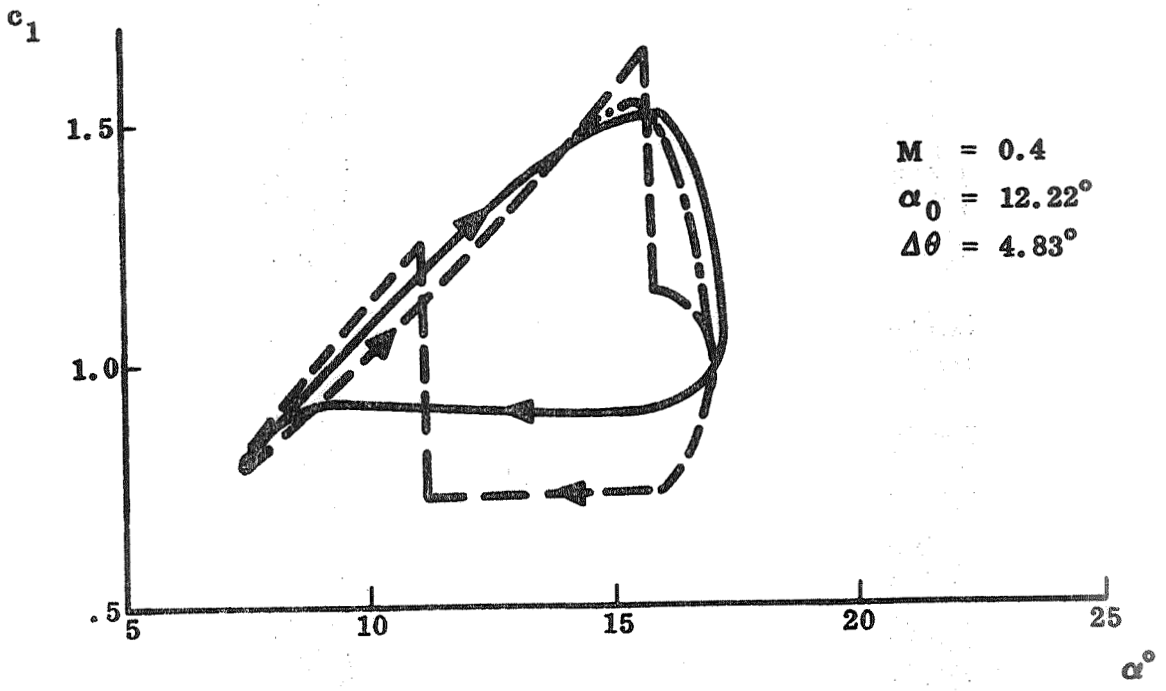

a) $\bar{\omega}$ = .124

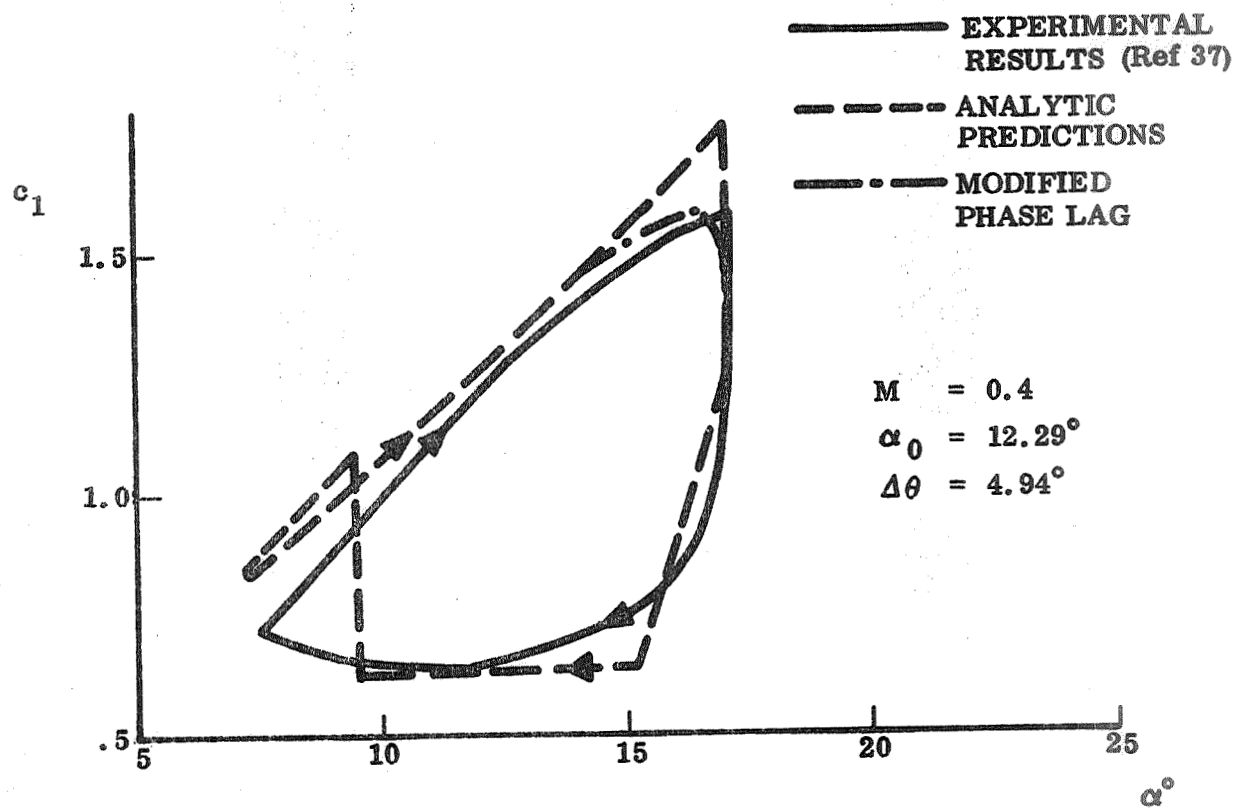

b) $\bar{\omega}$ = .248

Figure 43 Predicted and Measured Dynamic Lift Loops at Various Frequencies

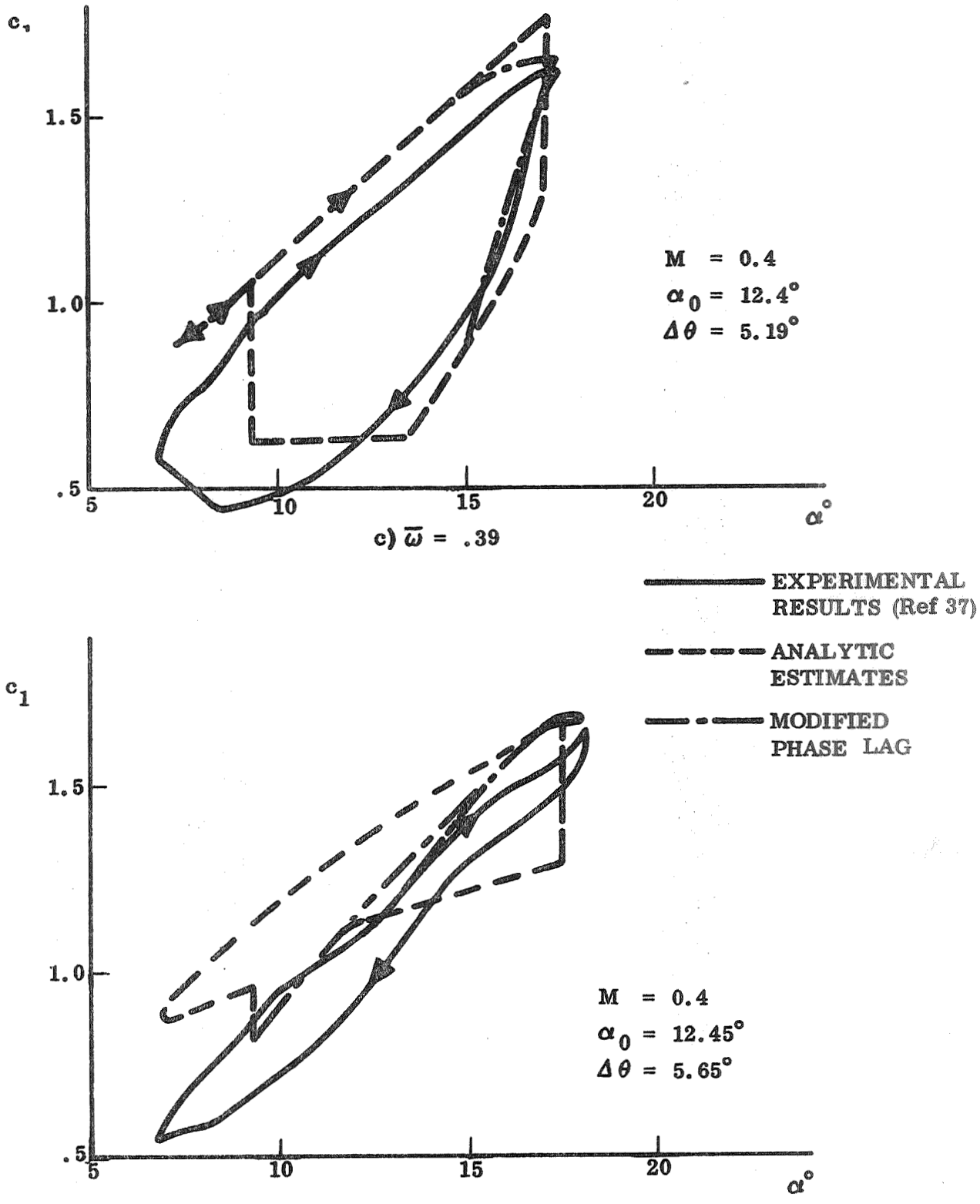

Figure 43 Predicted and Measured Dynamic Lift Loops at Various Frequencies

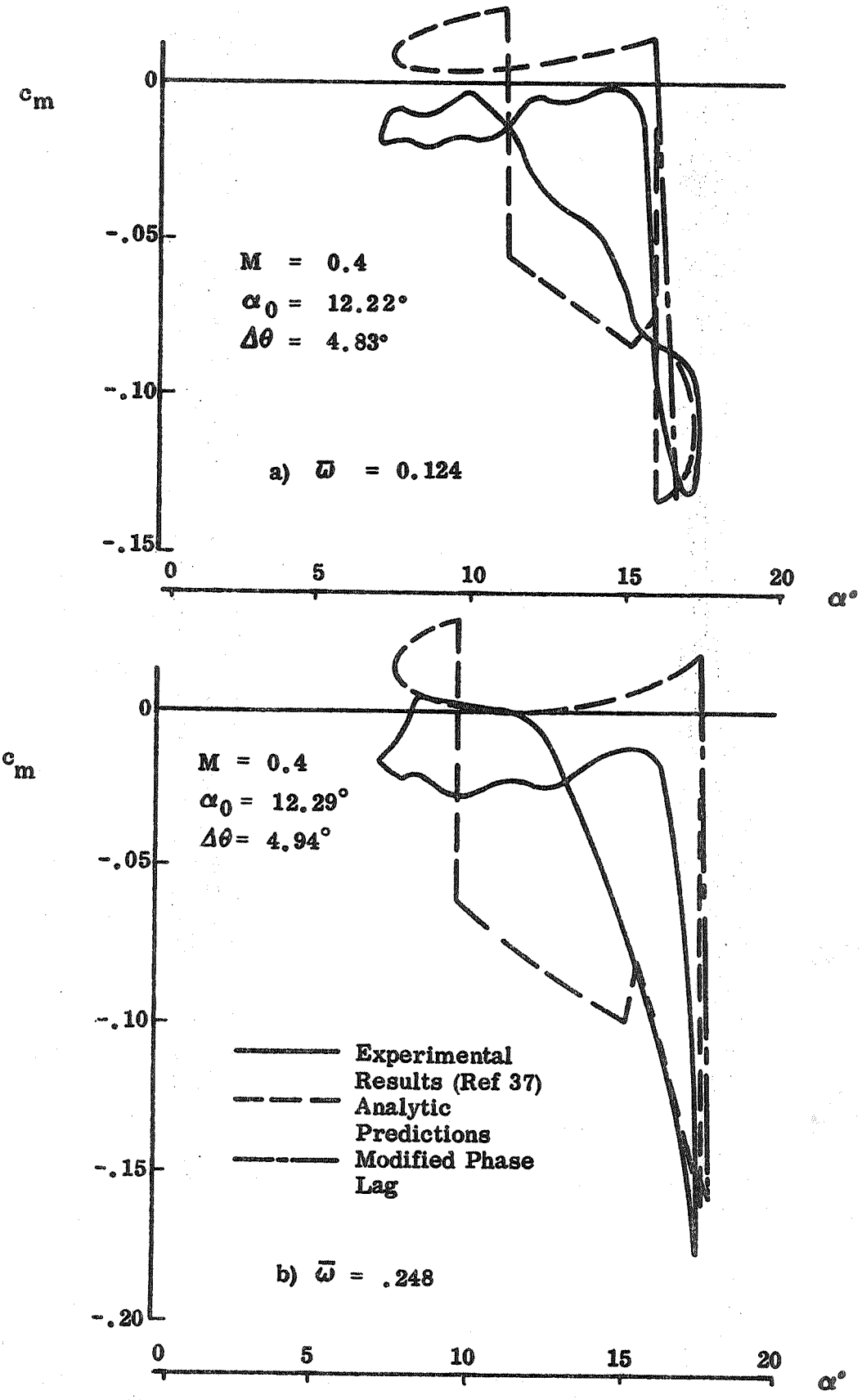

Figure 44 Predicted and Measured Dynamic Moment Loops at Various Frequencies

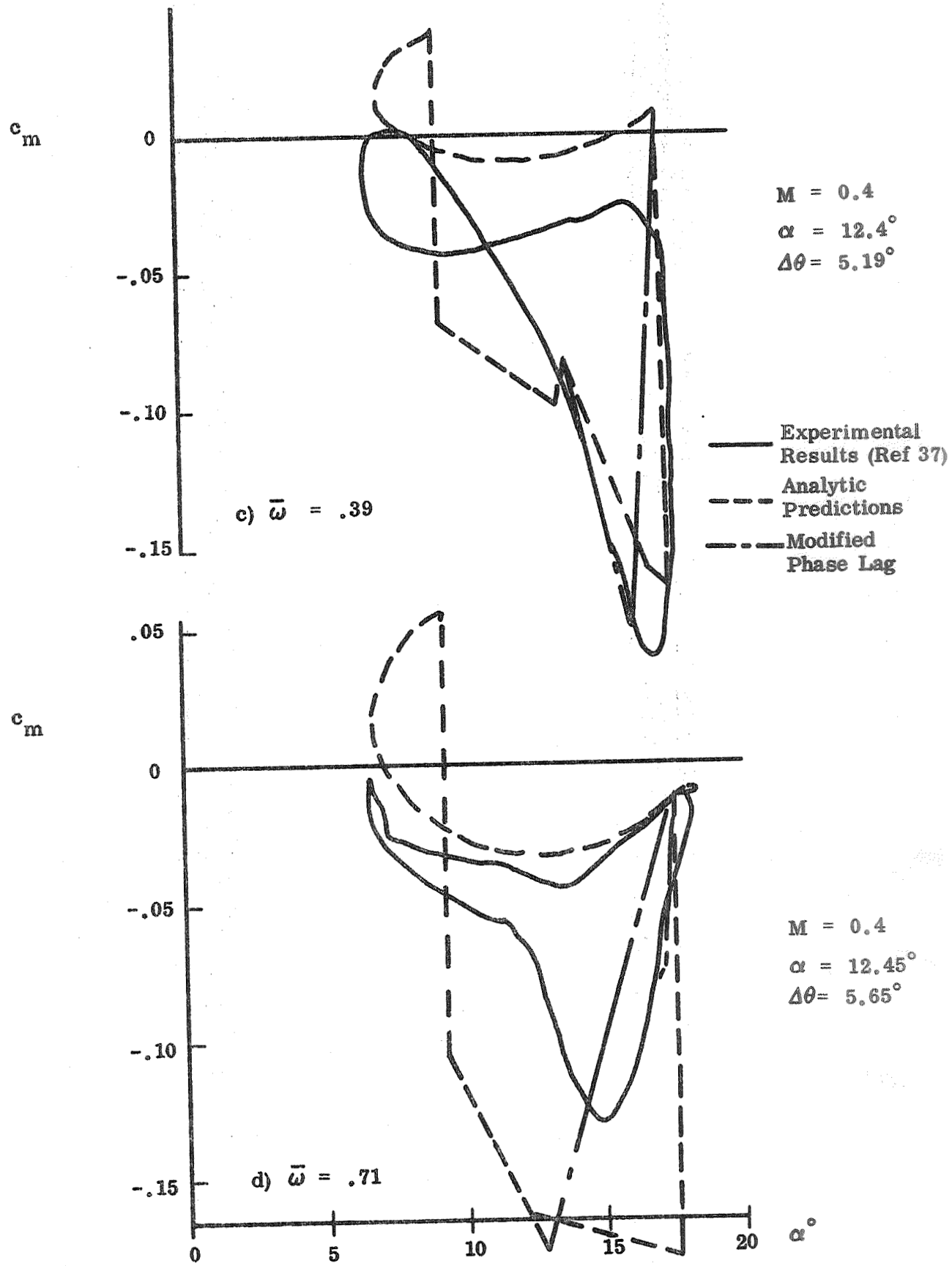

Figure 44 Predicted and Measured Dynamic Moment Loops at Various Frequencies

it should agree with this dynamic measurement as well as the $c_{l_{max}}$ -overshoot does (Figure 38a). That is, the data in Figure 38 can be used to "extrapolate analytically" to other test conditions and also to other airfoils as long as the stall type does not change.

The present mechanized technique shows poorer agreement with measurements in the deep stall region than the earlier graphical method (compare α_o = 24.57 characteristics of Fig. 25 and 40). This is the result of using the values of $\Delta c^*_{l_{max}}$ and $\Delta c^*_{m_{max}}$ at the trim angle of attack. In reality these quantities are a maximum at α_s and decrease to zero at higher angle of attack (Fig. 36). By accounting for the variation of $\Delta c^*_{l_{max}}$ and $\Delta c^*_{m_{max}}$ in a more sophisticated computer program the agreement with experiment will be significantly improved.

While the agreement could be better, especially in regard to the reattachment characteristics, the agreement is good enough for preliminary design purposes, and assures us that the main characteristics of unsteady airfoil stall are described by the present analysis. Much of the deviations is probably due to nonlinear effects, in regard to both amplitude and phase modulation, which are not described by the present pseudo-linear theory. That the theory still represents a decisive improvement in our understanding of unsteady airfoil stall is revealed by Figure 45. Even after elaborate curve fitting and data smoothing operations, Carta et al. cannot predict the original dynamic loops‡ (Ref. 59) as well as the present analytic theory can, using only static data as an input (compare Figures 44 and 45).

‡ From which they sampled discrete data points to determine the coefficients in the "analytic extrapolation formula."

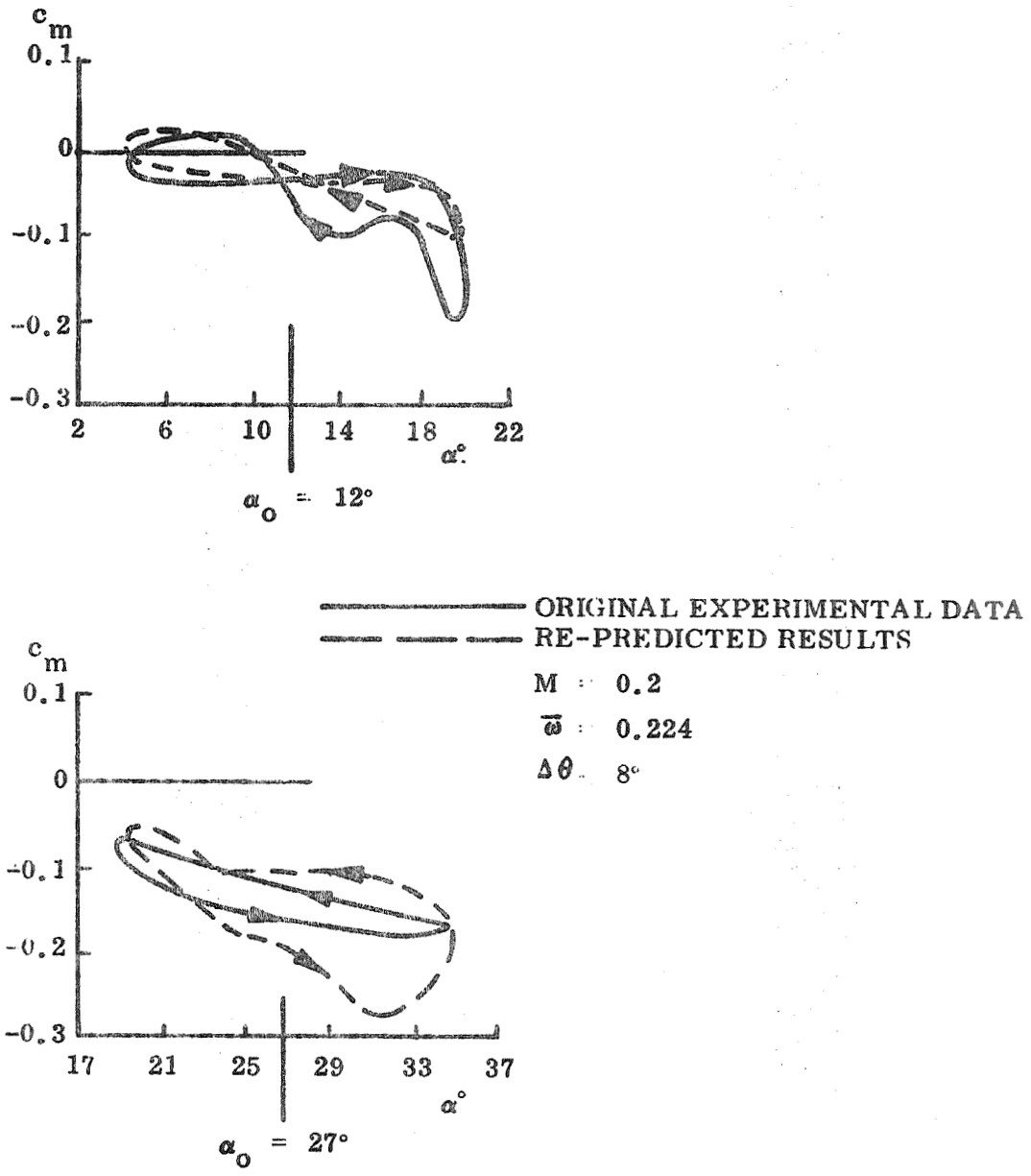

Figure 45 Comparison Between Original and Reconstructed Dynamic Pitching Moment Loops for NACA = 0012 Airfoil (Ref. 59)

Section 5
PREDICTION OF SPACE SHUTTLE STALL FLUTTER

The validity of the present method in predicting the dynamics of airfoil sections has already been demonstrated. However, the reason for developing such a technique is to provide a useful tool in predicting the stall flutter of a full scale flight vehicle. The impetus in this case was to provide a means of predicting the stall flutter of the straight wing space shuttle vehicle as it pitches downward through the stall region during the transition maneuver (Refs. 5 and 75, Figure 46).

Perhaps the most difficult, at least the most frustrating, aspect of applying the present technique to a practical wing is the difficulty of obtaining the necessary static input data. The first step is to extrapolate two-dimensional incompressible static data to finite aspect ratio (AR = 7.36 in case of the flutter test data in Figure 46). Standard methods (e.g., Ref. 76) give

$$C_{L_\alpha} = \frac{c_{l_\alpha}}{1 + c_{l_\alpha}/\pi AR} \tag{88}$$

The increase in stall angle α_s due to finite aspect ratio is simply

$$\left(\Delta\alpha_s\right)_{AR} = \frac{C_{L_{MAX}}}{C_{L_\alpha}} \frac{c_{l_{max}}}{c_{l_\alpha}} \tag{89}$$

Assuming that the maximum lift is unchanged, $C_{L_{MAX}} = c_{l_{max}}$, Eqs. (88) and (89) give

$$\left(\Delta\alpha_s\right)_{AR} = \frac{c_{l_{max}}}{\pi AR} \tag{90}$$

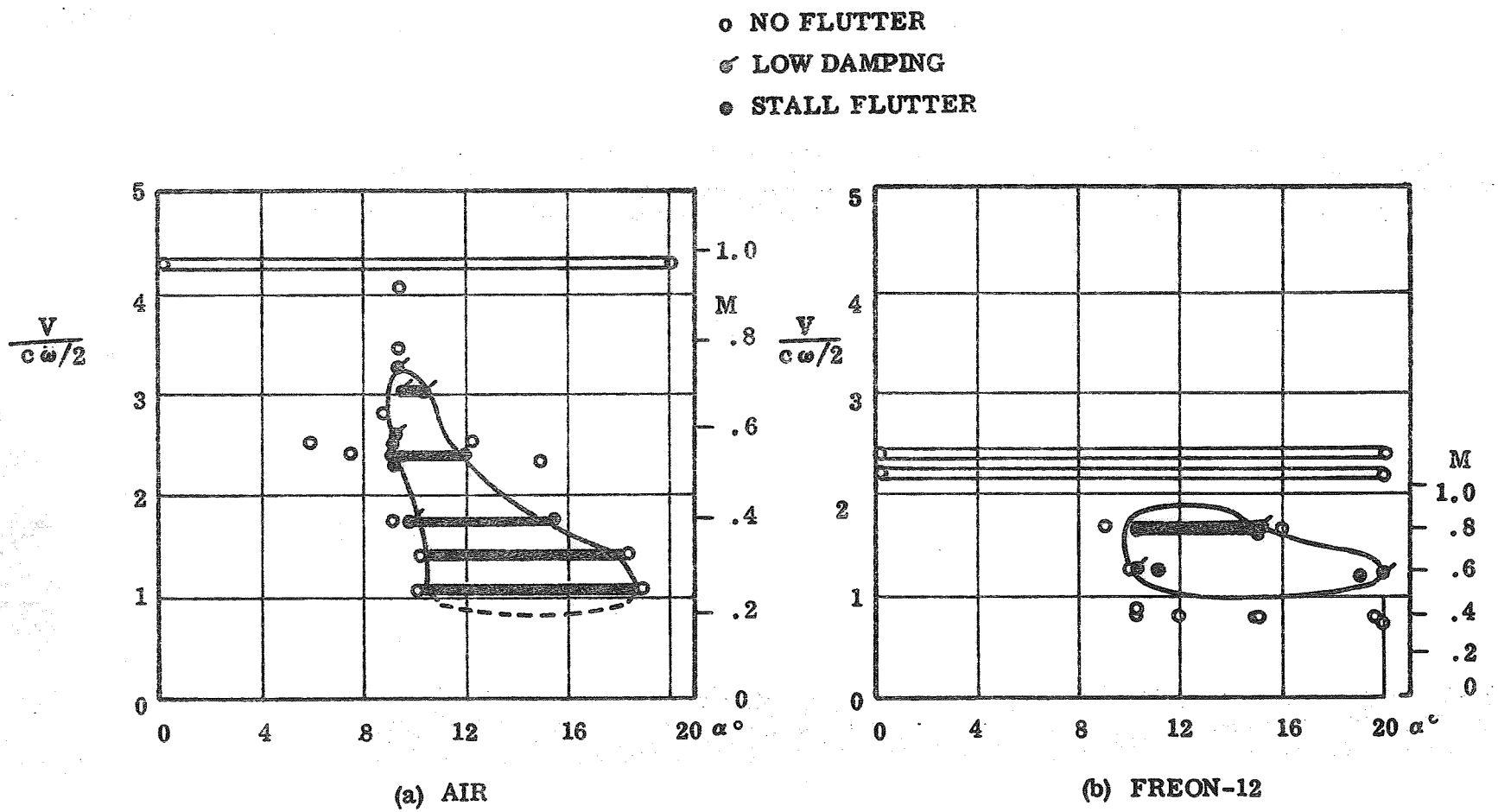

Figure 46 Variation of Flutter Velocity Coefficient with Angle of Attack for a NACA 64-012 Airfoil (Ref. 75)

Although the assumption of unchanged maximum lift may be challenged, the correction for aspect ratio is rather straightforward. One has more trouble in extrapolating incompressible data to cover the Mach range of the flutter test, $0.2 \leq M \leq 0.8$. One unforeseen problem was the definition of "incompressible" in regard to airfoil stall data. It is standard practice to assume that wind tunnel tests performed below $M_\infty = 0.4$ give essentially incompressible results. While this is a good assumption for most test data of interest, it is completely false in the case of stall data. The peak velocity on the airfoil near stall is several times higher than it is at more moderate angles of attack. Using again the handy French formula, Ref. 12 and Eqs. (14) and (15), gives

$$\left(\frac{U_e}{U_\infty}\right)_{max} = \left[1 + \frac{\left(1 + \sqrt{\frac{\rho_N}{2}}\right)^2 \alpha^2}{\rho_{N/2}}\right]^{1/2} \tag{91}$$

The effect of angle of attack on peak velocity ratio, as defined by Eq. (91), is illustrated by a carpet plot (Ref. 77 and Figure 47) for the $\rho_N - \alpha$ - range of interest. For a typical nose radius, e.g., $\rho_N = 1\%$, the tunnel Mach number would have to be $M_\infty = 0.1$ in order to correspond to the low angle of attack assumption for incompressibility, i.e., $M_e \leq 0.4$. Thus, for all practical purposes there is no such thing as incompressible airfoil stall. Unfortunately, the experimentalists have not remembered that, and for most of the available static stall data there is no information about what Mach number the test was performed at; M = .15 or M = .3? It makes a big difference!

That the effect of free stream Mach number on static and dynamic stall indeed is large is demonstrated by airplane pull-up data (Refs. 31, 32, and Figures 48 and 49). The variation of $C_{L_{MAX}}$ with Mach number seems to follow the relationship

$$\frac{\left(C_{L_{MAX}}\right)_2}{\left(C_{L_{MAX}}\right)_1} = \left(\frac{1 - M_2^2}{1 - M_1^2}\right)^2 \tag{92}$$

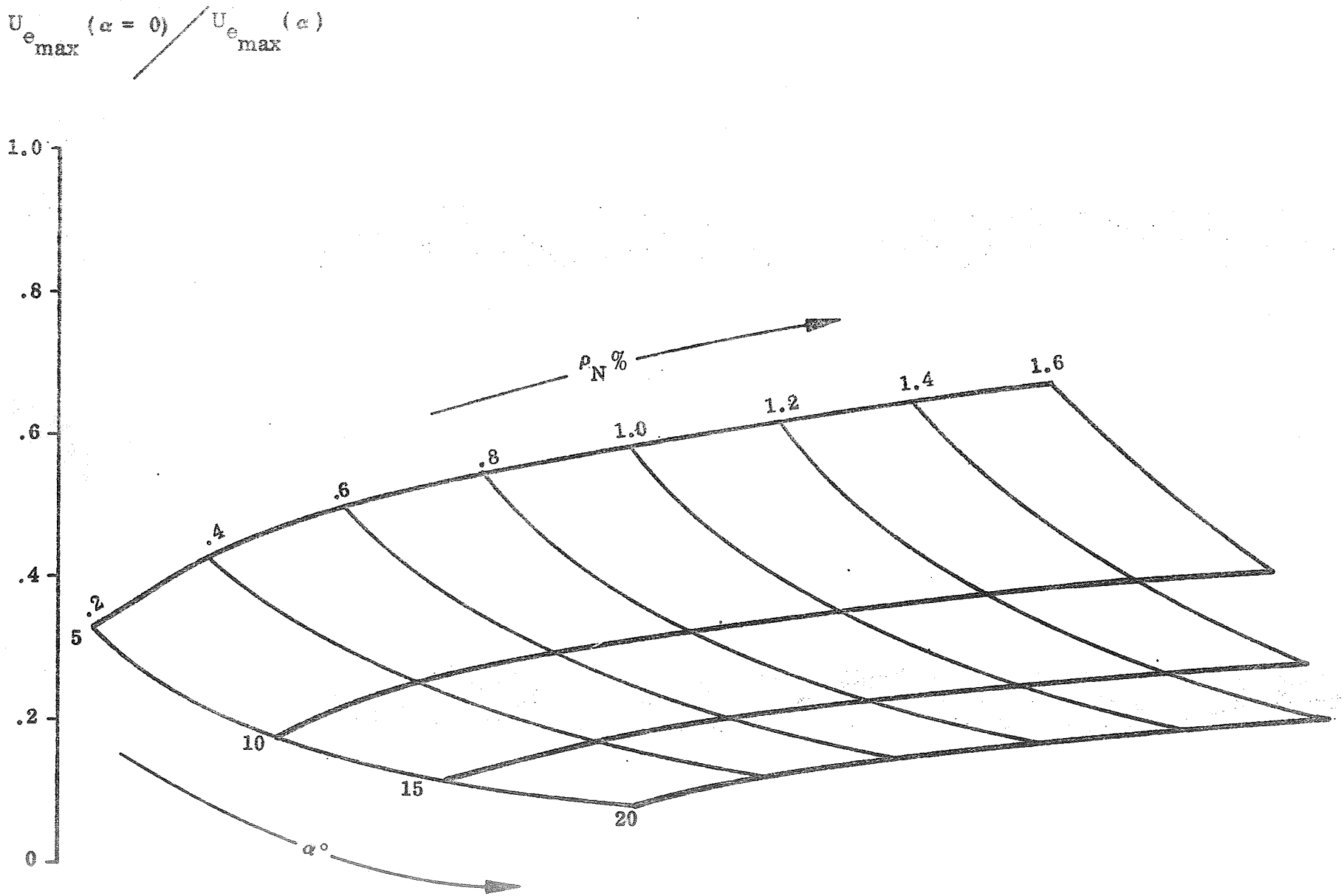

Figure 47 Ratios Between Peak Velocities at $\alpha = 0$ and $\alpha > 0$ as a Function of Nose Radius and Angle of Attack

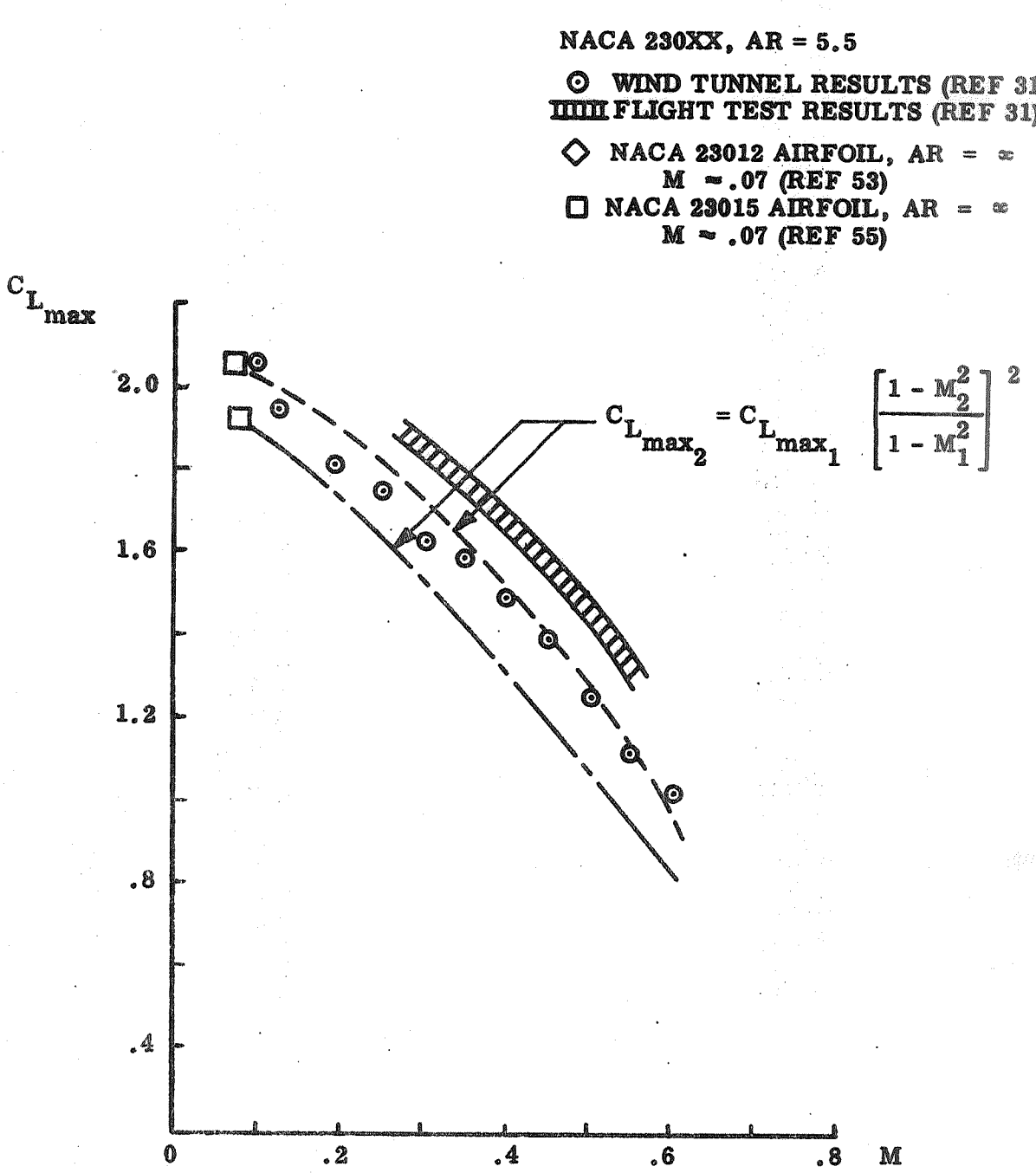

Figure 48 Maximum Lift as a Function of Mach Number for the NACA 230XX-Airfoil

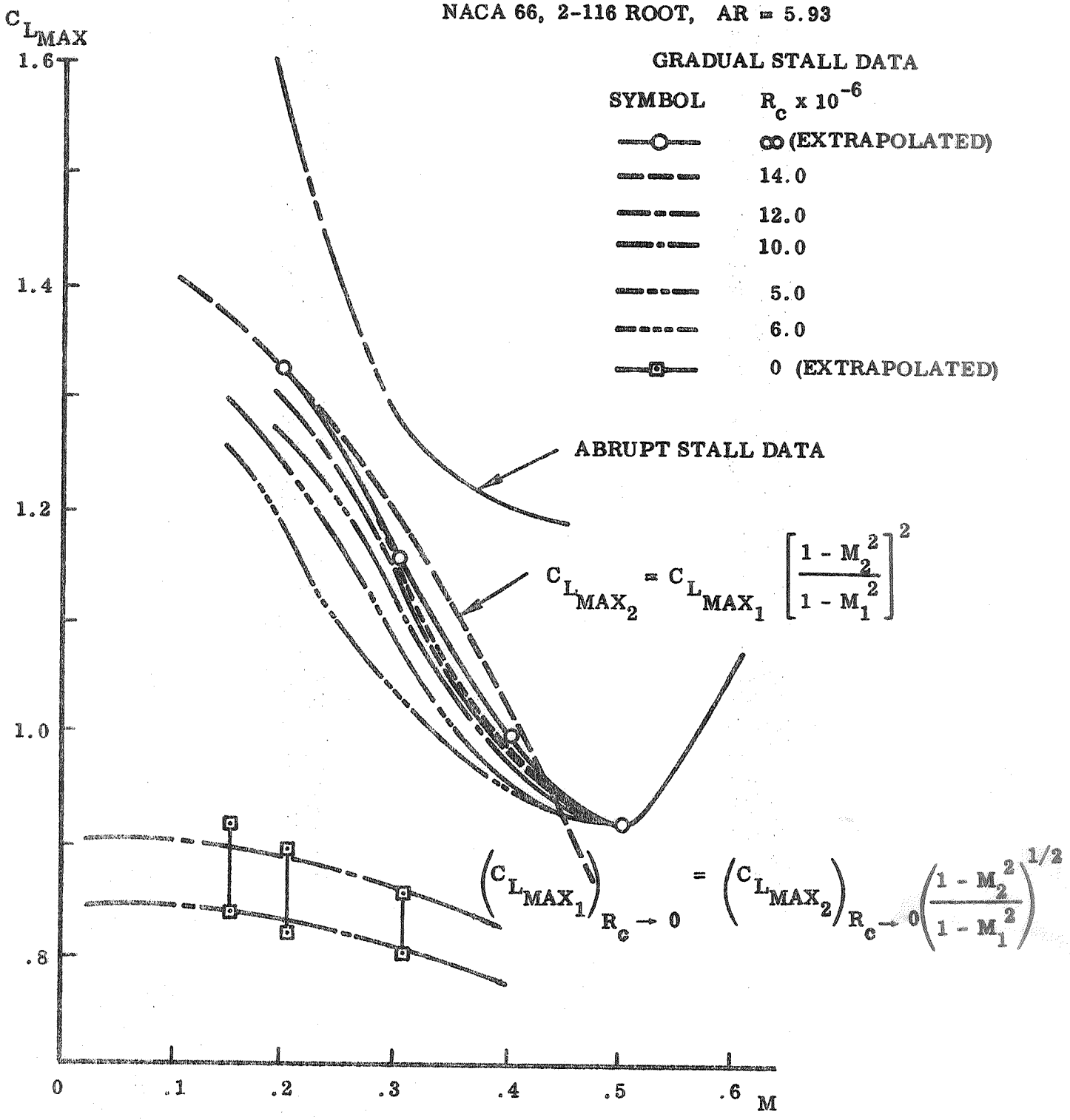

Figure 49 Maximum Lift as a Function of Mach Number and Reynolds Number for NACA 66-Series 16 Percent Thick Airfoil

There is no theoretical basis for this curve fit, but it works rather well for both flight and wind tunnel stall data of the 230XX airfoil (Ref. 31 and Figure 48), as well as for the mixed LE-TE stall and pure trailing edge stall of the 66-series wing (Ref. 32 and Figure 49). Extrapolating the data in Figure 49 (Ref. 32) to zero Reynolds number gives the $C_{L_{MAX}}$ correlation (See Figure 49).

$$\left[\frac{\left(C_{L_{MAX}}\right)_2}{\left(C_{L_{MAX}}\right)_1}\right]_{R_c \to 0} = \left(\frac{1 - M_2^2}{1 - M_1^2}\right)^{1/2} \tag{93}$$

There is no firm theoretical basis for this curve fit either, but it makes sense that the effect of compressibility is much less for the case where the separation point is fixed, which is the physical interpretation of the zero Reynolds number limit.

The lift curve slope variation with Mach number (Ref. 78 and Figure 50) is well predicted by the Prandtl-Glauert compressibility factor (Ref. 43)

$$c_{l_{\alpha_2}} / c_{l_{\alpha_1}} = \left(1 - M_1^2\right)^{1/2} \Big/ \left(1 - M_2^2\right)^{1/2} \tag{94}$$

If the linear relation $C_{L_{max}} = C_{L_\alpha} \alpha_s$ is used, Eqs. (92) - (94) define the following Mach number sensitivity for the stall angles

$$\frac{\alpha_{s_2}}{\alpha_{s_1}} = \left(\frac{1 - M_2^2}{1 - M_1^2}\right)^{n_R} ; \quad n_R = \begin{cases} 5/2 \; ; \; R_e \gg 0 \\ 1 \; ; \; R_e \to 0 \end{cases} \tag{95}$$

Stall flutter is the result of the aerodynamic negative damping that occurs when the stall is penetrated, as was discussed earlier. There is, of course, a strong relationship between the static α-M stall boundary and the stall flutter α-M boundary. Comparing Figure 46 with the separation boundaries defined by Pearcy (Ref. 39 and Figure 51) indicates clearly the similarity for the low α-M flutter boundary. If one uses the α-M-separation boundaries measured on a wing with a 65A012 airfoil

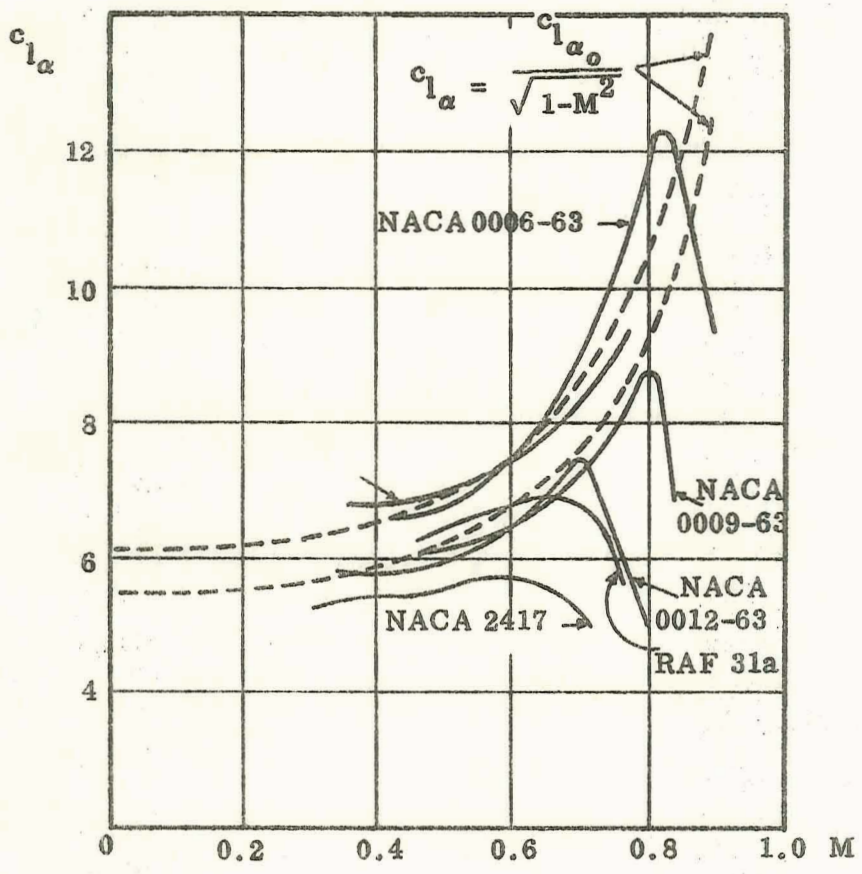

Figure 50 Effect of Mach Number on Lift Curve Slope

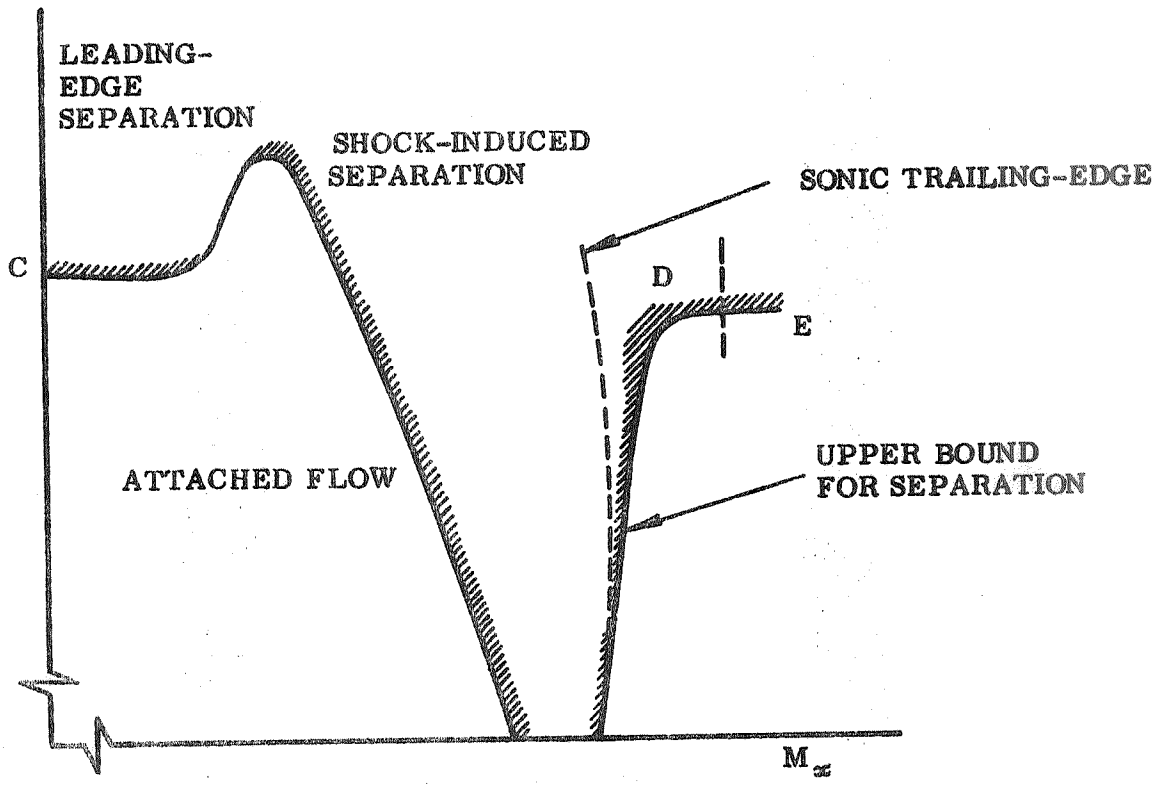

Figure 51 Separated Flow α-M-Boundaries

(AR = 5.1, TR = 0.71, $\Lambda = 35^\circ$ Ref. 79), they seem to agree rather well with the low α-limit for stall flutter of a wing with a 64-012 airfoil (AR = 7.36, TR = 0.42, $\Lambda = 11.1^\circ$, Ref. 75) judging by Figure 52. One has to bear in mind that the data for 65A012 are for $R_c \approx 1.6 \times 10^6$, and that the flutter test Reynolds number was $R_c \approx 10^5$ in air and $R_c \approx 10^6$ in Freon. In addition the flutter boundary is affected by structural damping and oscillation amplitude. However, these latter effects do not distort the stall flutter boundary appreciably, as the damping variation with amplitude is very steep when extrapolating towards infinitesimal amplitude (see Figure 41) Consequently, one might conclude from these data that the low α-limit for stall flutter is nothing but the static stall angle α_s for the same Reynolds and Mach number. It was these results that during the early phase of this study led us to predict that the full scale low α-limit would move to higher α-values, i.e., the α_s-values corresponding to flight Reynolds and Mach number. This low α-limit may still be a realistic boundary for stall flutter as occurring for increasing angles of attack. However, for the space shuttle transition maneuver (Ref. 80), where the angle of attack is continually decreased, such a boundary is not realistic according to the analysis in Sections 2 and 3.

The amplitude modulation effects, Eqs. (21) and (30), predict that the dynamic reattachment angle moves towards the zero-Reynolds number limit (and the dynamic stall angle towards the infinite Reynolds number limits) in proportion to the angular rate $\left| c\dot{\alpha}/U_\infty \right|$. That is, we would predict that the stall flutter boundary for the space shuttle vehicle would approach these limits, at least at low Mach numbers where the reduced frequency $\tilde{\omega}$ is large (Figure 46). As the Mach number is increased, Mach number effects limit the margin for dynamic overshoot of the static stall, thus moving the infinite Reynolds number limit towards lower α-values. In addition to this effect, which was discussed earlier in the discussion of Figures 48 and 49, the stall flutter data (Ref. 75), due to the test setup, will have a decreasing reduced frequency with increasing Mach number (Figures 46 and 52). That is, $c\dot{\alpha}/U_\infty$ (per unit amplitude $\Delta\theta$) decreases for increasing Mach number*, further hastening the movement to the

*That is, the capability to reach the infinite Reynolds number limit is decreasing. How large this effect is cannot be assessed without a complete structural dynamics analysis, as it is determined by the flutter limit cycle amplitude.

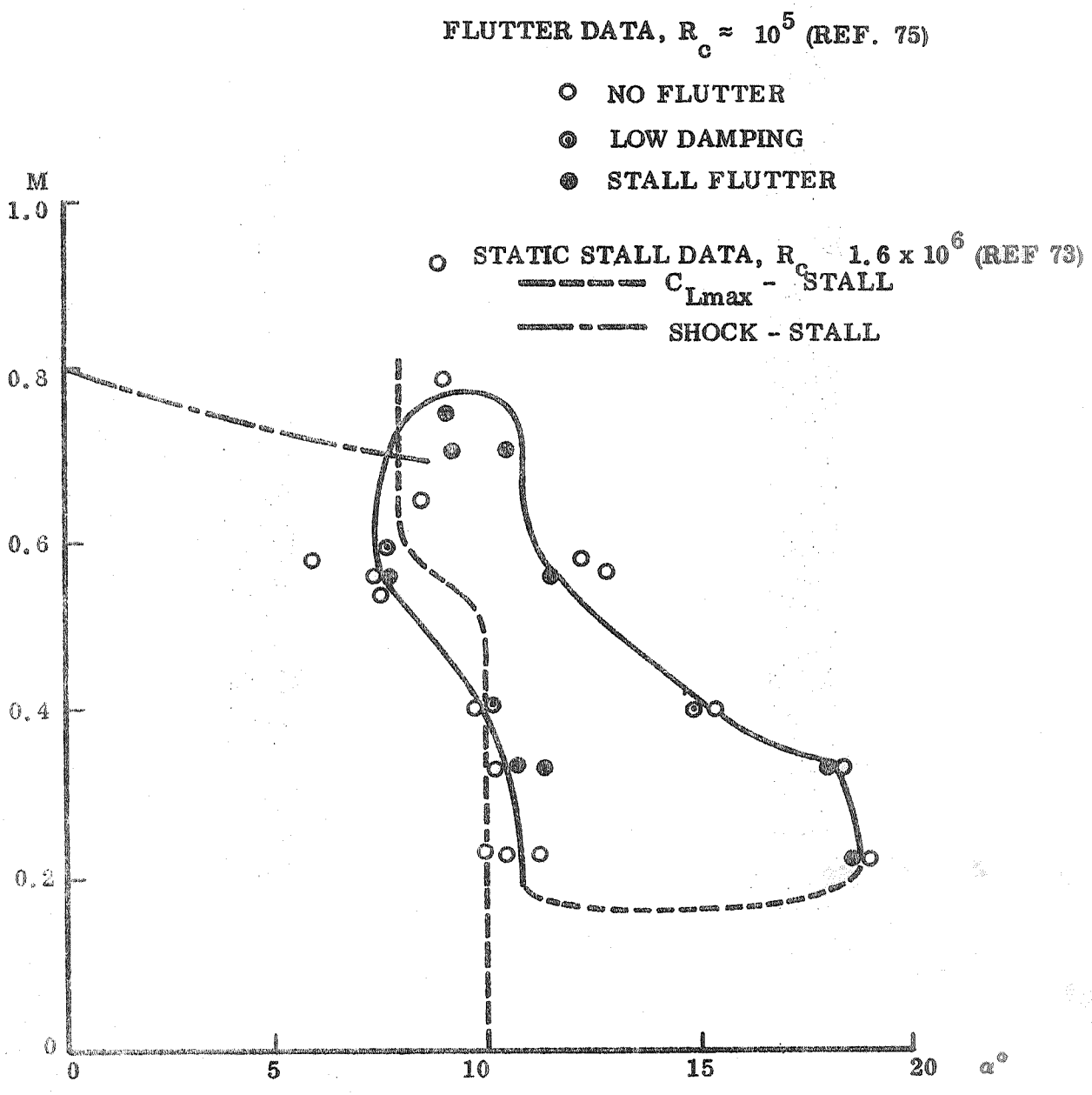

Figure 52 Stall Flutter and Static Stall Boundaries

left of the high α-limit for stall flutter with increasing M. For the low α-limit correspondingly decresed capability to reach the zero Reynolds number limit is realized for increasing Mach number. However, here the pure Mach number effect is to move the zero-Reynolds number reattachment (and stall) limit towards lower α's for increasing M, and the resultant stall flutter low α-limit is decreasing for increasing Mach number (Figure 53).

When trying to correct the incompressible stall limit for Mach number effects (Figure 53), we face the problem of placing the "incompressible" data in regard to Mach numbers below 0.4. The two-dimensional data for the NACA 64-012 airfoil, as reported in Ref. 55, were obtained at velocities between 150 and 300 miles per hour. Using the corresponding high and low Mach number for these "incompressible" stall data, i.e., M = 0.2 and M = 0.4, gives the two high α-limits for stall flutter shown in Figure 53. The airfoil nose radius $\left(\rho_N = 1.04\%\right)$ at the two dimensional stall angle $\left(\alpha_s = 16°\right)$ gives a supersonic peak velocity of $M_e = 1.4$ for $M_\infty = 0.35$ (Figure 47). The pull-up data (Figure 49) showed a "freezing" of the compressibility effect at $M_\infty = 0.4$. If one assumes that the shock-augmented leading edge separation, existing at $0.4 < M_\infty < 0.8$, behaves similarly to the stall at the zero Reynolds number limit, i.e., the separation point movement is practically negligible, then n_R in Eq. (95) has the value $n_R = 5/2$ for $M \leq 0.4$, and $n_R = 1$ for $0.4 < M < 0.8$. The low α-limit, the zero Reynolds number limit, is, of course, also given by $n_R = 1$ in Eq. (95). The high and low α-limits for stall flutter, determined in this manner, agree remarkably well with the boundaries determined through the flutter test. As the predictions are for zero structural damping, the predicted boundaries should be slightly conservative, which they appear to be*.

The high Mach number cut-off of the stall flutter boundary (Figures 46, 52, 53) simply reflects the fact that the shock induced separation that occurs at higher Mach numbers (Figures 51 and 52) does not generate (high enough) negative damping. Only

*The bending instability data point can be interpreted to support the predicted undamped aerodynamics at that α-M value.

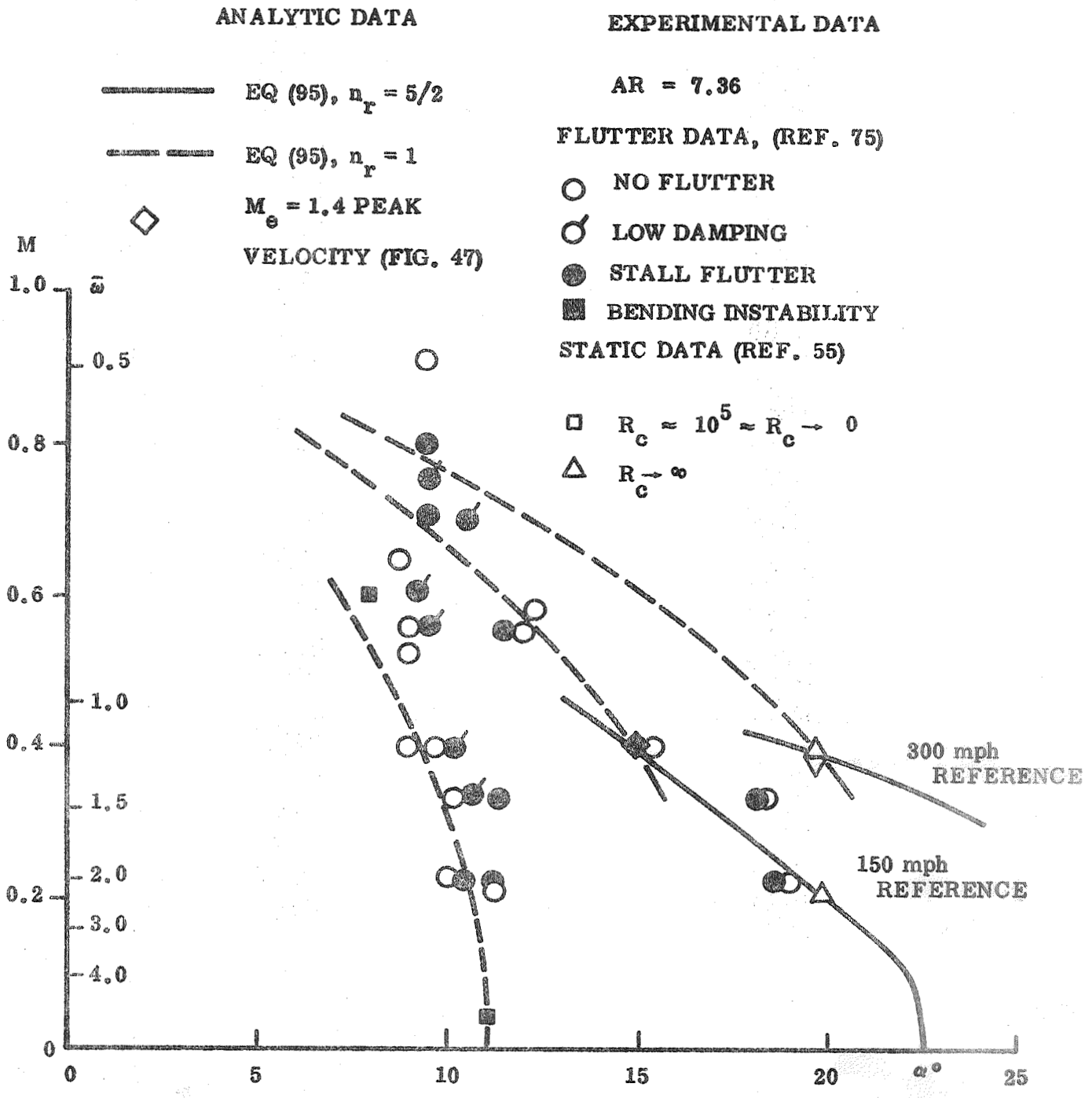

Figure 53 Predicted and Measured α-Boundaries for Stall Flutter

for elastic axis locations well aft of the 25% chord will negative damping be generated, and at a decreasing rate for increasing α (Eqs. (53), (54) and Figure 18). That is, no stall flutter is, as a rule, caused by shock induced separation. The low Mach number cut-off in Figure 46 is not an effect of the free stream Mach number at all. Due to the fixed wing stiffness, the reduced frequency $\left(\bar{\omega} = c\omega/U_\infty\right)$ increases as the tunnel speed is decreased until it finally reaches values near those of the vortex wake, Eqs. (71) and Figures 46 and 52. It has been shown that the vortex shedding off a cylinder is affected by the cylinder response (Ref. 68) and that the wake damps the cylinder oscillations when the cylinder oscillation frequency exceeds the vortex shedding frequency, (Ref. 81 and Figure 54). The maximum "undamping resonance effect" is obtained when the cylinder oscillates 5 percent below the vortex wake frequency. Rainey's stall flutter results (Ref. 59) show also this cut-off of the flutter boundary between $\bar{\omega} = 2$ and $\bar{\omega} = 4$ (Figure 55).

If the minimum flutter boundary (Ref. 75) is plotted versus a reduced frequency parameter based on sonic velocity, the flutter seems to disappear when trailing and leading edge translate relative to each other with sonic speed, i.e., for $\omega c/a = 1$ (Figure 56). One may make a case for shocks cutting off the communication with the wake when the trailing edge starts moving at supersonic translatory velocities, thereby eliminating the flutter. As the translatory trailing edge velocity is $\left(1 - \xi_{CG}\ c\dot{\alpha}\right)$, the parameter

$$\bar{\omega}_a = \left(1 - \xi_{CG}\right)\frac{\omega c}{a} \tag{96}$$

should then correlate the flutter boundary cut-off. Rainey's data (Ref. 59) for varying elastic axis location do not indicate such a dependence. The fact that the minimum flutter Mach number is linearly dependent upon $\omega c/a$ (Ref. 59) does only verify that the flutter disappears when $\bar{\omega}$ exceeds a certain critical value, which is constant, independent of Mach number. That is,

$$\bar{\omega} = \frac{1}{M}\ \frac{c\omega}{a} \qquad \text{implies} \qquad M_{crit} = \frac{1}{\bar{\omega}_{crit}}\ \frac{c\omega}{a}$$

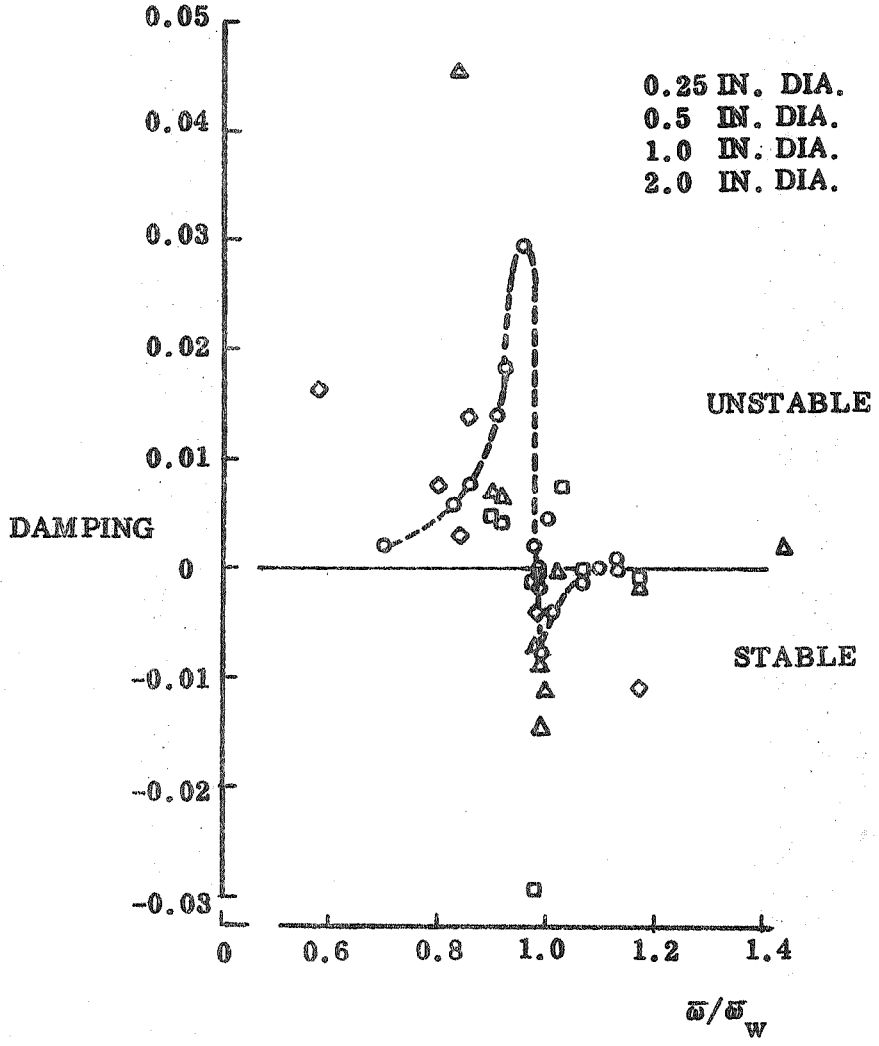

Figure 54 Cylinder Response to Karman Vortex Shedding

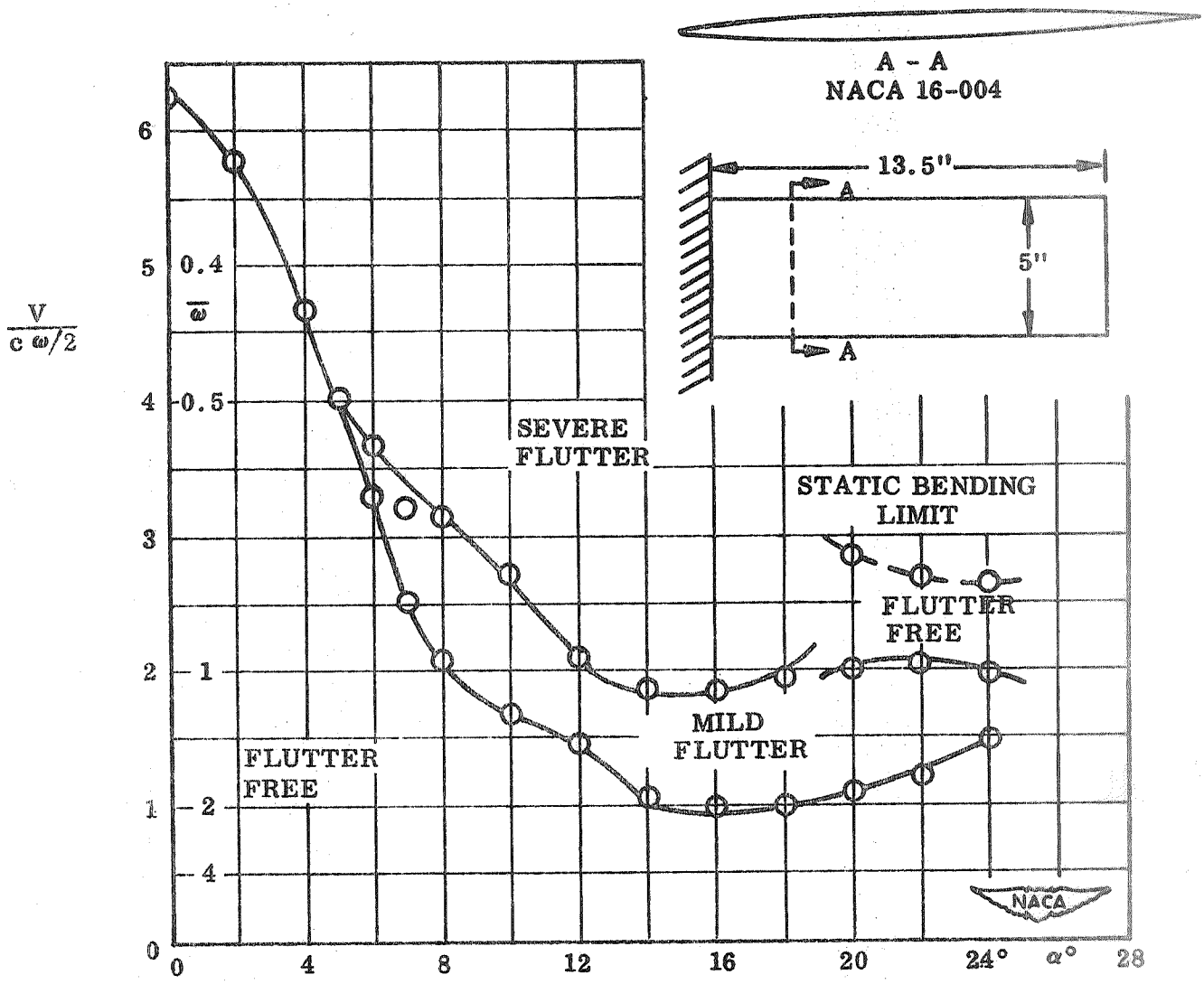

Figure 55 Stall Flutter Boundaries for a NACA 16-004 Airfoil (Ref. 61)

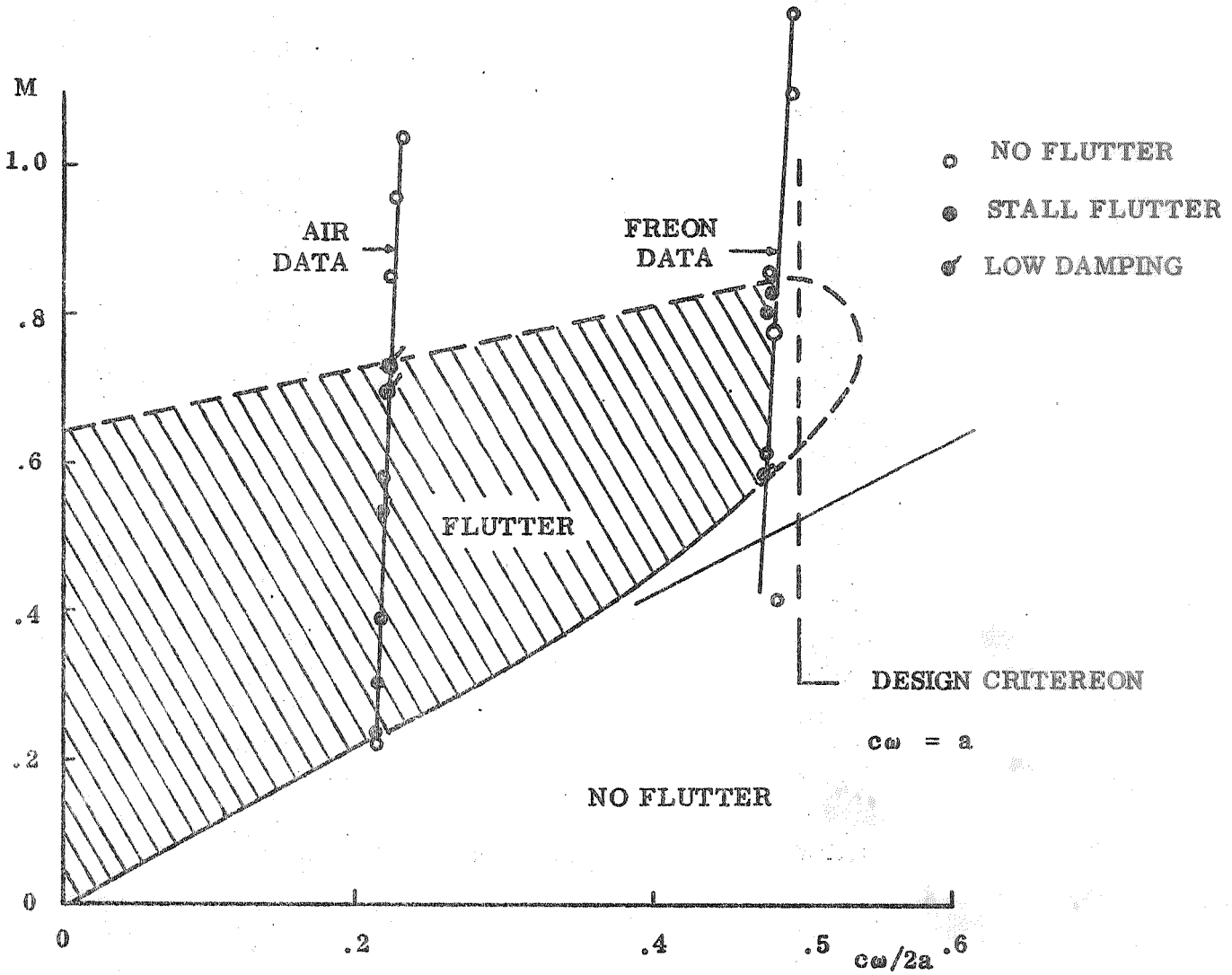

Figure 56 Stall Flutter Boundaries Using Mach Number and a Reduced Frequency Parameter Based on Sonic Speed (Ref. 75)

The data in Figure 8 of Ref. 59 give $\bar{\omega}_{crit} = 2.35$, right in the "ball park" given by Eq. (71). Rainey's data (Ref. 59) also indicate that there is no magic cut-off at $c\omega/a = 1.0$.

Both the wake resonance and this supersonic translation effect are probably playing a part in the low Mach number - high frequency cut-off. The wake resonance damping effect would disappear when $\bar{\omega}$ is increased beyond the critical value (Figure 54), and one would expect recurrence of flutter if no supersonic cut-off effect were present. It is, of course, rather difficult to get flutter at very high frequencies, even if the aerodynamic undamping is present, because the structural damping increases very fast (in relative magnitude) with increasing reduced frequency, i.e., with decreasing dynamic pressure.

The predicted stall flutter boundary for the wind tunnel test is not much different now from what it was during the early phase of the study. The big difference is the "analytic extrapolation" to full scale from the wind tunnel stall flutter data. Earlier we predicted that the stall flutter region would change greatly, and in such manner that the wind tunnel test was highly conservative. With the present analytic tools we predict that the full scale flutter boundary for the space shuttle transition maneuver will be very closely the same as in the wind tunnel test (Figure 57a). The $\bar{\omega}$-M-coupling may be somewhat different, but it is essentially the same, and infinite and zero Reynolds number limits are, of course, the same. For an aircraft entering the stall region from below (increasing α) our earlier prediction that the wind tunnel test is very conservative still holds (Figure 57b).

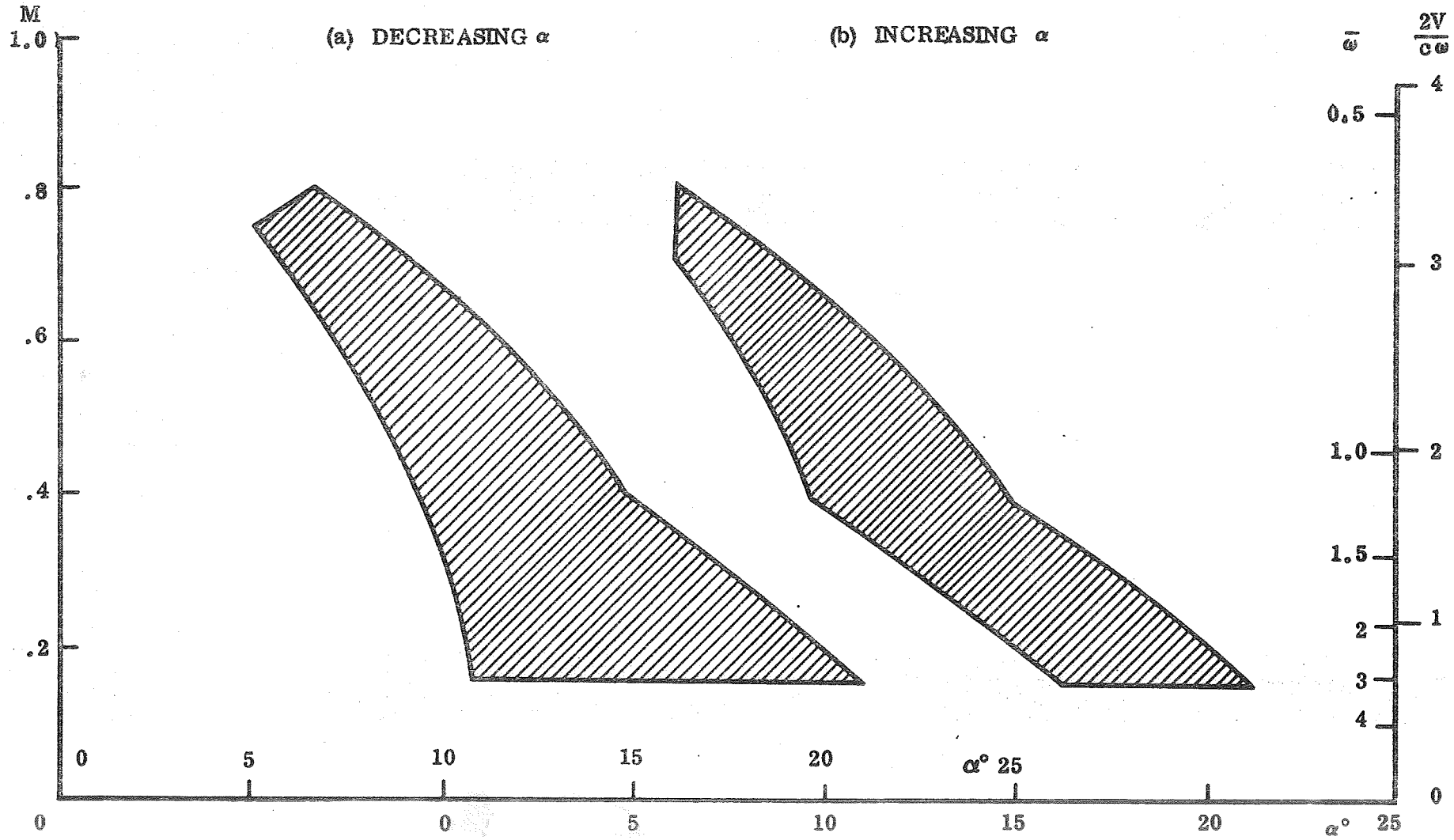

Figure 57 Predicted Stall Flutter Boundaries for Full Scale Flight Reynolds Numbers

Section 6
CONCLUSIONS

A study of unsteady airfoil stall and stall flutter has given the following results:

The large adverse dynamic effects of airfoil stall are caused by the pitch rate induced dynamic overshoot of the static stall and the large time lag associated with the following post stall characteristics.

The dynamic overshoot is caused by the decelerating wall effect, Eqs. (28) - (30) and/or the pressure gradient delay, Eq. (21).

The additional time lag for the post stall characteristics, which at high frequencies is large and completely dominates the Karman-Sears wake lag, is induced by the "moving wall" effect of the moving separation point, Eqs. (62) - (66).

Both the dynamic overshoot and the separation induced time lag are in a first approximation directly proportional to the angular rate of change, $c\dot{\alpha}/U_\infty$. At low and moderately high frequencies, where this first approximation is valid, the developed analytic theory predicts the dynamic loops and negative aerodynamic damping measured in wind tunnel tests using only static experimental data as an input. At higher frequencies a semi-empirical graphical method gives improved predictions.

Compressibility effects are not found to change the dynamic stall characteristics in principle until the Mach number gets high enough to cause shock-stall rather than leading edge stall. The shock-induced boundary layer separation and associated unsteady aerodynamic characteristics are described analytically, using static experimental data together with inviscid estimates to define the separation induced loads. For the shock-induced separation, the time lag generated by the separation point movement is amplified by the motion induced change of shock strength, Eqs. (33) - (38).

The perturbation of the shock induced boundary layer separation causes high frequency selfsustained quasi-harmonic oscillations that can be described analytically using static experimental data as an input, Eqs. (42)-(47). It can be shown that when the shock is near the leading edge, the self-sustained oscillations are of the type described by Trilling for laminar boundary layers. When the shock is farther away from the leading edge, the separation is no longer of the free interaction type but is controlled by the trailing edge and near wake flow conditions.

Three dimensional flow effects are found to have very pronounced influence even (or maybe, especially) on so called "two-dimensional" tests. The most important consequence is that dynamic stall data obtained in wind tunnel tests are very difficult to apply to full scale. The problem of Reynolds number scaling is found to exist only when determining the low angle of attack stall flutter boundary for increasing airplane attitudes. The dynamic stall characteristics in themselves, however, are found to be Reynolds number insensitive, at least for the amplitude- and frequency-ranges investigated so far in wind tunnel tests. The reason is that the pitch rate induced effects on the boundary layer are so powerful that the Reynolds number effects are washed out.

The experimentally measured upper and lower angle of attack stall flutter boundaries for a space shuttle wing are well predicted by the developed analytic theory. It is shown that the high Mach number cut-off of the stall flutter boundary is due to the fact that the leading edge stall has converted to shock-stall, which in itself does not cause aerodynamic negative damping with resultant stall flutter unless the elastic axis is far aft of the quarter chord. The low Mach number cut-off of the boundary is found to correspond to the high frequency at which the vortex wake shedding exerts a damping effect on the airfoil oscillation.

While it may still be said that no satisfactory stall flutter analysis has yet been developed, the results of the present analysis are so encouraging that one is tempted to prophesy that such an analytical theory will soon be available.

Section 7
RECOMMENDATIONS FOR FUTURE STUDY

The results of the present study are encouraging. The experimental unsteady airfoil stall characteristics at low frequencies ($\bar{\omega} \leq .40$) were well predicted from static airfoil characteristics using a linear quasi-steady, lumped-time-lag, technique. Throughout the frequency range the results of this method are at least as good as those obtained by synthesizing the unsteady stall characteristics from dynamic measurements.

It is possible to substantially improve the high frequency results by accounting for non-linearities in the analysis. A rather simple modification of static characteristics and phase lag near stall shows significant high frequency improvements. A similar approach to modify reattachment description should further improve high frequency results. The zero Reynolds number characteristic used presently as a return stroke limit, experiences "lift stall" before "moment stall." This is, of course, only a semantic anomaly. Both lift and moment stall occur at the same time. The details of the stall are such that the distribution of the separation induced lift losses produces equal and opposite moment components, thus erasing the stall clues from the moment characteristics.

The problem is one of decomposing the stall (or reattachment) into a finite number of lumped loads with appropriate time lags. Once this is accomplished a better analytic description of turbulent trailing edge stall is also possible. Thus, the next order of business is to examine the details of the stall and reattachment processes in regard to the load distribution. The present computer program supplies a powerful tool in such a study. It allows one to compare various interpretations of the lumped load distribution using different time lags with the variety of dynamic experimental data available in the literature. By playing static and dynamic results against each other in this manner, one will be able to gain insight impossible to obtain any other way.

Once a viable technique has been developed for prediction of unsteady airfoil stall characteristics throughout the frequency range, it would be meaningful to generate a library of such dynamic section characteristics. These data may not be obtainable any other way. The end plate and wall interference effects always present in dynamic wind tunnel tests, and varying from test to test, make it difficult to utilize dynamic test data by themselves for prediction of full scale stall flutter. By utilizing the dynamic characteristics as reshaped after correlation with computed characteristics, much more reliable dynamic airfoil section characteristics can be provided. For the full scale application one would, of course, still have to account for spanwise flow effects, etc., in computing the final stall flutter characteristics. However, knowing the dynamic section characteristics allows one to make an intelligent choice of section shape for a helicopter rotor, compressor blade, or space shuttle wing, in order to minimize stall flutter problems.

There are certainly a variety of experimental investigations that would help this analysis significantly, but much analysis remains still to be made using existing data before significant new facts will be obtained experimentally. It appears that the most efficient approach towards the development of a satisfactory stall flutter prediction capability is to first refine the present analytic tools. In particular, one faces the problem that for stall flutter prediction one is concerned with high frequency small amplitude oscillations, in which case both stall and reattachment occur at the ends of the oscillation cycle where the angular rate changes fast, violating the constant time lag assumption used in the present analysis. Until this deficiency has been removed, no really effective utilization of (all the) available dynamic data will be possible.

Section 8

REFERENCES

1. Harris, F. D. and Pruyn, R. P., "Blade Stall - Half Fact, Half Fiction," American Helicopter Society Journal, Vol. 13, No. 4, April 1968, pp. 27-48.

2. Liiva, J. "Unsteady Aerodynamic and Stall Effects on Helicopter Rotor Blade Airfoil Sections," J. Aircraft, Vol. 6, No. 1, Jan-Feb. 1969, pp. 46-51.

3. Ham, N. D. and Garelick, M. S., "Dynamic Stall Considerations in Helicopter Rotors," American Helicopter Society Journal, Vol. 13, April 1968, pp. 44-55.

4. Carta, F. O., "Unsteady Normal Force on an Airfoil in a Periodically Stalled Inlet Flow," J. Aircraft, Vol. 4, No. 5, Sept-Oct. 1967, pp. 416-421.

5. Runyan, H. L. and Reed, W. H., "Dynamics and Aeroelasticity - An Appraisal," Astronautics & Aeronautics, Vol. 9, No. 2, Feb. 1971, pp. 48-57.

6. Ericsson, L. E. and Reding, J. P., "Unsteady Airfoil Stall," NASA CR 66787, 1969.

7. Ericsson, L. E., and Reding, J. P., "Unsteady Airfoil Stall, Review and Extension," J. Aircraft, Vol. 8, No. 7, July 1971.

8. Ericsson, L. E. and Reding, J. P., "Dynamic Stall Simulation Problems," J. Aircraft, Vol. 8, No. 7 or 8, July or Aug. 1971.

9. von Karman, Th. and Sears, W. R., "Airfoil Theory for Non-Uniform Motion," Journal Aeronautical Sci., Vol. 5, No. 10, Aug. 1938, pp. 379-390.

10. Ericsson, L. E., "Aeroelastic Instability Caused by Slender Payloads," Journal Spacecraft and Rockets, Vol. 4, No. 1, Jan. 1967, pp. 65-73.

11. Schlichting, H., Boundary Layer Theory, translated by J. Kestin, McGraw Hill, N. J., 1955, pp. 206-214.

12. Ville, G., "Influence des Decallements au Bord d'Attaque sur les Characteristiques Aerodynamiques des Voilures," Association Francaise des Ingenieurs et Techniciens des l'Aeronautique et de l'Espace, Colloque d'Aerodynamique Appliquee, 4th, Lille, France, Nov. 8-10, 1967.

13. Abbot, I. H., Von Doenhoff, A. E., and Stivers, L. S., "Summary of Airfoil Data," NACA TR 824 (1945).

14. McCullough, G. B. and Gault, D. E., "Examples of Three Representative Types of Airfoil-Section Stall at Low Speed," NACA TN 2502, 1951.

15. Bushnall, W. J. and Lofting, L. K., "Experimental Investigation of Localized Regions of Laminar Boundary Layer Separation," NACA TN 2338, 1951.

16. Crabtree, L. F., "Prediction of Transition in the Boundary Layer of an Aerofoil," Journal Royal Aeronautical Society, July 1958, pp. 525-528.

17. Wallis, R. A., "Boundary Layer Transition at the Leading Edge of Thin Wings and Its Effect on General Nose Separation," Advances in Aeronautical Sciences, Proceedings of the Second International Congress in the Aeronautical Sciences, Zurich, 12-16 September 1970, pp. 161-184.

18. Gault, D. E., "An Experimental Investigation of Regions of Separated Laminar Flow," NACA TN 3505, 1955.

19. Obremski, H. J., and Morkovin, M. V., "Application of Quasi-Steady Stability Model to Periodic Boundary-Layer Flows," AIAA Journal, Vol. 7, No. 7, July 1969, pp. 1298-1301.

20. Moore, F. K., "On the Separation of the Unsteady Laminar Boundary Layer," IUTAM Symposium on Boundary Layer Research, Freiburg, August 26-29, 1957, pp. 296-311.

21. Brady, W. G. and Ludwig, G. R., "Basic Studies of Rotating Stall and an Investigation of Flow-Instability Sensing Devices," AF APL-TR-65-115, October 1965.

22. Brady, W. G. and Ludwig, G. R., "Research on Unsteady Stall of Axial Flow Compressors," CAL Report No. AM-1762-S-4, Nov. 1963.

23. Kelly, J. A., "Effect of Modifications to the Leading-Edge Region on the Stalling Characteristics of the NACA 63-012 Airfoil Section, NACA TN 2228, 1950.

24. Maki, R. L. and Hunton, L. W., "An Investigation at Subsonic Speeds of Several Modifications to the Leading-Edge Region of the NACA 64A010 Airfoil Section Designed to Increase Maximum Lift," NACA TN 3871, 1956.

25. Ericsson, L. E. and Reding, J. P., "Aerodynamic Effects of Bulbous Bases," NASA CR-1339, 1969.

26. Furlong, C. G. and Fitzpatrick, J. E., "Effects of Mach Number up to 0.34 and Reynolds Number up to 8×10^6 on the Maximum Lift Coefficient of a Wing of NACA 66-Series Airfoil Sections," NACA TN-2251, 1950.

27. Halfman, R. L., Johnson, H. C. and Haley, S. M., "Evaluation of High-Angle-of Attack Aerodynamic-Derivative Data and Stall-Flutter Prediction Techniques," NACA 2533, 1951.

28. Conner, F., Willey, C. and Twomey, W., "A Flight and Wind Tunnel Investigation of the Effect of Angle-of-Attack Rate on Maximum Lift Coefficient, NACA CR-321, 1965.

29. Harper, P. W. and Flanigan, R. E., "The Effect of Rate of Change of Angle of Attack on the Maximum Lift of a Small Model," NACA TN 2061, 1949.

30. Gadeberg, B. L., "The Effect of Rate of Change of Angle of Attack on the Maximum Lift of a Pursuit Airplane," NACA TN 2525, 1951.

31. Harper, P. W. and Flanigan, R. E., "Investigation of the Variation of Maximum Lift for a Pitching Airplane Model and Comparison with Flight Results," NACA TN 1734 (1948).

32. Spreiter, J. R., Galster, G. M., and Blair, W. K., "Effect of Mach and Reynolds Number on the Maximum Lift Coefficient Obtainable in Gradual and Abrupt Stalls of a Pursuit Airplane Equipped with a Low Drag Wing," NACA RM A5G06, 1945.

33. Twaites, B., Incompressible Aerodynamics, Fluid Motion Memoirs, Oxford at the Clarendon Press, 1960, pp. 211 and 223.

34. Swartz, F. and Wuest, W., "Flight Test and Wind-Tunnel Measurements on Airfoils with Boundary Layer Suction for Increasing Maximum Lift," Proceedings of the 4th Congress of the International Council of the Aeronautical Sciences, Spartan Books, Wash. D.C., 1965, pp. 459-480.

35. Fink, M. P., "Full Scale Investigation of the Aerodynamic Characteristics of a Sailwing of Aspect Ratio 5.9," NASA-TND-5047, 1969.

36. Hurley, D. G. and Ward, G. F., "Experiments on the Effects of Air Jets and Surface Roughness on the Boundary Layer Near the Nose of an NACA 64A006 Airfoil," Aeronautical Research Laboratories, Australia, ARL Aero Note 128, Sept. 1953.

37. Liiva, J., Davenport, F. J., Gray, L. and Walton, I. C., "Two-Dimensional Tests of Airfoils Oscillating Near Stall," Volumes I and II, USAAVLABS TR 68-13A & B, April, 1968.

38. Wallis, R. A., "The Turbulent Boundary Layer on the Articulated Nose of a Thin Wing Provided with Air Jets," Aeronautical Research Laboratories, Australia, ARL Aero Note 141, Oct. 1954.

39. Pearcey, H. H., "Shock-Induced Separation and its Prevention by Design and Boundary Layer Control," Boundary Layer and Flow Control, Vol. 2, Pergamon Press, N. Y., 1961, pp. 1166-1349.

40. Pearcey, H. H., "Some Effects of Shock-Induced Separation of Turbulent Boundary-Layers in Transonic Flow Past Airfoils," Paper 9, Proceedings of Symposium on Boundary Layer Effects in Aerodynamics, National Physics Laboratory, Great Britain, March 31 - April 1, 1955.

41. dePaul, V., "Recherches sur des Profils Transsoniques de Faible Trainee," Association Francaise des Ingenieurs et Techniciens de l'Aeronautique et de l'Espace, Colloque d'Aerodynamique Appliquee, 4th, Lille, France, Nov. 8-10, 1967.

42. Summers, J. L. and Treon, S. L., "The Effects of Amount and Type of Camber on the Variation with Mach Number of the Aerodynamic Characteristics of a 10-percent-thick NACA 64A-Series Airfoil Section," NACA TN 2096, 1950.

43. Glauert, H., "The Effects of Compressibility on the Lift of Airfoils," Proc. Roy. Soc., Series A, CXVIII, 1927, pp 113-119.

44. Jones, W. P., "Research on Unsteady Flow," The Sixth Minta Martin Lecture, Journal of Aerospace Sciences, Vol. 29, No. 3, March 1962, pp. 249-263.

45. Lambourne, N. C. "Some Instabilities Arising from the Interaction Between Shock Waves and Boundary Layers," Aero Research Council, C.P. No. 473, Feb. 1958.

46. Trilling, L., "Oscillating Shock Boundary-Layer Interaction," Journal of Aerospace Sciences, Vol. 25, No. 5, May 1958, pp. 301-304.

47. Gardner, M. F. and Barnes, J. L., "Transients in Linear Systems," John Wiley & Sons, Inc., New York, 1956.

48. Fizdon, W., "Some Experimental Results of Generating High Frequency Oscillating Shock-Waves and Oscillating Shock-Wave Boundary-Layer Interaction at Supersonic Speeds," Advances in Aerodynamic Sciences, Vol. 3, Pergamon Press, N. Y., 1962, pp. 433-446.

49. NACA Ames Research Staff, "Equations, Tables, and Charts for Compressible Flow," NACA Report 1135, 1953.

50. Reding, J. P. and Ericsson, L. E., "Loads on Bodies in Wakes," Journal of Spacecraft and Rockets, Vol. 4, No. 4, April 1967, pp. 511-518.

51. Jordan, P. F., Comment on "Thermally Induced Vibration and Flutter of a Flexible Boom," Journal of Spacecraft and Rockets, Vol. 8, No. 2, Feb. 1971, pp. 204-205.

52. Ericsson, L. E., "Loads Induced by Terminal-Shock Boundary-Layer Interaction on Cone-Cylinder Bodies," Journal of Spacecraft & Rockets, Vol. 7, No. 9, Sept. 1970, pp. 1106-1112.

53. Sinnot, C. S., "On the Prediction of Mixed Subsonic/Supersonic Pressure Distributions," Journal of the Aerospace Sciences, Vol. 27, No. 10, Oct. 1960, pp. 767-778.

54. Critzos, C. C., Heyson, H. H. and Boswinkle, Jr., R. W., "Aerodynamic Characteristics of NACA-0012 Airfoil Section at Angles of Attack from 0° to 180°," NACA TN 3361 (1955).

55. Jacobs, E. N. and Sherman, A., "Airfoil Section Characteristics as Affected by Variations in the Reynolds Number," NACA TR 586 (1937).

56. Carta, F. O. and Niebanck, C. F., "Prediction of Rotor Instability at High Forward Speeds, Volume III, Stall Flutter," USAAVLABS TR 68-18C, February 1969.

57. Carta, F. O., "An Analysis of the Stall Flutter Instability of Helicopter Rotor Blades," with Comment by Ham, N. D., "Stall Flutter of Helicopter Rotor Blades – A Special Case of the Dynamic Stall Phenomenon," Paper No. 130, Proceedings 23rd Annual National Forum of the American Helicopter Society, Washington, D. C., May 10-12, 1967.

58. Arcidiacono, P. J., Carta, F. O., Casellini, L. M. and Elmon, H. L., "Investigation of Helicopter Control Loads Induced by Stall Flutter," USAAVLABS TR 70-2, March 1970.

59. Harris, F. D., Tarzanin, F. J. Jr., and Fisher, R. K. Jr., "Rotor High Speed Performance, Theory vs Test," Proceedings of the V/STOL Technology and Planning Conference (AFFDL), Las Vegas, Nevada, 23-29 Sept. 1969.

60. Theisen, J. G., "Vortex Periodicity in Wakes," AIAA Preprint 67-34, 1967.

61. Rainey, G. A., "Preliminary Study of Some Factors Which Affect the Stall-Flutter Characteristics of Thin Wings," NACA TN 3622, 1956.

62. Rainey, A. G., "Progress on the Launch Vehicle Buffeting Problem," Journal of Spacecraft and Rockets, Vol. 2, No. 3, May-June 1965, pp. 289-299.

63. Ericsson, L. E. and Reding, J. P., "Analysis of Flow Separation Effects on the Dynamics of a Large Space Booster," Journal of Spacecraft and Rockets, Vol. 2, No. 4, Jul-Aug. 1965, pp. 481-490.

64. Steiner, R. W., "Experimental Study of the Unsteady Flow Characteristics of Stalled Airfoils," AF Institute of Technology, Report GAEO56, August 1956.

65. Ham, N. D. and Young, M. I., "Torsional Oscillation of Helicopter Blades due to Stall," Journal of Aircraft, Vol. 3, No. 3, May-June, 1966.

66. Greidanus, J. H., van de Voren, A. I. and Bergh, H., "Experimental Determination of the Aerodynamic Characteristics of an Oscillating Wing with Fixed Axis of Rotation," NLL Report F-101, Jan. 1952.

67. Woods, L. C. "The Theory of Subsonic Plane Flow," Cambridge University Press, 1961, pp. 456, 457, 475, 476.

68. Parkinson, G. V. and Ferguson, N., "Amplitude and Surface Pressure Measurements for a Circular Cylinder in Vortex-Excited Oscillation at Subcritical Reynolds Numbers," Paper 18, Meeting on Ground Wind Load Problems in Relation to Launch Vehicles, NASA Langley Research Center, June 7-8, 1966.

69. Scruggs, R. M., Lockheed Georgia Research Laboratories, Private Communication of presently unpublished data.

70. Bollay, W. and Brown, C. D., "Some Experimental Results on Wing Flutter," Journal Aero. Sci., Vol. 8, No. 8, June 1941, pp. 313-318.

71. Ericsson, L. E., "Separated Flow Effects on the Dynamic Stability of Blunt-Nosed Cylinder-Flare Bodies," Report LMSC-667991, Contract NAS 8-5338, Dec. 1965.

72. Fung, Y. C., "An Introduction to the Theory of Aeroelasticity," Dover Publ. Inc., N. Y. 1968, pp. 190, 191.

72A. Ref. 72, pp. 209, 210.

73. Ericsson, L. E. and Reding, J. P., "Reentry Capsule Dynamics," AIAA 70-563, 1970.

74. Ericsson, L. E. and Reding, J. P., "Dynamics of Separated Flow over Blunt Bodies," Lockheed Missiles & Space Company, Report 2-80-65-1, NASA Contract NAS 8-5338, Dec. 1965.

75. Goetz, R. C., "Exploratory Study of Buffet and Stall Flutter of Space Shuttle Vehicle Wing Concepts," NASA LWP-872, May 22, 1970.

76. Perkins, C. D. and Hage, R. E., "Airplane Performance Stability and Control," John Wiley & Sons, Inc., New York, 1949, pp. 27 and 28.

77. Jecmen, D. M., Reding, J. P., and Ericsson, L. E., "An Application of Automatic Carpet Plotting to Wind-Tunnel Data Reduction," Journal of Spacecraft and Rockets, Vol. 4, No. 3, March 1967, pp. 408-410.

78. Fung, Y. C., "An Introduction to the Theory of Aeroelasticity," Dover Publ. Inc., N. Y. 1968, p. 129.

79. Hunton, L. W., "A Study of the Application of Airfoil Suction Data to the Estimation of the High-Subsonic-Speed Characteristics of Swept Wings," NACA RM A55C23, 1955.

80. Stengel, R. F., "Optimal Transition from Entry to Cruising Flight," AIAA 70-1018, August 1970.

81. Cincotta, J.J., Jones, G.W., and Walker, R.W., "Experimental Investigation of Wind Induced Oscillation Effects on Cylinders in Two-Dimensional Flow at High Reynolds Numbers," Paper 20, Meeting on Ground Wind Load Problems in Relation to Launch Vehicles, NASA Langley Research Center, June 7-8, 1966.

APPENDIX A

NOMENCLATURE

a	Speed of sound, m/sec
AR	aspect ratio, AR = b^2/S
A/A_o	amplitude ratio
b	wing span, m
c and $\bar{c}$	reference length, m c = 2-dim. chord length $\bar{c}$ = S/b, mean aerodynamic chord
f	frequency, CPS
H	boundary layer shape parameter, H = δ^*/θ
H_o	total pressure, kg/m^2
K_a	dynamic overshoot coefficient, eqs. (21) and (30)-(32)
K, k	reduced frequencies of shock boundary layer interactions, Eqs. (48) and (49), respectively.
L	lift, kg: Coefficient $C_L = L/\left(\rho_\infty U_\infty^2/2\right)S$
l	section lift, kg/m: Coefficient $c_l = l/\left(\rho_\infty U_\infty^2/2\right)c$
M	Mach number
M_p	pitching moment, kg-m: Coefficient $C_m = M_p/\left(\rho_\infty U_\infty^2/2\right)Sc$
m_p	section pitching moment, kg-m/m: Coefficient $c_m = m_p/\left(\rho_\infty U_\infty^2/2\right)c^2$
N	normal force, kg: Coefficient $C_N = N/\left(\rho_\infty U_\infty^2/2\right)S$

n	normal force, kg/m: Coefficient $c_n = n/\left(\rho_\infty U_\infty^2/2\right) c$
n_R	exponent for M-effect, eq. (95).
n	exponent for viscosity-temperature relationship, $n = 3/4$
p	static pressure, kg/m^2: Coefficient $C_p = \left(p - p_\infty\right)/\left(\rho_\infty U_\infty^2/2\right)$
q	pitch rate, rad/sec
R	radius, m
R_c and $R_{\bar{c}}$	Reynolds number based on chord length
r	radius , m
r_N	nose radius, m
S	reference area, m^2
S_o	Strouhal number of cylinder wake shedding, $S_o = \bar{\omega}_o/2\pi$
S_e	density ratio, $S_e = \rho_e/\rho_{wall}$, Eq. (50)
s	surface arc length coordinate, m
t	time, sec
T	period of oscillation, sec, $T = f^{-1}$
U	velocity, m/sec
$\bar{U}$	convection velocity, m/sec
U_w	apparent wall velocity, m/sec
V	flutter speed, m/sec
$V_\perp$	velocity normal to surface, m/sec
$\bar{v}$	velocity ratio, $v = U_e/U_\infty$
W	work by aerodynamic forces, kg-m, Eq. (84)
x	horizontal coordinate, m
y	airfoil surface height, m
z	translatory coordinate, m

α	angle of attack, radian or deg
α_o	trim angle of attack, radian or deg
$\tilde{\alpha}$	generalized angle of attack, radian, Eq. (59)
α_{s_1}	stall delay due to pressure gradient relief, Eq. (21)
α_{s_2}	stall delay due to "decelerating wall" effect, Eq. (30)
γ	ratio of specific heats
δ	boundary layer thickness, m
Δ	increment
ζ	damping, fraction of critical, eq. (43)
Λ	Sweep back angle of 25% chord line, radian or deg
θ	angle of attack perturbation, radian or deg
ξ	dimensionless x-coordinate, $\xi = x/c$
ξ_{CG}	center of oscillation
ρ	air density, kg-sec^2/m^4
ρ_N	non dimensional nose radius, $\rho_N = r_N/c$
σ	pitch rate induced camber angle, radian, $\sigma = \nu_{TE} - \nu_{LE}$
τ	dimensionless time, $\tau = t/\frac{c}{U_\infty}$
ν	camber line slope, radian or deg (Fig. 4)
ϕ	wake lag, radian or deg, Eq. (72)
ϕ_s	stall induced additional phase lag, radian or deg, Eq. (72)
ψ	total phase angle, radian or deg, $\psi = \omega t$
Ω	cylinder angular velocity, radian/sec (Fig. 33)

ω	oscillation frequency, radian/sec
$\bar{\omega}$	reduced frequency, $\bar{\omega} = \omega c/U_\infty$ $\left(\text{or } \omega \bar{c}/U_\infty\right)$
$\bar{\omega}_0$	reduced frequency of cylinder wake shedding, $\bar{\omega}_0 = \omega$ (diameter)/U

Subscripts

a	accelerated flow effect
AC	aerodynamic center
AM	apparent mass
CG	center of gravity
e	boundary layer edge conditions
E and eff	effective
H	hysteresis (static)
LE	leading edge
j	jet
N	nose
n	natural
M,n,N	numbering subscripts
QS	quasi-steady
R	reattachment
s	stall
sh	shock
TE	trailing edge
w	wake and wall
∞	undisturbed flow

O	initial value
1,2,3,4	numbering subscripts
$\perp$	surface normal

Superscripts

i	induced and inducing, e.g., $\Delta^i C_L$ = separation induced lift and α^i = separation inducing angle of attack
$\widehat{\ }$	value aft of a normal shock, e.g. $\widehat{p}_e$

Differential Symbols

$\dot{\theta} = \frac{\partial \theta}{\partial t}$; $\overset{o}{\xi} = \frac{\partial \xi}{\partial \tau}$

$c_{l_\alpha} = \frac{\partial c_l}{\partial \alpha}$; $v_\xi = \frac{\partial v}{\partial \xi}$

$c_{m_{\dot{\theta}}} = dc_m \Big/ d\left(\frac{c\dot{\theta}}{U_\infty}\right)$

$c_{\overline{m}_{\dot{\theta}}}$ = linear measure of non-linear damping, Eq. (86).